ABSTRACT

Title of dissertation: DESIGN, DEVELOPMENT, AND EVALUATION OF A MRI-GUIDED NEUROSURGICAL INTRACRANIAL ROBOT

Mingyen Ho, Doctor of Philosophy, 2013

Dissertation directed by: Professor Jaydev P. Desai
Department of Mechanical Engineering

Brain tumors are among the most feared complications of cancer. Their treatment is challenging because of the lack of good imaging modality and the inability to remove the complete tumor. To overcome this limitation, we propose to develop a Magnetic Resonance Imaging (MRI)-compatible neurosurgical robot. The robot can be operated under continuous MRI, and the Magnetic Resonance (MR) images can be used to supplement physicians' visual capabilities, resulting in precise tumor removal.

We have developed two prototypes of the Minimally Invasive Neurosurgical Intracranial Robot (MINIR) using MRI compatible materials and shape memory alloy (SMA) actuators. The major difference between the two robots is that one uses SMA wire actuators and the other uses SMA spring actuators combined with the tendon-sheath mechanism. Due to space limitation inside the robot body and the strong magnetic field in the MRI scanner, most sensors cannot be used inside the robot body. Hence, one possible

approach is to rely on image feedback to control the motion of the robot. In this research, as a preliminary approach, we have relied on image feedback from a camera to control the motion of the robot. Since the image tracking algorithm may fail in some situations, we also developed a temperature feedback control scheme which served as a backup controller for the robot. Experimental results demonstrated that both image feedback and temperature feedback can be used reliably to control the joint motion of the robots.

A series of MRI compatibility tests were performed to evaluate the MRI compatibility of the robots and to assess the degradation in image quality. The experimental results demonstrated that the robots are MRI compatible and created no significant image distortion in the MR images during actuation.

The accomplishments presented in this dissertation represent a significant development of using SMA actuators to actuate MRI-compatible robots. It is anticipated that, in the future, continuous MR imaging would be used reliably to control the motion of the robot. It is aspired that the robot design and the control methods of SMA actuators developed in this research can be utilized in practical applications.

DESIGN, DEVELOPMENT, AND EVALUATION OF A MRI-GUIDED NEUROSURGICAL INTRACRANIAL ROBOT

by

Mingyen Ho

Dissertation submitted to the Faculty of the Graduate School of the
University of Maryland, College Park in partial fulfillment
of the requirements for the degree of
Doctor of Philosophy
2013

Advisory Committee:
Professor Jaydev P. Desai, Chair/Advisor
Professor Nikhil Chopra
Professor Cornelia Fermüller
Professor Rao Gullapalli
Professor Satyandra K. Gupta
Professor Carol L. Keefer, Dean's Representative

Table of Contents

List of Figures

List of Abbreviations

Chapter 1

Introduction

This chapter provides the motivation of conducting this research and a literature review of related work. The research objectives and outlines are also covered.

1.1 Motivation

Brain tumors are among the most deadly adult tumors which account for 2% of all cancer deaths in the United States. According to the American Cancer Society's estimates for brain tumors in the United States, about 22,910 malignant brain tumors will be diagnosed in 2012 and about 13,700 people will die from these tumors. Despite numerous advances in treatment, the prognosis for these patients is poor, with a median survival of 4-8 months [1]. Surgical resection is considered the optimal treatment for most brain tumors. To minimize the trauma to the surrounding brain tissue during surgical resection, Endoscopic Port Surgery (EPS) was developed [2]. EPS is a minimally invasive technique for brain tumor resection which minimizes tissue disruption during tumor removal. However, because of the lack of a good continuous imaging modality for intraoperative intracranial procedures, it is extremely challenging for surgeons to remove brain tumors precisely and completely without damaging surrounding brain tissue using traditional surgical tools. As a result, patients may develop hemiparesis, cognitive impairment, or stroke after the procedure.

To overcome the above mentioned limitations, we propose to develop a highly dexterous meso-scale robot that can be operated in a MRI scanner. The robot will be operated through a narrow surgical corridor, which is 11 mm in diameter, dissected by the neurosurgeon. MRI will be used to supplement physicians' visual capabilities, resulting in less trauma to surrounding healthy brain tissue and more precise tumor removal during surgery.

1.2 Surgical Robotic Systems

Robotic systems are widely used in automation and machining because of the high accuracy that can be achieved during positioning or force control tasks. Over the past years, robotic systems have been successfully introduced to operating rooms for the same reasons. Such robotic systems provide the possibility of assisting and guiding the motion of physicians thus improving their performance. In comparison with industrial robots, surgical robotic systems require more stringent safety constraints because these systems directly interact with patients. Many groups have developed robot-assisted interventional systems, some of which have evolved to commercial systems such as ROBODOC®, ORTHODOC® (Curexo Technology Corporation.) and the da Vinci® surgical system (Intuitive Surgical, Inc.). The ROBODOC® surgical assistant system was developed together with the IBM Watson Center. A five Degree of Freedom (DOF) SCARA robot (manufactured by Sankyo Seiki) was custom designed for total hip arthroplasty (surgical repair of a joint). The system consists of a robotic arm and a PC-based Three-Dimensional (3-D) planning station called ORTHODOC®. The da Vinci® system con-

sists of a surgeon's console and a patient-side cart with four interactive robotic arms controlled by the console. Three of the arms are for tools that hold objects, such as a scalpel, scissors, or electrocautery instruments. The fourth arm is for an endoscopic camera with two lenses that gives physicians full stereoscopic vision from the console. The da Vinci® system also scales, filters and translates the physician's hand movements into more precise micro-movements of the instruments, which operate through small incisions in the body.

In addition to commercialized systems, Webster *et al.* [3] built a snake-like miniature flexible active cannula which is composed of concentric, pre-curved tubes and is capable of following curved paths in soft tissue or open space. Degani *et al.* [4] developed a Highly Articulated Robotic Probe (HARP) that can exploit its snake-like structure to navigate in a confined anatomical environment while minimally interacting with the environment along its path. Xu and Simaan [5] presented a multiple-backbone continuum robot which can be potentially used for minimal invasive surgery. These kinds of snake-like or continuum robots have a limitation that they can only be bent to a continuous curve, which limits its application especially in a space constrained environment. Robotic technology is now regularly used in minimally invasive surgery and to guide instruments in various surgical procedures. A detailed review of recent developments in medical robotics for minimally invasive surgery can be found in [6].

1.3 Neurosurgical Robotic Systems

In 1988, Kwoh *et al.* [7] proposed to use an industrial PUMA® 200 robot to perform brain tumor biopsy. The robot was used to hold and manipulate a needle guide through which a biopsy needle can be inserted. Several Computed Tomography (CT) images were taken and used to calculate the stereotactic coordinates of the target tumor before the biopsy procedure. Once the tumor is located, a control command will be sent to the robot and move it to the target location. The experimental results showed that the robotic assisted procedure is faster than a manual procedure with an accuracy of 2 mm and repeatability of 0.05 mm. Three years later in 1992, Drake *et al.* [8] used a similar system to control a surgical retractor. Although the industrial robot was modified for these work, its design was not suited for surgical application. MINERVA, developed by Burckhart *et al.* [9], had five DOFs: three linear axes and two rotary axes. It was designed to be operated inside a CT scanner for brain tumor biopsy. It was the first neurosurgical robotic system that could be guided through real-time CT images, allowing physicians to change the trajectory as the operation goes. This is an important feature since the brain tissue moves and deforms during the operation. The real-time images can compensate for these shifts and deformations. However, patients had to be inside the CT scanner during the operation which is not safe for the patients due to the radiation exposure. Moreover, the system could only perform single-DOF incursions.

Benabid's [10] group in Gernoble University developed a six-DOF robotic manipulator for brain tumor biopsy called NeuroMate®. The system used preoperative CT or MR images to position a cannula or probe for biopsy deep brain tumors. The system

computed the relative position of the robot end-effector and patient's anatomy using a calibration cage attached to the patient's head. There were fiducial markers on the cage which served as reference points in the CT or MR images. The system was later commercialized by Integrated Surgical Systems, Sacramento, CA, and was known NeuroMate®. NeuroMate® was approved by Food and Drug Administration (FDA) and has been used for more than 1000 cases [11]. Hongo *et al.* [12] developed a telecontrolled robotic platform for minimally invasive neurosurgery, called NeuRobot. It could be used to perform sophisticated surgical procedures through surgical openings of about 10 mm in diameter. The end-effector of the robot was a rigid cylinder which was 10 mm in diameter and 17 cm long. There were an endoscope, irrigation and suction channels, and three robot arms embedded in the cylinder. The robot arms had three DOFs: rotation, swing of neck, and forward/backward motion. A bipolar coagulation system was integrated to the NeuRobot® and two micro-forceps were connected to an electric surgical unit. The system has been used for a clinical trial to remove a portion of a tumor from a patient with a recurrent, atypical meningioma. The system was integrated with a surgical simulation console called ROBO-SIM®. ROBO-SIM® was designed to work with patients' diagnostic images from MRI, CT or ultrasound. The images could be loaded to the system and used to plan and simulate neurosurgery steps. The steps included the definition of the trepanation point for entry into the skull and the target point within the depth of the brain, checking the surgical track and doing virtual trepanations (virtual craniotomy) [13]. Recently in 2012, NeuRobot® has been clinically used for an endoscopic neurosurgery [14].

NeuroMaster was designed and developed by Liu *et al.* [15] for cerebral hemor-

rhage therapy, tumor biopsy, and tissue stimulation with an electrode. The systems consisted of a 5-DOF robot arm, a vision system of two cameras for intro-operative imaging, and a preoperative planning system. The planning system was used to reconstruct the tumor and the skull to provide an intuitive 3D display based on CT or MRI images. Physicians could then use the reconstructed 3D image for pre-operative planning. The vision system used the markers fixed to patient's head and robot end-effector for positioning. The robot arm can be controlled autonomously based on the pre-operative planning or interactively through the control joy sticks. The maximum positioning error was 2.5 mm, and the average error was 1.5 mm. The first clinical trial was done on August 4, 2003 and a remote surgery was conducted successfully on September 10, 2003. Another system used camera for positioning is the PathFinder® [16]. PathFinder®is an image-guided robotic system that was designed for neurosurgery. The system consisted of a planning workstation and a robotic arm which had a six DOFs, and was mounted on a wheeled trolley. Physicians can specify a target and a trajectory on the planning workstation with 3-D CT images [17] and the end-effector of the robotic arm will follow the trajectory by identifying reflectors attached to the patient's head using a camera attached to it, which differs from other neurosurgical robotic systems. The positioning accuracy was reported to be in sub-millimeter [18] and 2.7 mm [19], comparing to the 1.5 mm accuracy of the NeuroMaster robot system [15] and the 1.95 mm of the NeuroMate® [10].

Shamir *et al.* [20] developed an image-guided system to precisely guide needle or probe in minimally invasive neurosurgical procedures. The system used a MARS robot [21] with a 3D scanner and a navigation system to automatically position the robot with respect to predefined targets in pre-operative CT/MRI images following an anatom-

ical registration with a intraoperative 3D surface scan of the patient's facial features. The experimental results on an *in-vivo* test showed that the positioning error of phantom targets was 1.7 mm, which was close to the required 1-1.5 mm clinical accuracy in many keyhole neurosurgical procedures. The system was relatively compact and inexpensive (USD 50K) compared to the NeuroMate and the PathFinder (USD 300K). A detailed review of robotic neurosurgery can be found in [6, 22].

1.4 MRI-Compatible Robotic Systems

MRI is an excellent modality to provide high contrast images of different soft tissues such as the brain, muscles, the heart, and cancers. The high-contrast MR images can provide high-quality anatomic data resulting in better diagnostic accuracy compared to other medical imaging techniques such as ultrasound and CT [23]. Moreover, CT leads to radiation exposure and MRI uses no ionizing radiation. MRI scanners have been widely used for brain tumor diagnosis and its importance is recognized in that it is often difficult for even the most experienced neurosurgeon to accurately distinguish a tumor from healthy brain tissue based on appearance, texture or feel of the tissue. MRI supplements the physician's visual sense in a way that no other imaging device can achieve. In many ways, the MRI has revolutionized the ability of the neurosurgeon to obtain complete tumor resection without jeopardizing normal tissues [24] with early evidence suggesting that its use is associated with improved survival rates [25].

Several MRI-compatible surgical robotic systems have been developed by the research community. A MRI-compatible device for image-guided biopsy and therapeutic

procedures in the prostate was developed by Krieger *et al.* [26, 27]. The device was mainly constructed of plastic materials, while small metallic parts were kept to a minimum. The system was manually positioned and actuated, and the motion was monitored by active fiducial markers made of small RF coils placed at known areas of the device. The system has been tested in both *ex-vivo* and *in-vivo* studies and the experimental results demonstrated that the accuracy of placing a needle was within 2 mm. Wang *et al.* [28] built a MRI-compatible neural interventional robot using a piezoelectric actuator system. Kokes *el al.* [29] developed a MRI-compatible 1-DOF needle-driver system for Radio Frequency Ablation (RFA) of breast tumors using hydraulic actuation. Yang *el al.* [30] improved Kokes' design using pneumatic actuation with long transmission tubes. The above mentioned robotic systems are MRI compatible, but they cannot be used to reach the target which is not in the "line-of-sight". A more broad review of MRI-compatible robotic systems can be found in [31].

The potential of MRI-compatible robotic systems is that the motion of robots can be seen and controlled through MR images, resulting in reliable minimally invasive surgery with less tissue disruption, smaller incisions and shorter recovery time than traditional open surgeries. However, the commonly used materials, sensors and actuators in conventional robotic systems interfere with the static magnetic field, switching magnetic field gradients and Radio Frequency (RF) pulses emitted and detected by the MR scanners [32]. Therefore, the main challenges in developing MRI-compatible robotic systems are the selection of materials and the development of sensing and actuation techniques.

The choice of materials for instrumentation is important for developing MRI-compatible systems. Schenck [33] has done extensive work to investigate the influence of magnetic

susceptibility on the MRI compatibility of materials. The author divided the materials that can be used in a MRI environment into three groups. Materials in the first group, such as nylon and polyetheretherketone (PEEK), produce essentially no image abnormality. Materials in the second group, such as brass and zinc, produce noticeable image distortion, but it would not be significant for most applications. Materials in the third group, such as titanium and aluminum, produce obvious artifacts, but would still be acceptable for some applications.

In general, no ferromagnetic components should be brought into the MRI room. Several non-ferromagnetic metals, such as aluminum and brass, are widely used for fixation components and stereotaxic frames [34] because they are rigid and easy to machine. Polymers, such as nylon and PEEK, lead to negligible artifacts in the MR images and can be used within or close to the imaging region. The choice of proper actuation techniques is a central issue in the development of robotic systems and significantly determines the performances of the system. To choose a proper actuation technique that can be used in a MRI environment is even more difficult because of the safety and compatibility constraints due to the strong magnetic field imposed by the MRI scanner. Therefore, traditional actuators that are based on electromagnetic principles are not acceptable for use in a MRI-compatible system. The commonly used MRI-compatible actuation techniques can be roughly divided into four groups; they are mechanical transmission, pneumatic, hydraulic and electric actuation. However, a good actuation system usually involves a combination of several actuation principles. A detailed review and comparison of different MRI-compatible actuation techniques are given in [35, 36]. The authors analyzed different actuation principles based on MRI compatibility and the quality of force feedback

that can be realized. Since choosing a suitable actuator is a major topic of this research, a detailed review of different MRI-compatible actuation techniques will be discussed later in Chapter 3.

1.5 MRI-Compatible Neurosurgical Robotic Systems

Regarding to the MRI-compatible robotic systems that are especially designed for neurosurgical purposes, Masamune *et al.* [37] first developed a MRI-compatible manipulator dedicated to neurosurgical applications. The device was designed to be mounted on the patient couch and above the head of the subject, providing six DOF for MR guided stereotactic needle biopsies. Non-magnetic piezo-ultrasonic motors were used to actuate the robot and optical rotary encoders were used for position feedback. The robot was made of PET, PEEK®, Delrin®, non-magnetic steel, brass, aluminum and ceramics. In the phantom experiment, the tip of the needle reached the target within 3 mm. This error was caused mainly by the limited image resolution of the MRI. The MRI compatibility tests revealed that when the system was actuated, the ultrasonic motors substantially deteriorated the image quality and it was required to power off the motor drivers during MR scanning.

Another well-known MRI-compatible neurosurgical robotic system, named neuroArm, was developed at the University of Calgary by Sutherland *et al.* [38]. NeuroArm was specifically designed for neurosurgery applications, capable of performing both microsurgery and biopsy applications. The system consisted of a computer workstation, a control cabinet and two robotic arms. The computer workstation provided a field camera

view, a single channel view from the surgical microscope and MR images, which are used for surgical planning. The control cabinet had two hand controllers with force feedback capabilities and was able to controlled the two arms remotely from outside of the MRI room. The two robotic arms were made of MRI-compatible materials such as titanium, PEEK® and Delrin® and actuated by 16 ceramic piezo-ultrasonic motors. Each arm had six revolute joints and a 3-DOF force sensor providing the sense of touch attached to the end-effector. The end-effector was designed to hold various surgical devices such as micro scissors, bipolar forceps, suction device and needles. By using different tools, NeuroArm is able to cut and manipulate soft tissue, suture, biopsy, electrocauterize, aspirate, and irrigate. Those tools were superimposed on the MR images, providing real-time visual feedback during intracranial procedures. Typically, the human hand can steady itself and move in increments of one or two millimeters. NeuroArm can move in increments of 50 μm. The first clinical trial of the system was done in 2008 to remove an egg-sized brain tumor. More information about this project is available online in [39].

Cole *et al.* [40] also used piezo-ultrasonic motors to develop a MRI-guided robotic system for deep brain stimulation electrode placement. A parallelogram linkage and cable-driven mechanism were also used in the system. The system had six DOFs and relied on optical encoders placed on the joint actuators for position feedback. The robot used pre-operative MR images through open source image guided therapy software [41] for selecting target point and trajectories for the electrode insertion. In addition to piezo-ultrasonic actuators, Raoufi *et al.* [42] used hydraulic cylinders and a pneumatic motor to design a MRI-guided robotic system for brain biopsy. The system consisted of a navigation module and a biopsy module. The navigation module was a parallel mechanism

actuated by six hydraulic cylinders and used to adjust the linear displacement and orientation of the biopsy module. The biopsy module was actuated by a pneumatic motor and used for needle insertion. However, no experimental results were available on this device.

1.6 Research Objectives

Based on the above review of current state-of-art neurosurgical robotic systems, a simple comparison between different systems is shown in Table 1.1. The table clear shows that most neurosurgical robotic systems relied on pre-operative images to position the robot, and was prone to errors when the brain shifted. Although the MINERVA can be guided through real-time CT images, it is not safe for the patient due to the radiation exposure. In addition, most of the systems can only be used for needle insertion procedures, such as tumor biopsies, catheter insertion, deep brain stimulation, aspiration and evacuation of deep brain hematomas, and minimal access craniotomies, which are not able to remove brain tumors completely. The only system that can be guided through real-time MR images and used for brain tumor removal is the NeuroArm. However, NeuroArm cannot be used to remove a tumor that is not in the line-of-sight. Moreover, it is bulky and expensive.

Table 1.1: Comparison between different neurosugical robotic systems.

System	MRI-compatible	Function	Work outside of the line-of-sight	Image guidance
Kwoh *et al.* [7]	No	Needle insertion[1]	No	Pre-operative CT
Drake *et al.* [8]	No	Surgical retraction	No	Pre-operative CT
MINERVA [9]	No	Needle insertion[1]	No	Real-time CT, pre-operative MRI
NeuroMate [10]	No	Needle insertion[1]	No	Pre-operative CT/MRI
NeuRobot [12]	No	Multi-function	Yes, endoscopic surgery	Pre-operative CT/MRI, real-time camera
Pathfinder [16]	No	Multi-function	No	Pre-operative CT, real-time camera
NeuroMaster [15]	No	Needle insertion[1]	No	Pre-operative CT, real-time camera
MARS [20, 21]	No	Needle insertion[1]	No	Pre-operative CT/MRI, real-time 3D scanner
Masamune *et al.* [37]	Yes	Needle insertion[1]	No	Pre-operative/continuous MRI
NeuroArm [38]	Yes	Multi-function	No	Pre-operative/continuous MRI
Cole *et al.* [40]	Yes	Needle insertion[1]	No	Pre-operative/continuous MRI

[1]The needle Insertion procedure includes tumor biopsies, catheter insertion, deep brain stimulation, aspiration and evacuation of deep brain hematomas, and minimal access craniotomies.

To overcome the above-mentioned limitations of current neurosurgical robotic systems, we envision developing a MINIR. MINIR is MRI-compatible, so that frequently-updated MR images can be used to provide real-time virtual visualization of the target tumor for physicians while most state-of-art neurosurgical robots relied on pre-operative images. MINIR would be inserted through a surgical corridor carefully dissected by the neurosurgeon about 11 mm in diameter. Figure 1.1 shows a schematic of the envisioned system of MINIR. We envisioned MINIR to be under the direct control of a physician with visual information obtained exclusively from frequently-updated MRI. Because of the multiple DOFs of MINIR, it would be able to work outside of the "line-of-sight" of the entry trajectory while most state-of-art neurosurgical robots only has the ability of accessing the target that is in the "line-of-sight". MINIR can resect a tumor by positioning an instrument that liquefies tissue and washes out the debris like any human neurosurgeon. Consequently, the goal of this research is to design, develop and test prototypes of MINIR. Moreover, creating proper control algorithms are also key tasks of this research.

1.7 Thesis Outline

In the present chapter of this dissertation, we have introduced the motivations of conducting this research, given a brief review of some related work of surgical robotic systems and summarized the challenges of developing MINIR. In Chapter 2, we give a detailed review of MRI-compatible actuation techniques and propose to use SMA actuators for MINIR. We also summarize basic types of SMA actuation and their advantages. In Chapter 3, We discuss the fundamentals of SMAs and give a review of their theoretical models

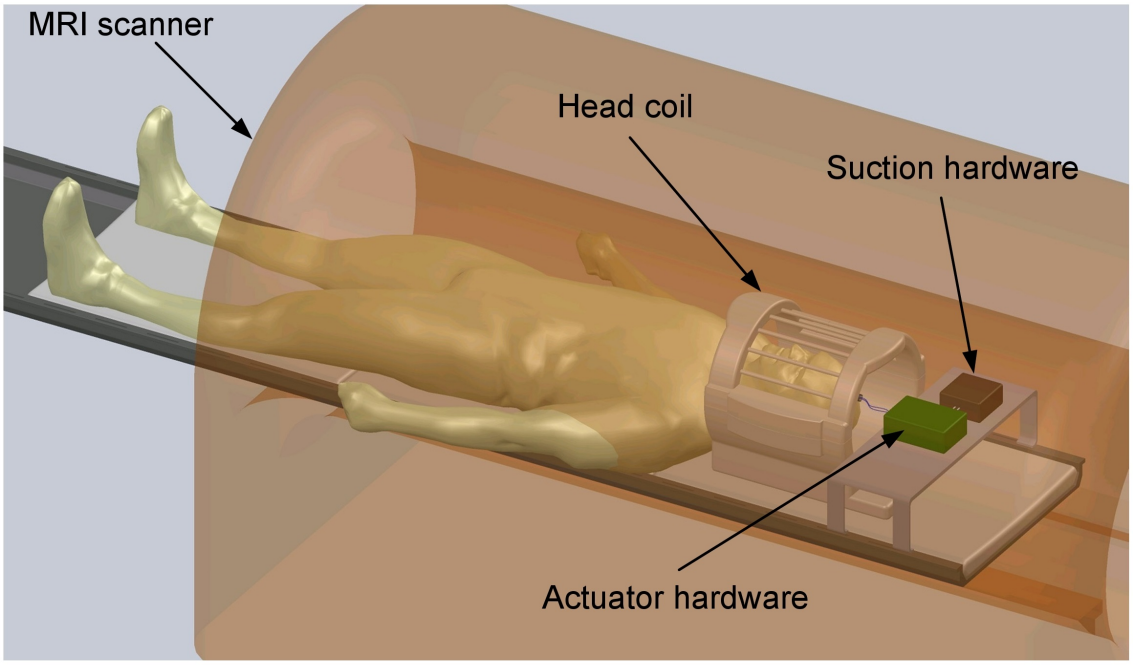

(a)

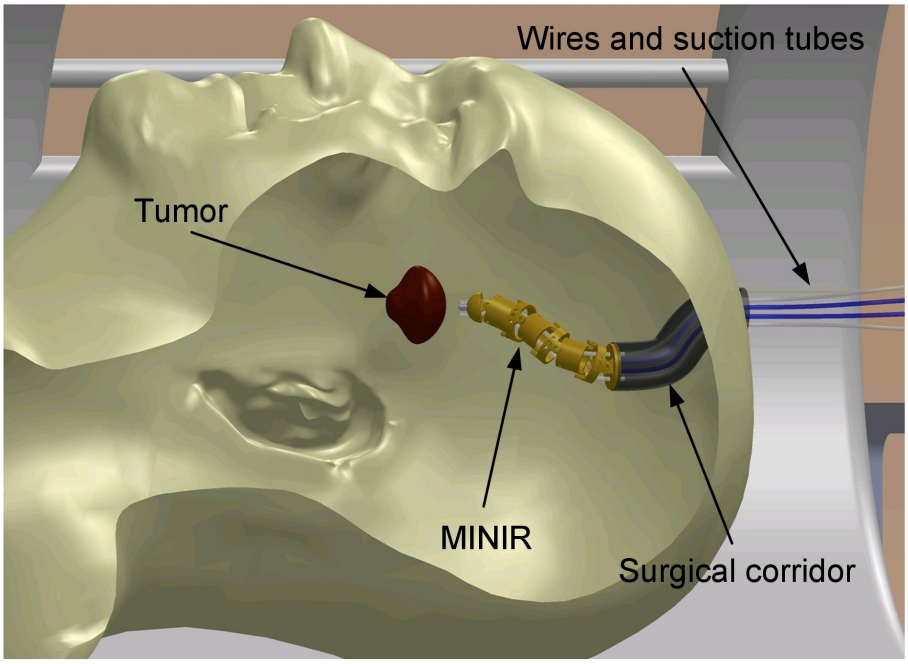

(b)

Figure 1.1: The schematic of MINIR: (a) MINIR can be operated inside a MRI scanner and (b) a close-up view of MINIR when operated inside a human brain through the surgical corridor.

and applications. We also outline the important parameters for the theoretical models of SMA and present a systemic procedure to measure those parameters using customized experimental setup. In Chapter 4 and Chapter 5, we present the design and experimental results of our second and third generation of MINIR, respectively. Detailed design considerations, actuation methods, control strategies and MRI compatibility evaluations are discussed as well. Finally in Chapter 6, we conclude the contributions of this research and point out some possible directions which could potentially extend this research.

Chapter 2

MRI-Compatible Actuators

This chapter gives a more detailed review of current state-of-art MRI-compatible actuation techniques. We roughly divided MRI-compatible actuation techniques into five categories: they are mechanical transmission, pneumatic actuation, hydraulic actuation, electric actuation and SMA-based actuation. In the last section of this chapter, we summarize the advantages and limitations of each actuation technique and propose to use SMA-based actuator to develop MINIR.

2.1 Mechanical Transmission

Mechanical transmission, such as cable and shaft transmissions, are commonly used to transfer motion and force over a long and narrow route while taking up very little space. Therefore, it has been used in many minimally invasive surgical robotic systems to allow working within limited workspace. Cavusoglu *et al.* [43] developed a laparoscopic telesurgical workstation using DC motors and cable driven mechanisms. The system consisted of a 4-DOF parallel mechanism and a 2-DOF robotic wrist mounted on the platform of the parallel mechanism. The parallel mechanism was used to control the position and orientation of the robot wrist. The robotic wrist was 10 cm long, 10 mm in diameter and actuated through tendons driven by DC motors. By using the tendon driven mechanism, the DC motors were able to be placed away from the robotic wrist so that the robotic

wrist can be used for suturing and knot tying through a small incision. Simaan *et al.* [44] developed a snake-like robot which could possibly be used for minimally invasive surgery of the upper airway. The robot was a 2-DOF robot composed of several disks and four super-elastic NiTi tubes. This prototype was 4.2 mm in diameter, 28 mm long, and the super-elastic NiTi tubes were 0.66 mm in diameter. The center tube was used as the primary backbone while the remaining three tubes were pushed and pulled manually to move the robot. Ota *et al.* [45] developed a highly articulated robotic surgical system to enable minimally invasive intrapericardial therapeutic delivery through a subxiphoid approach. The robot was composed of 50 rigid cylindrical links serially connected by three cables. The three cables were connected to the distal link to control the orientation of it by pushing and pulling the corresponding cables, respectively. The commercialized *da Vinci*® surgical system used cable driven mechanisms for actuation as well. However, those robotic systems are far from MRI-compatible due to the materials and actuators that were used in the systems.

Using mechanical transmission, motion and force of actuators can be transmitted from outside the MRI scanner or even outside the MRI room and therefore reduces electromagnetic interference caused by the actuators. This also allows remote actuation from outside the MRI room. Therefore, it can be used to develop MRI-compatible robots provided proper materials were selected. Chapuis *et al.* [46] developed a MRI-compatible haptic interface using cable transmission. The motor of the haptic device was outside the MRI room and nine meters away from the slave device which was in the MRI scanner. The experimental tests showed that the device worked properly with nine meters of transmission and the bandwidth was higher than that of a similar device using hydrostatic

transmission of similar length. However, no MRI compatibility test was presented in the paper, and slippage, friction and cable routing could be issues to use this device in practical applications. Krieger *et al.* [26] developed a MRI-guided manipulator to position the needle guide for biopsy, fiducial marker placements, and therapy delivery in prostate interventions. The system was controlled manually through two flexible shafts that transmit force and motion to the needle guide. Two tracking coils were placed on the needle guide to track the position of it and the average positioning error was 4.8 mm with a maximum of 8.3 mm. MRI experimental results showed that the manipulator was MRI-compatible, however, the manipulator made the procedures slower than using traditional techniques and provided low positioning resolution and accuracy since it was actuated manually. In 2010, Krieger *et al.* [27] further integrated piezo-ceramic motors to the manipulator. The prototype provided automatic positioning of the needle guide and the needle was then inserted manually. The MRI compatibility tests of the robot showed no reduction of Signal-to-Noise Ratio (SNR) in the motor off configuration and a 40% to 60% reduction in SNR when the motors were on. The paper also indicated that the RF shielding can significantly improve MR image quality. The main limitation of mechanical transmission is the requirement of fixed supporting and guiding structures, which reduces the system flexibility. Moreover, redirection mechanisms of cable transmission increase complexity and friction.

2.2 Pneumatic Actuation

Pneumatic actuation techniques have been used in several MRI-compatible manipulators because pneumatic cylinders can be made of MRI-compatible materials. Therefore, they can be used close to or within the imaging region of MRI scanners. The long and flexible pneumatic tubes allow easy placement and adjustment of the manipulators in a MRI room and the air compressor, air valves and controllers can be located outside of the MRI room. Air leakage is not problematic and no return path is required since air can be directly released to the environment. For these reasons, pneumatic actuation seems ideal for developing MRI-compatible robots. However, precise positioning control is difficult due to the friction in the pneumatic cylinders and time delay caused by compressible air and long transmission tubes.

Bone and Ning [47] proposed two control algorithms to address the positioning issue of a pneumatic cylinder and these two control algorithms were extensively tested in the paper. The Root-Mean-Square (RMS) deviation of the sliding-mode control based on a linearized plant model (SMCL) was 0.51 mm over the motion range from 3 mm to 250 mm, and it was 0.42 mm for the sliding-mode control based on a nonlinear plant model (SMCN). Fischer *el al.* [48] developed a pneumatic robot for prostate needle placement. They used high-speed piezoelectric valves to increase the bandwidth of the controller and shorten pneumatic tubes by placing the controller inside the MRI room to reduce the time delay. The robot controller was placed 3 m from the edge of the scanner bore. To avoid bringing noise to the MRI scanner, the controller was shielded and had no external electrical connections since electrical connections could act as antennas, bringing

noise into the scanner. MRI compatibility tests showed no more than 5% loss in average SNR when the robot was operated. Needle alignment accuracy of the robot under servo pneumatic control was better than 0.94 mm RMS per axis. Yang *el al.* [30] presented the design and control of a MRI-compatible robot for RF ablation of breast tumor using pneumatic actuation. Long transmission tubes were used so that the robot controller could be placed outside the MRI room. The authors modeled the entire pneumatic system with long transmission tubes as a first-order system with time delay. Sliding-mode control was adopted and the experimental results demonstrated that the positioning error was less than 1 mm and the system was MRI-compatible.

Pneumatic actuation has also been adapted to develop MRI-compatible motors. Stoianovici *et al.* [49] presented their design and experimental results of a MRI-compatible pneumatic stepper motor, PneuStep. The motor was entirely made of non-magnetic materials such as plastics, ceramics, and rubber, and the position sensing was provided by fiber optics. Each PneuStep motor required four pneumatic tube, four optic fibers for incremental encoding, and two optic fibers for a limit switch sensor. The motor has been applied to a robotic system for prostate brachytherapy by Patriciu *el al.* [50]. The systems consisted of a 5-DOF robot actuated by PneuStep motors and a special brachytherapy end-effector used for needle insertion and seed deployment. The robot was able to position the end-effector with a resolution of 0.055 mm. The performance of the robotic system matched the requirements of the clinical applications for low speed ($<$20 mm/s) and high accuracy ($<$0.5 mm) operations. Sajima *et al.* [51] designed and developed a MRI-compatible pneumatic stepping actuator and a MRI-compatible needle guiding manipulator. The manipulator had two DOFs and was actuated by two pneumatic stepping

actuators. The actuators and the manipulator were made of resin to ensure the MRI compatibility of the system. Other non-MRI-compatible hardware, such as electromagnetic valves, the air compressor and controllers were set outside the MRI room and connected to the actuators through eight-meter-long tubes. The average positioning error was 0.43 mm and the maximum error was 0.8 mm and no SNR reduction was observed when the actuators were on.

2.3 Hydraulic Actuation

Hydraulic systems can be used either as actuators, where a hydraulic pump generates pressure used to actuate a piston located at some distance, or as closed hydrostatic transmission, linking a master to a slave piston in a closed-loop manner. Similar to pneumatic systems, the installation of hydraulic systems is flexible because of the long and flexible transmission tubes. The liquid for hydraulic systems is incompressible which suggests that hydraulic transmission can be used for both positioning tasks and force feedback applications.

Kim *et al.* [52] developed a hydraulic-driven manipulator for minimally invasive liver surgery. The manipulator used hydrostatic transmission to transmit force and motion of ultrasonic motors placed far from the MRI scanner. Beryllium copper was used to make the tip forceps of the manipulator and aluminum, brass, titanium were used to build the manipulator structure. MRI compatibility tests showed that the SNR of the MR images dropped from 275.6 to 174.8 after the manipulator was actuated. During the experiments, the beryllium copper forceps were in the imaging region and other structure

was 30 mm from the imaging region. No positioning accuracy was reported in the paper. Kokes *et al.* [29] developed a MRI-compatible needle driver system for RFA of breast tumors using hydraulic actuation. The system structure was made of polypropylene and carbon-fiber rods to ensure the MRI-compatibility. Hydraulic pump and valves were located in the control room since they are not MRI-compatible. The system can be operated under continuous MRI while being teleoperated by a haptic feedback device from outside the MRI room. The RFA needle was mounted to a MRI-compatible force sensor so that the forces that were experienced by the RFA probe could be measured and sent to the haptic device. The MR images showed negligible noise which meant that the needle driver was MRI-compatible and did not introduce significant artifacts in the image, enabling its usage within the MRI environment during continuous imaging. The maximum positioning deviation of the needle was calculated to be 2.54 mm and the image with worst quality had an SNR of 5.2.

Ikuta *et al.* [53] developed an active catheter which could be safely used in human blood vessels. The current prototype had two multipurpose channels, each with a diameter of 0.5 mm. The catheter was driven by a hydraulic system with micro valves and had multiple DOFs. The entire catheter was made of soft silicone rubber and thus it was MRI-compatible. The authors also proposed a new method called "pressure pulse drive" to control the bending of the catheter. The experimental results showed that the bending motion of the catheter can be precisely controlled by the pulse pressure and pulse width. Yu *et al.* [54] developed two comparable haptic interface devices, one with hydrodynamic and the other with pneumatic actuation, to control a 1-DOF manipulator in a MRI scanner. The paper demonstrated that both devices were MRI-compatible, showed no SNR drop

after actuation and yielded no artifacts in fMRI images in a 3-T scanner. Experimental results showed that the hydrodynamic actuation can achieve smoother motion, higher positioning accuracy, and better robustness against force disturbances than the pneumatic actuation. On the other hand, pneumatic actuation had a faster response and was easier to maintain because of its simpler system infrastructure. Moreover, the leakage of air does not cause any problem.

In general, pneumatic actuation is more favorable for the applications that require fast response, whereas hydrodynamic actuation is recommended for applications that require higher position accuracy, slow and smooth movements. Both hydraulic and pneumatic transmissions are flexible and can be easily adapted to the MRI environment. The limitations of hydraulic actuation are that the fluid viscosity and joint friction (known as Stribeck friction) make the transmission nonlinear and difficult to control. Moreover, the infrastructure is complicated because it requires additional mechanisms to convert electro-mechanical power into hydraulic power. Moreover, leakage is not be acceptable in medical applications.

2.4 Electric Actuation

Electric actuators convert electric energy to mechanical energy directly, which is in contrast to electromagnetic actuators that require ferrous or magnetic components to convert electric energy to magnetic energy. Therefore, they can be used in MRI environments. However, these actuators usually require high voltage to actuate and have to be placed at a minimum distance from the imaging region. Shielding and signal filtering may be

necessary in some cases [36].

Piezoelectric and ultrasonic motors are currently the most widely used electric actuators in MRI-compatible robotic systems. Fischer *et al.* [48] used piezoelectric servo valves in a MRI-compatible robotic system for prostate needle placement. The authors used piezoelectrically actuated proportional pressure valves for the pneumatic controller which was placed close to the MRI scanner. By reducing the distance between the pneumatic valves to the cylinders on the robot, the time delay of the system could be minimized. Another advantage of using piezoelectric valves was the rapid response time (4 ms) which could significantly increase the bandwidth and update rate of the controller. Experimental results showed that the MR compatibility of the system including the robot and controller was excellent with no more than 5% loss in average SNR with the robot operational. Yang *et al.* [55] extended their work of a 1-DOF needle driver system [30] to 4-DOF. The 4-DOF robot consisted of a parallel mechanism and a needle driver. The parallel mechanism provides one translational and two rotational degrees of freedom, while the needle driver provides the fourth degree of freedom that advances the needle. The parallel mechanism was actuated by three pneumatic cylinders and the needle driver was actuated with a piezo motor placed away from the imaging region. The positioning accuracy of the system was within 0.5 mm. The SNR dropped from 119.71 to 111.09 (7.2% drop) when the piezo motor was actuated. The author concluded that piezo motors could introduce noise in the MR images when actuated even with shielded cables passing through the filter panel. Therefore, piezo motors should be placed away from the imaging region.

Oura *et al.* [56] presented a 3-DOF versatile robot which was actuated by ultrasonic

motors for minimally invasive surgery. The robot consisted of a 2-DOF manipulation and a 1-DOF surgical tool. Although the ultrasonic motors were MRI-compatible, it produced significant noise in the MR images and could not be used directly in each joint. Therefore, the ultrasonic motors were placed away from the robot and transmitted motion and force to the robot through timing belts. The timing belts were made of rubbers and MRI-compatible. The average positioning error of each joint was 2.99 mm with a maximum of 9.58 mm. These errors were mainly caused by backlash and expansion of the timing belts. However, no MRI compatibility experiments were reported in the paper. Izawa *et al.* [57] described the development of a MRI-compatible manipulator actuated by ultrasonic motors. The manipulator was used to perform fMRI tasks of finger movements under continuous MRI. The prototype had a 2-DOF parallel link actuated by two ultrasonic motors with rotary encoders attached to the actuators for position sensing. The manipulator was tested in a 1.5-T MRI scanner and the SNR dropped from 206.3 to 203.7 (1% drop) during actuation. Harada *et al.* [58] proposed a surgical robotic system for intrauterine fetal surgery in an Open MRI. The system consisted of a flexible coil tube which was 150 mm long, 2.4 mm in diameter and could be bent manually. There was a 2-DOF mechanism at the end of the flexible tube. The mechanism included two ball joints and was driven using four cable, which can be bent up to 90° in any direction. The four cables were actuated by two ultrasonic motors. However, the prototype made in the paper was not yet MRI-compatible and therefore no MRI compatibility results were shown.

Carpi *et al.* [59] investigated the MRI compatibility of a new linear contractile actuator, developed with one of the best performing classes of electroactive polymer actuators: the dielectric elastomers. A typical dielectric elastomer actuator usually consists

of an insulating elastic material sandwiched between a couple of compliant electrodes. While applying high voltage, the actuator contracts and provides a thickness squeezing and an area expansion. The prototype actuator developed in the paper was 65 mm long with a cross section of 16 mm $\times$ 21 mm. The actuator was able to generate 0.5 N tensile force of stress when an electric field of 8 V/μm was applied but no displacement data was reported in the paper. MRI experiments showed that no image shift or distortion was observed during actuation and the loss of SNR was not significant (less than 0.5% for the worst condition when actuated).

2.5 SMA-Based Actuation

The advantages of SMA actuators over other conventional actuators are their large energy density, silent when during operation, environmental friendliness (no dust, no noise during operation), simplicity of mechanism, compactness and ease of miniaturization. The relatively large output force and stroke enable the design of simple actuation mechanisms. This is in contrast to complicated designs requiring gear reduction or motion amplification when employing conventional motors or other active materials, such as piezoelectrics. Low actuation voltages, low costs and reduced number of moving parts are additional advantages associated with SMA actuators.

Ikuta *et al.* [60] developed an active endoscope using SMA coils as actuators. Nakamura *et al.* [61] used SMA tubes to actuate active forceps for laparoscopic surgery. Ayvali *et al.* [62] developed a multi-DOF discretely actuated steerable cannula using SMA wires as actuators. Another important property of SMA is its MRI compatibility. SMA

has been tested in 1.5-T and 4.1-T MRI scanners and only a minor artifact was observed in the MR images [63]. Ikuta [64] compared the power/weight ratio of different types of actuators and found that when the weight is 100 g or lighter, SMA actuators have the highest power/weight ratio of almost 100 W/kg. This property indicates that SMAs have great potential for miniature actuators. SMA actuators can be used directly in many applications without additional mechanisms since they use only the shape recovery of the alloy and it can be achieved via Joule heating (resistive heating). The power circuitry for Joule heating is comparatively simple so that thin and flexible wires which do not interfere with the motion of the mechanisms can be used. Moreover, SMA actuators do not require any reduction gear system nor other friction mechanisms so they can work without producing dust particles and noise. According to the experimental results obtained in a super clean room [64], the cleanliness of SMA actuators while activated was much better than class 1000 (the number of particles of size 0.5 μm or larger permitted per cubic foot of air is less than 1000). Aside from the general advantages of SMA actuators discussed above, Nitinol (a most commonly used SMA) has excellent corrosion resistance and high biocompatibility [65] which make it extremely suitable for biotechnology and medical applications, and it has been successfully used in neurosurgical implants [66].

SMA actuators can be used to generate both linear motion, as shown in figure 2.1, and rotational motion, as shown in figure 2.2. There are typically three ways to use SMA as actuators. First, the one-way actuation as shown in figure 2.1(a). The SMA is pre-strained by an external force at a low temperature and then actuated to move element M in one direction. The second actuation type uses a bias spring with a SMA and is capable of moving the element M back and forth. The SMA is pre-strained at a low temperature

before being connected to the bias spring. When the SMA is actuated, the recovery force pulls the spring, thus the element M moves and the bias spring is stretched. Once the SMA is cooled, the force is released and the SMA is pulled back by the bias spring, thus completing the cycle as shown in figure 2.1(b). The third actuation type is the antagonistic actuation which includes two SMAs. The two SMAs are placed antagonistically and the element M can be controlled to move back and forth by cooling or heating the corresponding SMA as show in figure 2.1(c). In practice, the latter two arrangements are mostly used and the antagonistic setup is preferable because it can reduce the hysteresis effect since one of the SMA is heated while the other one cools. Another advantage of using antagonistic SMA actuators over a bias spring is, instead of providing passive biasing force or motion, both directions of motion can be actively controlled. This increases the controllability of the system. The bias-spring setup and antagonistic setup of SMAs can also be used to generate rotational motion as shown in figure 2.2(a) and figure 2.2(b), respectively.

2.6 Summary

To summarize, mechanical transmission such as cable and shaft transmissions are good to be used in minimally invasive surgical robotic systems since they can transfer motion and force over a long and narrow route while taking up very little space. However, they require fixed supporting and guiding structures which reduce the system flexibility and increases friction. The long and flexible transmission tubes make the placement and adjustment of pneumatic actuation and hydraulic actuation easy. In addition, they also allow the

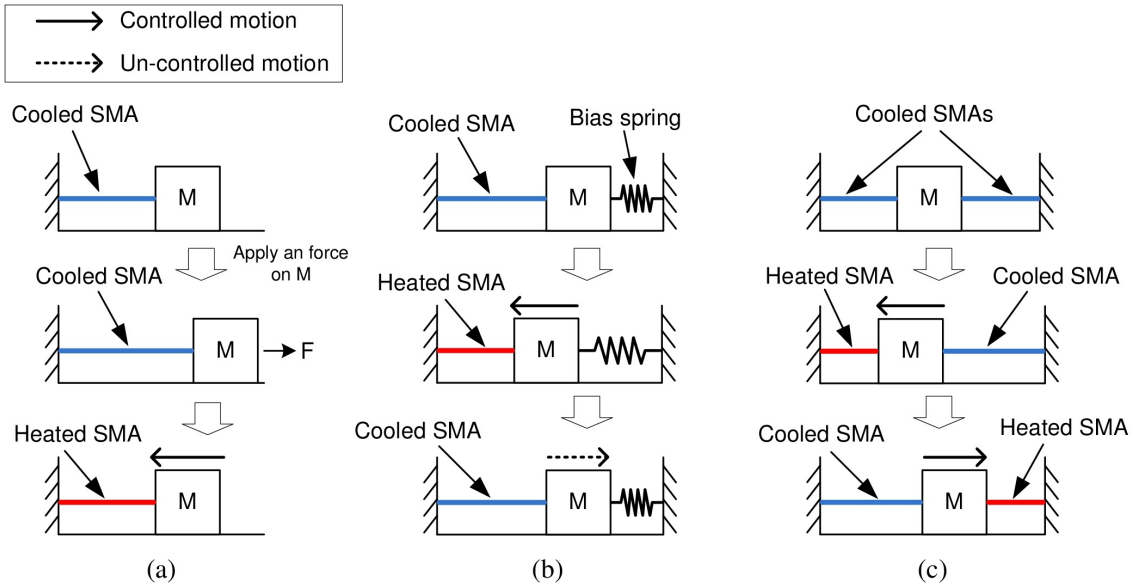

Figure 2.1: Different actuation types of using SMA for linear motion: (a) One-way actuation, (b) spring-biased actuation and (c) antagonistic actuation.

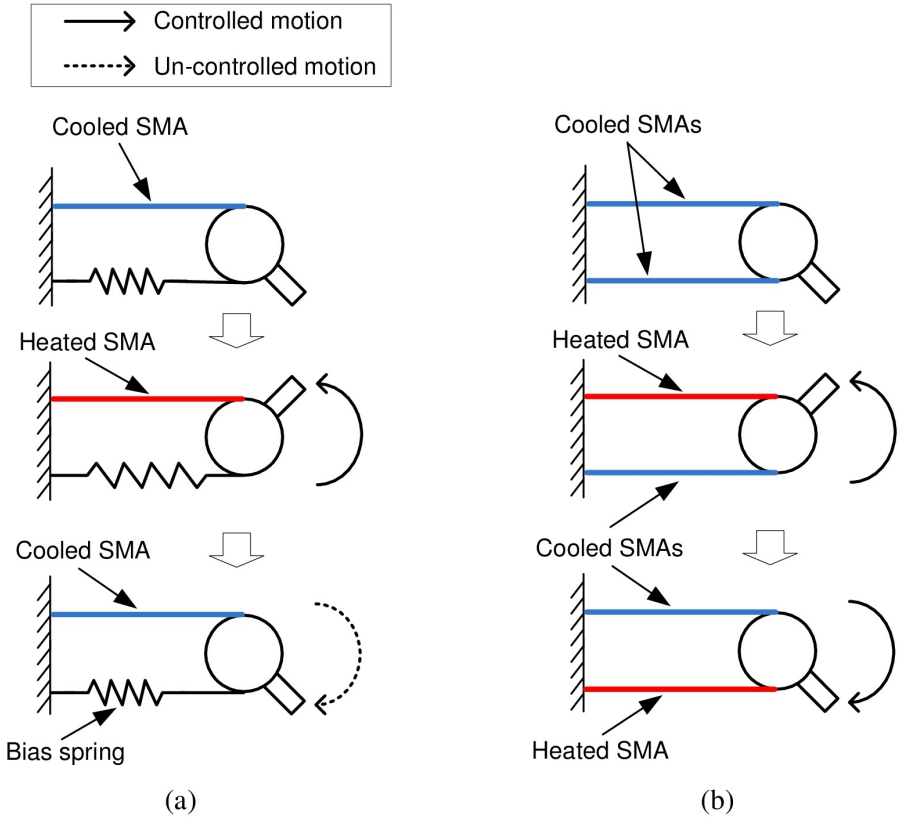

Figure 2.2: Different actuation types of using SMA for rotational motion: (a) Spring-biased actuation and (b) antagonistic actuation.

non-MRI-compatible components such as compressor, valves and controllers to be placed away from MRI scanners or even outside MRI rooms. This makes the pneumatic actuation and hydraulic actuation MRI-compatible. Precise positioning is difficult due to the time delay caused by compressible air for pneumatic actuation while hydraulic actuation can be used for smooth motion and precise positioning. Additionally, pneumatic actuation can be used for haptic feedback because the hydraulic fluid is in-compressible. However, fluid leakage is not be acceptable in medical applications while air leakage is not problematic for pneumatic actuation.

Electric actuators such as piezoelectric motors, ultrasonic motors and dielectric elastomers usually require high voltage to actuate and thus have to be placed at a minimum distance from the imaging region to prevent creating noises in MR images. Piezoelectric motors and ultrasonic motors are currently the most widely used actuators in MRI-compatible robotic systems. The advantages of these two kinds of motors include that they can be controlled precisely and are commercially available. Another advantage is the rapid response time which could significantly increase the bandwidth of the controller. Dielectric elastomers are MRI-compatible, however, the relatively large size and small output force makes they difficult to be used in practical applications. The advantages of SMA actuators are their large energy density, simplicity of mechanism, large output force and large stroke. SMA actuators are small, MRI-compatible and require low voltage to actuate, which makes it possible to use SMA actuators in the imaging region of MRI scanners. Moreover, low cost, excellent corrosion resistance and high biocompatibility are additional advantages of SMA actuators. However, the slow response is an issue of using SMA actuators.

Due to the leakage problem, hydraulic actuation is not considered for MINIR. Pneumatic actuation requires space for routing tubes, therefore, it is not suitable for MINIR. It is likely that ultrasonic actuators or piezoelectric actuators combined with mechanical transmission are the best actuation technique for MRI-compatible robotic systems. However, the high cost ($>$\$2000 for a set) make these techniques impractical for a multi-DOF system such as MINIR. SMA is low cost and commercially available in the form of rods, tubes, wires, springs and bars. Moreover, SMA wires are very easy to incorporate in actuation mechanisms. Thermal activation of the SMAs can also be accomplished conveniently and compactly by passing an electric current through the wires. The resistance of the wires causes a self-heating which activates the shape memory effect. Moreover, the low cost of SMA makes MINIR a disposable device which is preferable in medical applications. Therefore, we propose to use SMA-based actuators for MINIR in this research. A simple comparison of different MRI-compatible actuation techniques which are discussed in this chapter is show in Table 2.1 and it should be clear that using SMAs is a proper actuation method for MINIR.

Table 2.1: Comparison between different MRI-compatible actuation techniques.

Actuation Technique	Advantage	Disadvantage	MRI Compatibility
Pneumatic Actuation	– Flexible tubes lead to easy adjustment in a MRI room – Leakage is not problematic and no return path is required	– Lack of stability and stiffness – Difficult to control due to friction and compressible air	MRI compatible but not feasible for MINIR
Hydraulic Actuation	– Flexible tubes lead to easy adjustment in a MRI room – Could be used for haptic feedback – Good for slow and smooth motion	– Leakage could be an issue in medical applications – Friction could make control difficult – Infrastructure is complicated	
Electric Actuation	– Compact – Precise positioning – Fast response	– Causes significant noise in MR images if operated in the imaging region – Requires high voltage to operate	
Mechanical Transmission	– Transfers motion and force over a long and narrow route while taking up very little space	– Friction, cable slippage and cable routing could be issues – Requires fixed supporting and guiding structures which reduces system flexibility	MRI compatible and feasible for MINIR
Shape Memory Alloy	– Bio-compatible, compact and ease of miniaturization – High energy density – Could be trained to different shapes for different applications – Could be used within imaging region without causing significant noises in MR images – Low cost and disposable	– Slow response due to slow cooling	

Chapter 3

Shape Memory Alloy

This chapter discusses the background of SMA and the characterization procedures of finding important material parameters of SMA. Section 3.1 explains the mechanisms of the Shape Memory Effect (SME) as well as the definition of the transformation temperatures of SMA. Section 3.1 also contains previous work on modeling and controlling of SMA actuators. Section 3.2 deals with experimental characterization of SMA wires using a customized experimental setup and outlines the important parameters that are required for the theoretical model of a SMA. Detailed design and experimental procedures for characterizing SMA wires are discussed. The measured parameters of the SMA wire we used in this research are also presented. Most of the contents in section 3.2 are published in [67, 68].

3.1 Fundamentals of Shape Memory Alloy

SMA is a class of metallic alloys that have a special ability to memorize its original (trained) shape and recover large deformation on thermal activation. When a SMA is at a lower temperature than the transformation temperature, it can be deformed and hold the shape until heated above the transformation temperature. Upon heating, the SMA can recover to its original shape. This phenomenon is called SME. SME is caused by a transformation between martensite phase and austenite phase in the material. This transformation

can be traced to the lattice structure and the associated deformation mechanisms inside the material.

The most commonly used shape memory material is an alloy of nickel and titanium called Nitinol (Nickel titanium alloy developed at the Naval Ordinance Lab), which was discovered by Buehler *et al.* [69]. This material is a binary alloy of nickel and titanium (NiTi) in a ratio of 55% and 45% respectively. The recoverable strain of Nitinol is up to a maximum of about 8% [70], and it can generate extremely large forces during phase transformation because of its three- to four-fold increase in elastic modulus in the austenite phase compared with that in the martensite phase [71]. The large recoverable strain and the large recovery force provide Nitinol a good material to be used as actuators. In the typical use of SMA actuator, the material is usually pre-strained at a low temperature and it starts to recover upon heating. When the temperature reaches a specific temperature, the pre-strain in the SMA recovers completely, and this shape is retained on cooling to the initial low temperature. The deformation, heating, recovery and cooling cycle is repeatable for different pre-strains.

3.1.1 Shape Memory Effect

The SME occurs as a result of a reversible transformation between two phases in the SMA. The phase transformation depends on the stress applied to the material and the temperature in the material. Under a no stress condition, SMA exists in the martensite phase at low temperatures and the material transforms to the high temperature austenite phase on heating. If a deformation imparted to a SMA at a low temperature martensite

phase, the deformation will recover upon heating as the material transforms to the high temperature austenite phase. On subsequent cooling, the material returns to the martensite phase, but there is no further change in the shape of the material. Because the shape change occurs only during heating, this transformation is called the one-way SME as shown schematically in figure 3.1(a). Note that the austenite phase can exist in only one shape, while the martensite phase can have several different shapes.

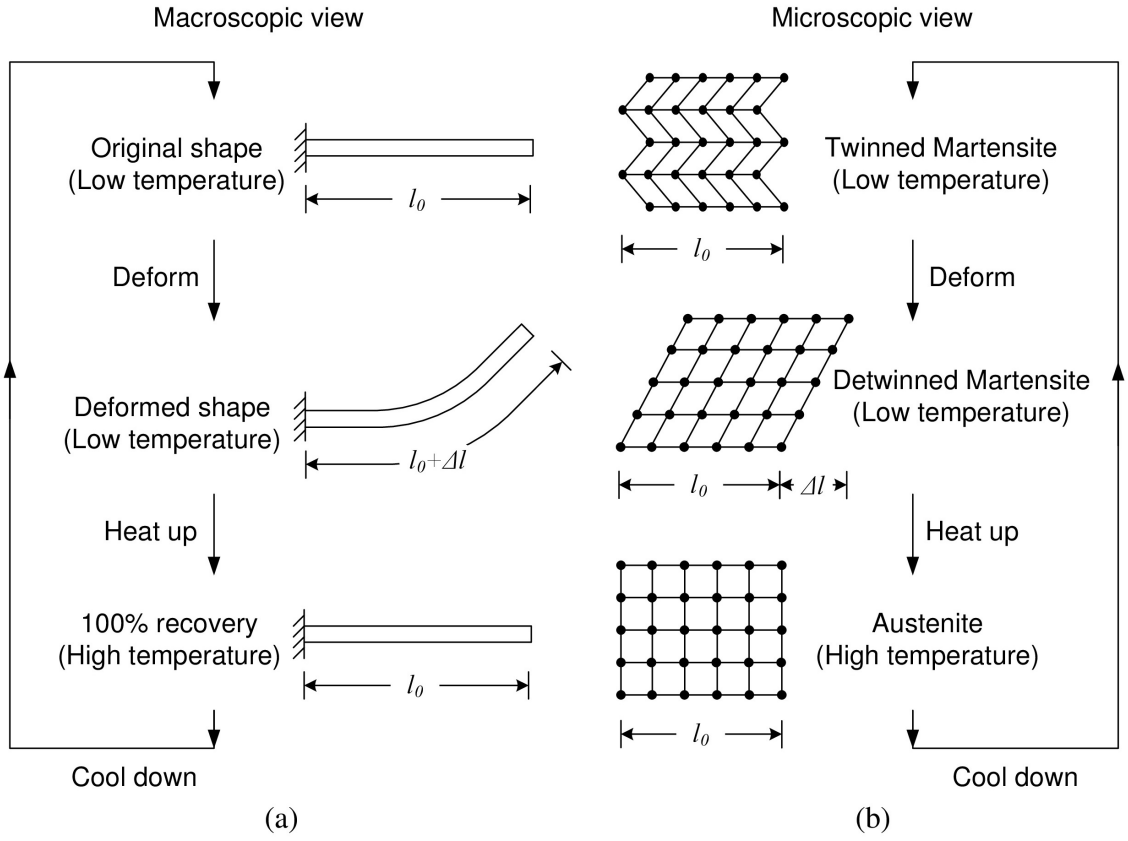

Figure 3.1: One-way shape memory effect: (a) Macroscopic view and (b) microscopic view.

At a microscopic level, the SME can be explained using the change in the lattice structure of a SMA as shown in figure 3.1(b). Let us consider that the material is initially at a low temperature (twinned martensite), and a section of the lattice has an initial

length of l_0. Assume an external stress is applied to the lattice at the same temperature and the deformation is only in the horizontal direction. The lattice is then deformed to the detwinned martensite phase by the stress and increases in length by an amount of $\triangle l$. The detwinning process is basically a rearrangement of atoms and a relatively small stress is required to detwin the martensite phase because bonds between the atoms are not broken in the process. It is important to note that the martensite phase has several possible arrangements of atoms but there is only one arrangement of atoms in the austenite phase. Upon heating, the martensite phase transforms to the austenite phase and the lattice changes to the only shape that the austenite phase has. Thus, it can be seen in figure 3.1(b) that the increased length, $\triangle l$, is recovered. When cooling, the material transforms from austenite phase to martensite phase which results in the formation of a twinned martensite phase. Note that the length of the new lattice is the same as the original length, l_0, since the distances between the atoms remain the same as in the austenite phase. Almost all physical properties of SMA such as Young's modulus, specific heat and resistivity are different between the martensite and austenite phases. These differences are caused by the lattice structure of the material. For example, the Young's modulus of the austenite phase is much higher than that of the martensite phase because the austenite phase is associated with a body-centered cubic crystal structure whereas the martensite phase is linked with face-centered cubic crystal structure. In general, the lattice structure of the martensite phase is more disordered and exhibits less symmetry than that of the austenite phase.

The stress-strain behavior of SMA undergoing the one-way shape memory effect is shown schematically in figure 3.2. In the figure, the SMA is originally at a low tempera-

ture and in the martensite phase. When stresses, which are smaller than the critical stress, σ_s^{cr}, are applied, the SMA initially deforms elastically (a→b). When the applied stress goes over the critical stress, a large stressed-induced strain occurs suddenly (b→c). This is the detwinning process of the SMA. At the point that the stressed-induced martensitic transformation has been completed (point c), the detwinned martensite phase dominates. During unloading, the elastic deformation recovers (c→d) and the material remains deformed with a residual strain, ε_r), caused by the detwinning of the SMA. If the SMA is then heated above the transformation temperature, the residual strain recovers (d→a) and the material returns to its original shape. At this point, the SMA is at the high temperature austenite phase. After cooling the SMA down below the transformation temperature, the SMA converts to the low temperature martensite phase while the shape remains the same as in the high temperature austenite phase. Note that if the stress exceeds the yield strength of the material, plastic deformation will occur and cause unrecoverable strain upon heating.

3.1.2 Transformation Temperatures

SME is caused by the phase transformations between martensite phase and austenite phase in SMA. These phase transformations are dependent on the stress applied to the SMA and the temperature in it and there are four important temperatures related to these phase transformations. They are martensite start temperature, M_s, martensite finish temperature, M_f, austenite start temperature, A_s, and austenite finish temperature, A_f. Figure 3.3 shows the definitions of these four transformation temperatures and how they are

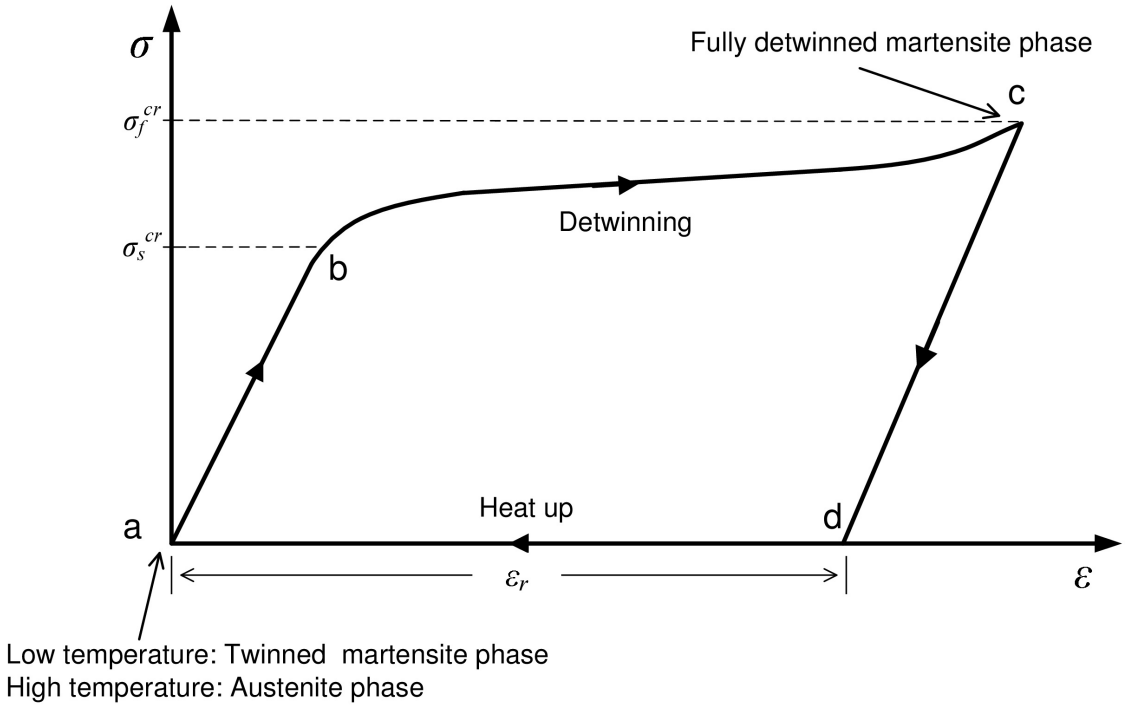

Figure 3.2: Stress-strain behavior of the one-way shape memory effect.

related to the phase transformation between martensite phase and austenite phase in SMA.

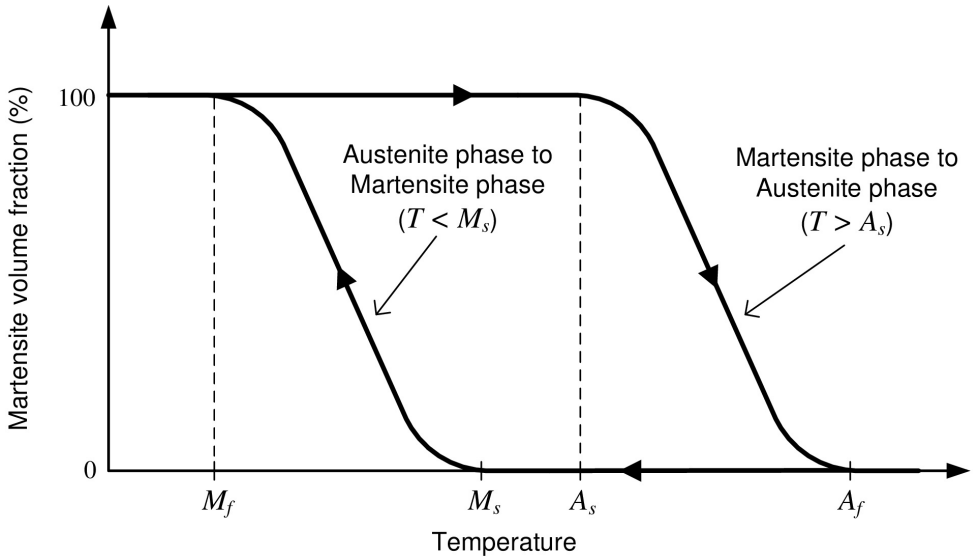

Figure 3.3: The relationship of the transformation temperatures and the phase transformations of SMAs.

In figure 3.3, the SMA is initially at a temperature lower than M_f and it is in 100%

martensite phase. When the SMA is heated up to a temperature above A_s, the martensite phase starts to transform to austenite phase. When the temperature in the SMA is higher than A_s but lower than A_f, the material is partly in the martensite phase and partly in the austenite phase. This combination of phases in the SMA can be characterized by the martensite volume fraction. The martensite volume fraction refers to the volumetric fraction of the material that is in the martensite phase. We will discuss the details of how the martensite volume fraction is related to these four transformation temperatures later in section 3.1.3. As the temperature goes above A_f, the SMA transforms completely to 100% austenite phase. If the SMA is then cooled down below a temperature that is lower than M_s, the austenite phase starts to transform to martensite phase. As the temperature cools below M_s, the transformation ends and the SMA is in 100% martensite phase. These four transformation temperatures can be determined experimentally and are generally a linear function of the stress applied to the SMA and the details of how to determine these four transformation temperatures from experiments will be discussed in section 3.2.

3.1.3 Constitutive Models

To effectively design actuators and other systems using SMA, it is necessary to understand the thermomechanical behavior of it. Many constitutive models of SMA have been developed in the past two decades and can be broadly classified into two categories: macroscopic phenomenological models and micromechanics-based models. From an engineering point of view, macroscopic phenomenological models are relatively practical because they fit the experimental data without attempting to capture the detailed underly-

ing thermomechanical behavior and avoid parameters that are difficult to measure, such as free energy. This section discusses three commonly used phenomenological constitutive models that have been proposed. In these models, only uniaxial loading is considered and quasistatic deformation is assumed, resulting in an isothermal condition. Typically, a strain rate below 5×10^{-4}/sec for a wire sample can be considered as a quasistatic deformation.

The thermomechanical behavior of SMA is quite different from that of conventional materials, and is a function of three primary variables: stress (σ), strain (ε), and temperature (T). The first phenomenological constitutive model of SMAs was proposed by Tanaka [72]. The author assumed that strain, temperature and the martensite volume fraction (ξ) are the only state variables, and the material constitutive relationship is:

$$d\sigma = \frac{\partial\sigma}{\partial\varepsilon}d\varepsilon + \frac{\partial\sigma}{\partial\xi}d\xi + \frac{\partial\sigma}{\partial T}dT \tag{3.1}$$

From equation 3.1, the constitutive equation can be written as a general expression

$$\sigma - \sigma_0 = E(\varepsilon - \varepsilon_0) + \Omega(\xi - \xi_0) + \Theta(T - T_0) \tag{3.2}$$

where E represents the Young's modulus of the SMA, Ω is the phase transformation coefficient and Θ is the thermal expansion coefficient of the SMA. The terms associated with subscript 0 refer to the initial state of the SMA. The above equation 3.2 shows that the stress consists of three parts: the mechanical stress, the stress due to phase transformation and the thermal expansion stress. Tanaka [72] presented an exponential expression to

describe the martensite volume fraction of SMAs as a function of stress and temperature. For transforming from martensite phase to austenite phase (heating transformation), ξ is given by:

$$\xi_{M\to A}(\sigma, T) = e^{a_A(A_s - T) + b_A\sigma} \tag{3.3}$$

For transforming from austenite phase to martensite phase (cooling transformation), ξ is given by:

$$\xi_{A\to M}(\sigma, T) = 1 - e^{a_M(M_s - T) + b_M\sigma} \tag{3.4}$$

where a_M, b_M, a_A and b_A are constants which can be determined experimentally. They are defines as:

$$\begin{aligned} a_M &= \frac{ln(0.01)}{M_s - M_f} & b_M &= \frac{a_M}{C_M} \\ a_A &= \frac{ln(0.01)}{A_s - A_f} & b_A &= \frac{a_A}{C_A} \end{aligned} \tag{3.5}$$

where C_M and C_A are the stress influence coefficients for the martensite phase and the austenite phase respectively. They represent the effect of stress on the transformation temperatures, and are frequently assumed to be constant as shown in figure 3.4.

Liang and Rogers [73] presented a model which was based on Tanaka's model. The difference between these two models is in the modeling of the martensite volume fraction. In the Liang and Rogers' model, ξ is modeled as a cosine function. For the heating transformation, ξ is defined as:

$$\xi_{M\to A} = \frac{\xi_0}{2}\{cos[a_A(T - A_s) + b_A] + 1\} \tag{3.6}$$

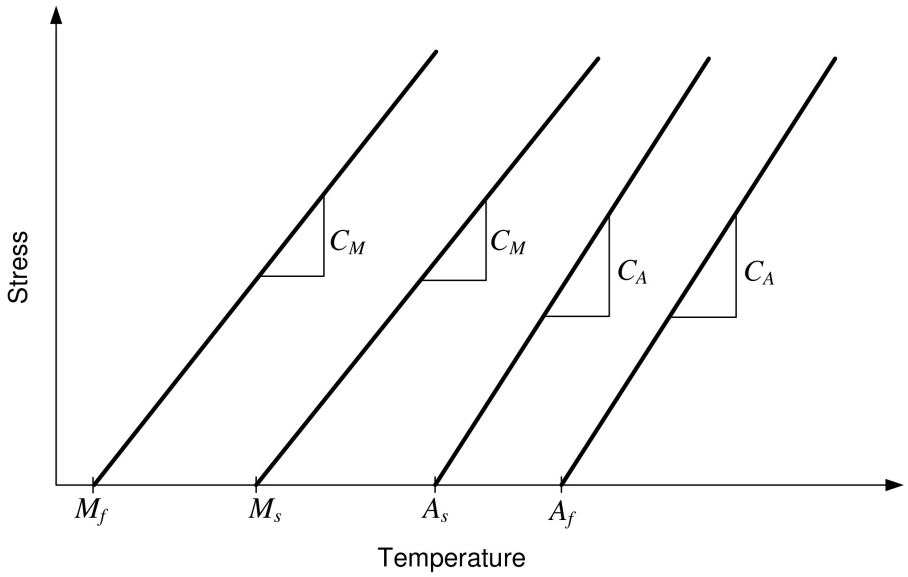

Figure 3.4: Definition of the stress influence coefficients for the martensite phase (C_M) and the austenite phase (C_A), which represent how the transformation temperatures change with stress in the Tanaka's and Liang and Rogers' models.

and for the cooling transformation, ξ is defined as:

$$\xi_{A\rightarrow M} = \frac{1-\xi_0}{2} cos[a_M(T - M_f) + b_M\sigma] + \frac{1+\xi_0}{2} \tag{3.7}$$

the constants, a_M, b_M, a_A and b_A are determined experimentally and given by:

$$\begin{aligned} a_M &= \frac{\pi}{M_s - M_f} & \qquad b_M &= -\frac{a_M}{C_M} \\ a_A &= \frac{\pi}{A_s - A_f} & \qquad b_A &= -\frac{a_A}{C_A} \end{aligned} \tag{3.8}$$

The major limitation of Tanaka's and Liang and Rogers' models is that they do not capture the stress-induced detwinning of the martensite phase. This means that these models cannot describe the detwinning process of the martensite phase in the SMA. Brinson [74] divided martensite volume fraction into two parts, namely stress-induced (ξ_s)

and temperature-induced (ξ_T) components, where

$$\xi_s + \xi_t = 1 \tag{3.9}$$

Based on the definition, the author modified tanaka's model according, resulting in a new constitutive equation shown as:

$$\sigma - \sigma_0 = E(\varepsilon - \varepsilon_0) + \Omega_s(\xi_s - \xi_{s0}) + \Omega_T(\xi_T - \xi_{T0}) + \Theta(T - T_0) \tag{3.10}$$

It is important to note that the definitions of the transformation temperatures used in the Brinson's mode are slight different from those used in the Tanaka's and Liang and Rogers' models. The definition of A_s and A_f are the same in both models, however, the definitions of M_s and M_f are different. In the Tanaka's and Liang and Rogers' models, the transformation temperatures are defined at zero stress and proportional to the stress applied to the SMA, as shown in figure 3.4. In the Brinson's model, the author assumed the M_s and M_f do not change if the applied stress is smaller than the critical stress. Therefore, the definitions of M_s and M_f in the Brinson's model are shown in figure 3.5. In chapter 4, since only heating transformations of SMA are considered, the difference between Tanaka's model and Brinson's model can be ignored. Therefore, we use Tanaka's model in the chapter for simplicity. We then use Liang and Rogers' and Brinson's models in chapter 5 for a more precise modeling.

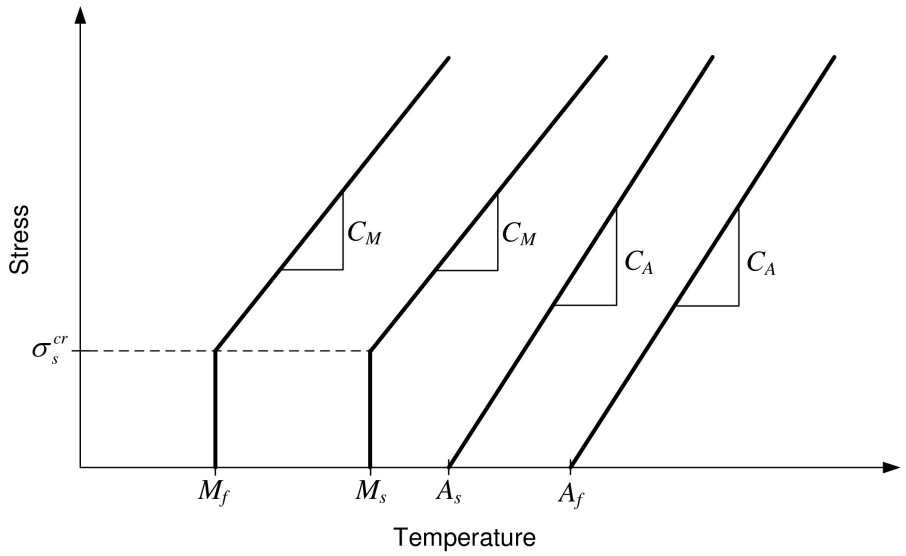

Figure 3.5: Definition of the stress influence coefficients for the martensite phase (C_M) and the austenite phase (C_A), which represent how the transformation temperatures change with stress in the Brinson's model.

3.1.4 Control Strategies

The approaches of controlling SMA can generally be divided into two categories, namely: direct feedback control and indirect feedback control. Direct feedback control uses direct measurements, such as position and force, as feedback to control the recovery strain of SMA, while indirect feedback control uses indirect measurements, such as temperature and resistance, and theoretical models to compute the recovery strain of SMA.

For direct feedback control, Teh *et al.* [75] presented a control system consisted of a differential-mode controller, an anti-slack mechanism, a rapid-heating mechanism and an anti-overload mechanism to fast, accurately control the output forces of an antagonistic pair of SMA wires. Two load cells and a rotary encoder were used to measure the output forces and positions of the SMA wires, and the measured data was used as direct feedback to control the SMA wires. The closed-loop response is fast and accurate even in the

presence of large external motion disturbances. Song *et al.* [76] designed a controller to control the tip position of a composite beam with embedded SMA wire actuators. The SMA wire actuators are embedded in a soft polymer sheet and then the sheet was attached to a honeycomb core to build a composite beam. The composite beam can be deformed by supplying direct current ranging to the SMA wires, and the tip of beam can move up to 15 mm. The feedback of the controller was from an infrared laser range sensor which measures the tip displacement of the beam. The measurements were sent to a real-time control implemented using a dSPACE data acquisition system and the control command from the controller was sent to a programmable power supply to actuate the SMA wire actuators. The experimental results demonstrated that the controller and the SMA actuators can be used to control the tip position of the composite beam precisely.

For indirect feedback control, Ikuta [60, 64] proposed a control scheme which combined electrical resistance feedback and position feedback to control the stiffness of the SMA actuators and indirectly control the output force using electrical resistance feedback. Bidaud *et al.* [77] presented a temperature feedback controller to remotely steer a SMA-actuated endoscope by a joystick. The simplicity of the controller permits to integrate it in a micro-systems. The research demonstrated that temperature feedback control was difficult because precisely measurement of the disturbed temperature of the SMA actuator in an open environment is challenging. Ma *et al.* [78] developed an electrical resistance feedback control system for a spring-biased SMA wire actuator. A Proportional-Derivative (PD) position control system was designed and experimentally tested to illustrate that electrical resistance feedback control was a feasible alternative to control SMA actuators for some applications. Bundhoo *et al.* [79] used commercially available

polymeric thick-film force sensitive resistors to control the contact force of biomimetic artificial fingers.

Pulse-Width Modulation (PWM) has been shown to be the most effective method in regards to control the temperature of SMAs. Ma *et al.* [80] implemented a PWM control scheme using MATLAB/Simulink and dSPACE data acquisition system. It was shown that the SMA actuator consumed 30% less energy than the continuous PD controllers while maintaining the same accuracy. Sugiyama *et al.* [81] applied open-loop PWM control to a soft robot that was capable of crawling and jumping. A periodic voltage pattern is applied to eight SMA coils during crawling. Price *et al.* [82] used AVR 8-bit RISC microprocessor which had three available PWM channels and power MOSFET drivers to synchronously control two MOSFET transistors, which in turn drove the SMA wires. Bundhoo and colleagues [79, 83] used a microcontroller-based PWM-PD feedback controller and a minimum jerk trajectory feedforward controller to control the finger in emulating natural joint motions.

MINIR is required to be operated in a MRI environment, however, commonly use position and force sensors are either not MRI-compatible or too big to fit in MINIR. Therefore, we decided to rely on image feedback to control the motion of MINIR since it is MRI compatible and the MR images of MINIR are clear which enables us to use MR images as feedback to control the motion of MINIR. However, the tracking algorithm for image feedback control may fail in some situations due to image noise or loss of tracking features. A backup control scheme is required. Temperature monitoring is required for antagonistic SMA actuators to prevent overheating and the temperatures in SMA actuators can be measured by thermocouples. In addition, MRI-compatible thermocouples (Type-

E) are commercially available [84]. Therefore, we proposed to use temperature feedback control as the backup control scheme for MINIR.

3.2 Characterization of Shape Memory Alloys

We have proposed to use temperature feedback control as a backup control scheme to control the recovery strain of SMA and discussed the relations of the strain in SMA and the temperature in it in the previous section. In this section, we discuss the important material parameters that are required for controlling the SMA using temperature feedback and how to determine those parameters experimentally. We also introduce the experimental setup that we designed for the experiments.

3.2.1 Important Parameters of SMA

For a specific SMA material, the phase transformation coefficient in equation 3.2 can be correlated with its Young's modulus. Let a SMA initially be stress free, strain free and in 100% austenite phase, *i.e.*, $\sigma_0 = 0$, $\epsilon_0 = 0$, $\xi_0 = 0$. Cool it down to a completely martensite phase and stretch it to the maximum recoverable strain, *i.e.*, $\sigma = 0$, $\xi = 1$, $\epsilon = \epsilon_L$. The thermal expansion stress is small compared to the mechanical stress and phase transformation stress in equation 3.2 and thus negligible. Thus, equation 3.2 becomes:

$$\Omega = -\varepsilon_L E \tag{3.11}$$

The above equation 3.11 shows that the phase transformation coefficient is a function of the Young's modulus of SMA since the maximum recoverable strain is a constant for a specific material. The Young's modulus of SMA is a function of the martensite volume fraction and can be considered as a combination of both the martensite phase and the austenite phase [72], which results in the expression:

$$E(\xi) = E_A + \xi(E_M - E_A) \tag{3.12}$$

where E_A and E_M are Young's moduli of the austenite phase and the martensite phase respectively. The ratio of E_A to E_M is generally larger than two, which enables us to use the antagonistic setup of SMA actuators [see figure 2.1(c) and figure 2.2(b)]. By substituting equation 3.11 and equation 3.12 into equation 3.2, the constitutive equation can be written as:

$$\sigma - \sigma_0 = (\varepsilon - \varepsilon_0 - \varepsilon_L\xi + \varepsilon_L\xi_0)[E_A + \xi(E_M - E_A)] \tag{3.13}$$

In this section, we used Tanaka's model that assumes an exponential expression of the martensite volume fraction, see equation 3.3 and equation 3.3. From equation 3.13, we can see that there are nine material parameters that are needed to be determined to fully define the constitutive model of a SMA. These parameters are M_s, M_f, A_s, A_f, E_M, E_A, C_A, C_M, and ε_L. Among these nine parameters, E_A and E_M are usually available from manufacturers. C_A, C_M, and ε_L are material constants that can be adapted from previous researches. The other parameters, M_s, M_f, A_s and A_f, are the transformation

temperatures which are highly dependent on the thermal and mechanical history of the SMA. Therefore, one of the focus in this section is to determine the transformation temperatures of the SMA. Since we only considered the heating transformation of the SMA in this research, we were especially interested in measuring A_s and A_f. After obtaining all required material parameters, Tanaka's model can be fully developed. In Tanaka's model, stress, strain and temperature are assumed to be the only variables in the model, see equation 3.13. Therefore, if stress is known, the strain will be a function of temperature. Since the strain in the SMA is related the temperature in it and the temperature in the SMA can be monitored using a thermocouple attached to it, we can control the strain in the SMA through temperature feedback based on equation 3.13.

3.2.2 Experimental Setup

The transformation temperatures in the constitutive models described in the previous section can be obtained from a series of experiments performed on SMAs using the experimental setup described in this section. Shaw and colleagues [85, 86] have published a series of papers to introduce uninitiated engineers to the characterization of SMA. They described special experimental techniques that help to illuminate and quantify the macroscopic thermo-mechanical behavior of SMAs. Although a lot of previous work has been done in the area of SMA characterization [85–88], the characterization procedures of SMA are not yet standardized, and material property tables are either not available or are provided incompletely. This is because SMA behavior is inherently nonlinear, hysteretic, and extremely temperature dependent. Since each SMA may be different, it is

necessary for us to develop our own experimental setup and procedures to obtain a satisfactory physics-based characterization of SMA. Moreover, most published research is based on uniaxial tensile tests, but bending, *i.e.*, to enable revolute joint motion, is the most important behavior which we are interested in characterizing, and hence, customized experimental setup and procedures are required.

To design the experimental setup, we followed the suggestions of ASTM F2082-06, Standard Test Method for Determination of Transformation Temperature of Nickel-Titanium Shape Memory Alloys by Bend and Free Recovery. This test method describes procedures for determining the martensite-to-austenite transformation temperatures of either fully-annealed or heat-treated nickel titanium alloys by measuring the deformation recovered during the thermal transformation. In other words, it is used to find the relation between recovery strain and temperature in the SMA. It can be extended to perform the stress-temperature relation of the SMA by adding a force sensor. For MINIR, we used antagonistic pairs of SMA wire to actuate the robot joints. Therefore, the experimental setup should be able two test two antagonistic SMA wires at the same time and have similar geometry with the robot. The design of the experimental setup is shown as figure 3.6. There are two columns on the main structure and the SMA wires can be pinched on them by screws. It is important to note that knot-tying and coiling of SMA wires will yield poor characterization results, therefore, fix the SMA wires by pinch or grasp are better choices. A rotary encoder is located on the top of the main structure and an extension place is attached to the shaft of the rotary encoder. There are two pins on the extension plate which are used for SMA wires to push against and hence rotate the rotary encoder. The rotation angle will then be measured by the rotary encoder. The rotary encoder can

count 2880 pulses per revolution which results in a 0.125° resolution. The device can not only be used to characterize single SMA wire and antagonistic SMA wires, but also capable of testing a single joint of the robot by attaching the joint to the device, as shown in figure 3.6. The detailed procedures and results of testing a single joint of the robot will be discussed later in section 4.5.1 and section 4.5.2.

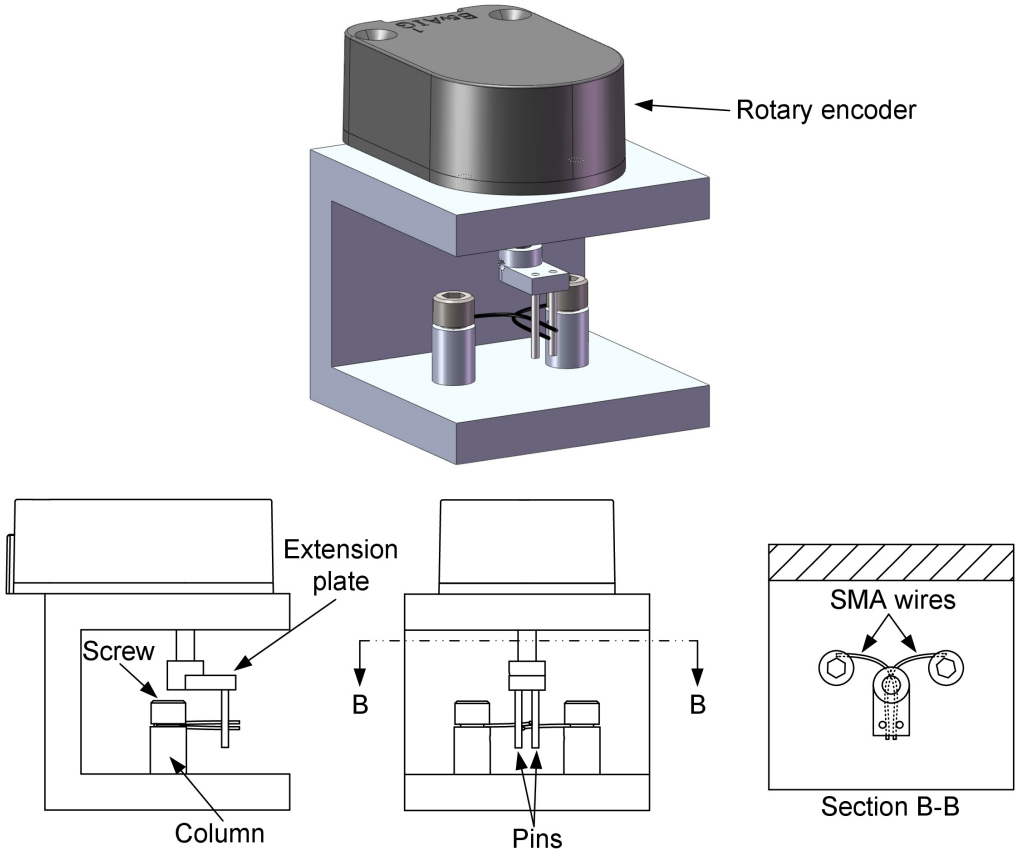

Figure 3.6: The design of the experimental setup for characterizing SMA wires in bending configurations.

For temperature sensing, we used T-type thermocouples which has 1°C accuracy. A thermocouple was attached to the middle of a SMA wire using a heat shrink tube with thermally conducive paste. The heat shrink tube was used to fix the thermocouple to the SMA wire to prevent it moves during testing. The thermally conductive paste was used

to ensure heat transfer while preventing current flowing through thermocouples because of its high thermal conductivity and high electric resistance. The temperature in the SMA wire will be recorded by a computer through a data acquisition system. The data acquisition system has a Sensoray model 626 PCI multifunction I/O card. The card has three 24-bit up/down counter pairs which can be configured for up to six incremental encoders, each having 24 bits of resolution. It also has sixteen 16-bit A/D converters which can be programmed for ± 5 V or ± 10 V maximum digital outputs, four 14-bit D/A converters with ± 10 V analog outputs and forty-eight DIO channels with 5 V digital outputs. The structure of the overall experimental setup is shown schematically in figure 3.7. The A/D converters were used to convert the analog voltage readings from thermocouples to digital inputs so that the computer can record it. The D/A and DIO channels were used to send control commands to control the temperatures in the SMA wire. For a 16-bit A/D converter, the ± 5 V output leads to a 0.076 mV output resolution. However, a 0.076 mV variation in voltage measurement is too small to precisely measured and it leads to about 1.8°C variation in the temperature estimation. As a result, the use of signal amplifiers was required for the system. We used Linear Technology LT1920 precision instrumentation amplifiers to implement the amplification circuit. Figure 3.8 shows the amplification circuit that we designed for a pair of antagonistic SMA wires.

3.2.3 Experimental Procedure

Because of the antagonistic actuation setup, we were only interested in characterizing the heating transformation of a SMA wire. Since the non-heated SMA wire will be naturally

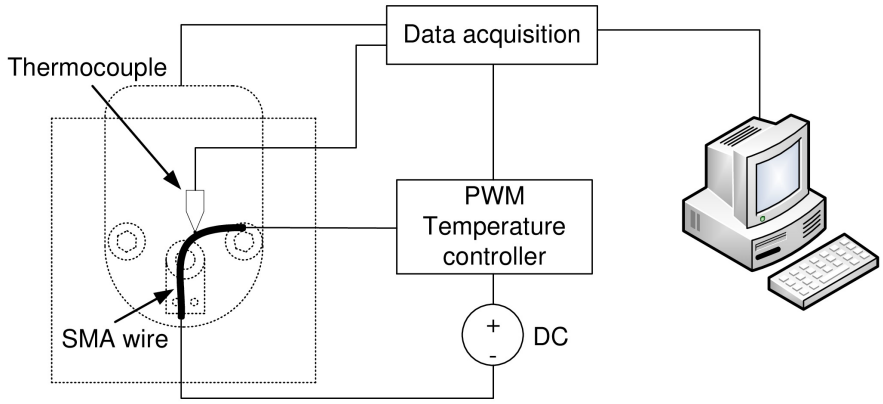

Figure 3.7: The hardware structure of the overall experimental setup.

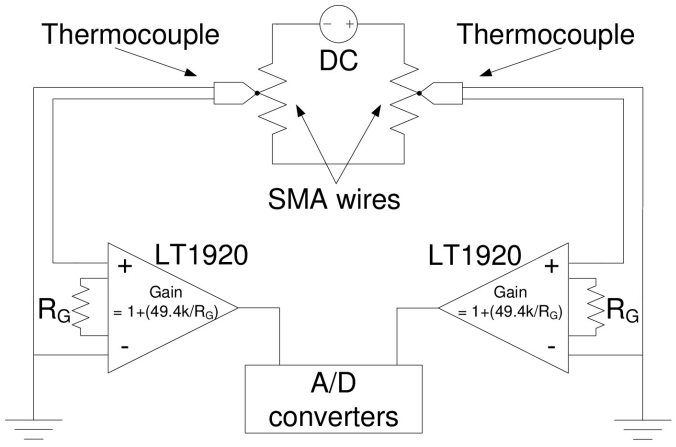

Figure 3.8: Amplification circuit for each pair of antagonistic SMA wires.

deformed by the heated wire towards the other direction, the hysteresis between heating transformation and cooling transformation of SME can be ignored. In section 3.2.1, we have seen that A_s and A_f are important parameters in the constitutive model and the accurate measurements of them were necessary for predicting the material behavior during the heating process. For the heating process, only A_s and A_f are required to be determined. Note that these transformation temperatures are often defined for the material in a stress-free condition, because they change as a function of applied stress. There are numerous ways to find A_s and A_f experimentally, but three methods are commonly used for Nitinol. They are Constant Load, Differential Scanning Calorimeter (DSC), and Active A_f.

We chose the Active A_f method to characterize SMA wires because the method involves bending characterization and the bending behavior of SMA wires is what we were interested in our application. This method, while not very sophisticated, yielded surprisingly accurate and repeatable results, and it required very little experimental apparatus. For the experiment procedures, we followed the suggestions of ASTM F2082-06 standard for measuring A_s and A_f.

We used resistive heating to actuate SMA wires. A constant current was applied across a SMA wire through a PWM temperature controller as shown in figure 3.6, causing the temperature in the SMA wire to increase by internal heating. Quasistatic conditions were achieved by allowing the temperature in the SMA wire to stabilize at the set temperature before recording the data to eliminate any dynamic effects. The experimental setup was put in a Styrofoam box to isolate it from outside disturbances when performing the experiments. The test specimen was a 25-mm-long SMA wire with a diameter of 0.5 mm, which is exactly the same as what we used in MINIR. Before starting the experiment, the SMA wire was heated to about 80°C and then cooled down to room temperature to ensure the SMA is in 100% martensite phase. The SMA wire was then placed in parallel with the back wall of the main structure and a screw was used to pinch one end of the SMA wire on the column. After fixing one end of the SMA wire, it was then carefully bent to an arc shape and the other end of it was placed in contact with one of the two pins on the extension plate. This end of the SMA wire was free to move during the experiment to prevent overconstrain as shown in figure 3.9(a). The maximum recoverable strain of the SMA wire is about 8%, therefore, the the radius of curvature of the bent SMA wire should not be smaller than 12.5 times the wire radius to prevent overstrain. For example,

in our test, the diameter of the SMA wire was 0.5 mm and the radius of curvature of the bent SMA wire in figure 3.9(a) was about 14 mm.

After placing the SMA wire on the experimental setup, we then started to characterize the SMA wire by heating it up. As the SMA wire is heated, it recovers to its original straight configuration and thus causes the extension plate to rotate along the rotary encoder as shown in figure 3.9(b). The rotation of the extension plate will then be measured by the encoder and the corresponding temperature will also be recorded. From this experiment, we can obtain the bending displacement vs. temperature relationship of the SMA wire and the transformation temperatures can be determined from the experimental results.

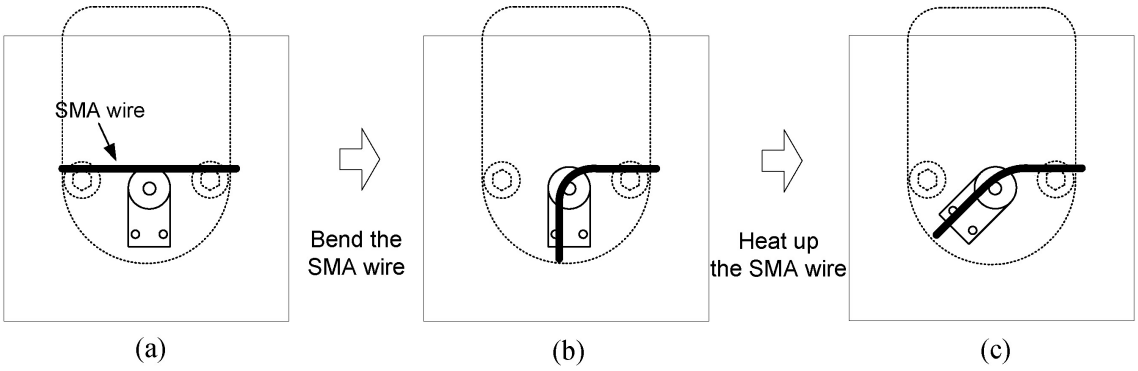

Figure 3.9: Schematic of the experimental procedures of characterizing the transformation temperatures of a SMA wire.

3.2.4 Experimental Results

The parameters to be measured in this experiment were the transformation temperatures, *i.e.*, A_s and A_f, of a SMA wire under zero stress. The connections of the SMA wire were show in figure 3.10(a). Both ends of the SMA wire were connected to electric wires. The connections were covered using heat shrink tubes which provide electric isolations. The

thermocouple was attached to the middle of the SMA wire and a heat shrink tube was used to fix the thermocouple. The SMA wire was then placed on the testing device as described in the previous section 3.2.3 and is shown in figure 3.10(b). The SMA wire was initially bent to an arc shape at 27°C. A constant current was applied across the SMA wire through a PWM temperature controller. The applied current heated the SMA wire because of internal heating. As the temperature in the SMA wire increased beyond A_s, the SMA wire started to transform to an austenite phase and recover to its original straight configuration as shown in figure figure 3.10(b).

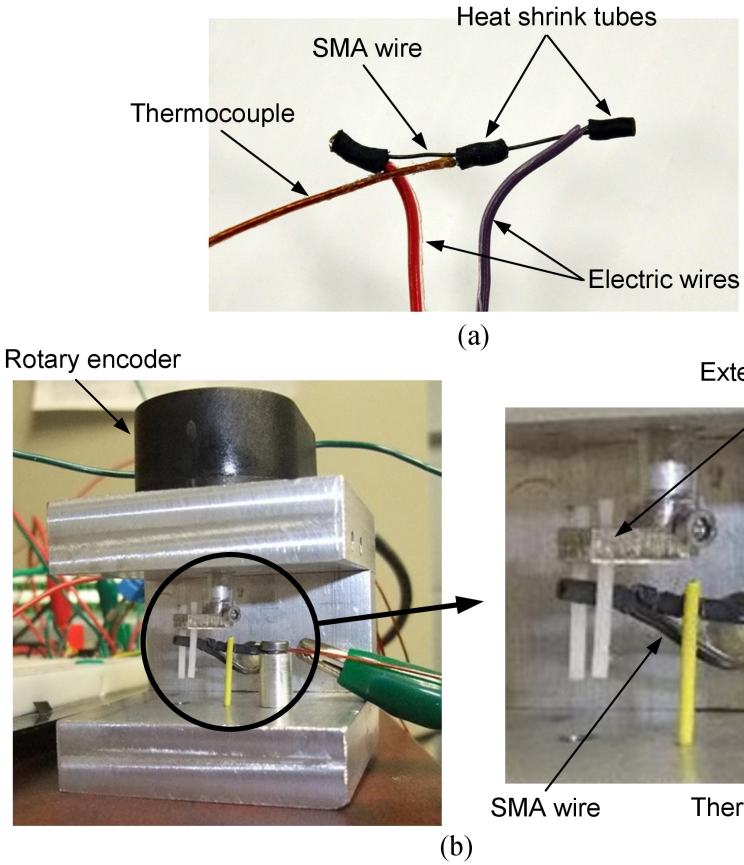

Figure 3.10: (a) Connections of the SMA wire and (b) experimental setup for characterizing the transformation temperatures of the SMA wire.

The experimental results are repeatable and shown in figure 3.11. Each data point in

Table 3.1: SMA wire parameters

Elastic moduli	Transformation temperatures	Strain	Transformation constant
E_A = 70 GPa E_M = 28.7 GPa	A_s = 30 °C A_f = 55 °C	ε_L = 0.067 ε_0 = 0.026	C_A = 13.8 MPa/°C

the figure was the average of six trials. A_s and A_f can be determined from the figure and they are approximated to be 30°C and 55°C respectively. The solid line in the figure was the theoretical model computed using equation 3.2 with the material parameters listed in table 3.1. In the table, the elastic moduli were provided by the manufacturer, and the maximum recoverable strain and transformation constant were from [73]. Initial strain of the SMA wire was computed from the geometry of a link of MINIR and the transformation temperatures were obtained from the experiments discussed previously in this section. Experimental results fit the theoretical model well with a maximum difference of 4.8°. The A_s of the SMA wire we used in this experiment was lower than human body temperature. It seems improper for our neurosurgical application since the SMA wire can be actuated by body temperature. However, the transformation temperatures of SMA can be tuned through annealing/training procedures [19]. Typically, A_s ranges from 25°C to 75°C. Hence, in our future prototype for tissue experiments, we planned to have SMA wires with 40°C A_s and 55°C A_f to prevent them from actuating by body temperature or damaging healthy tissues. Furthermore, the robot will be shielded by a polymer skin, which will act as an insulator.

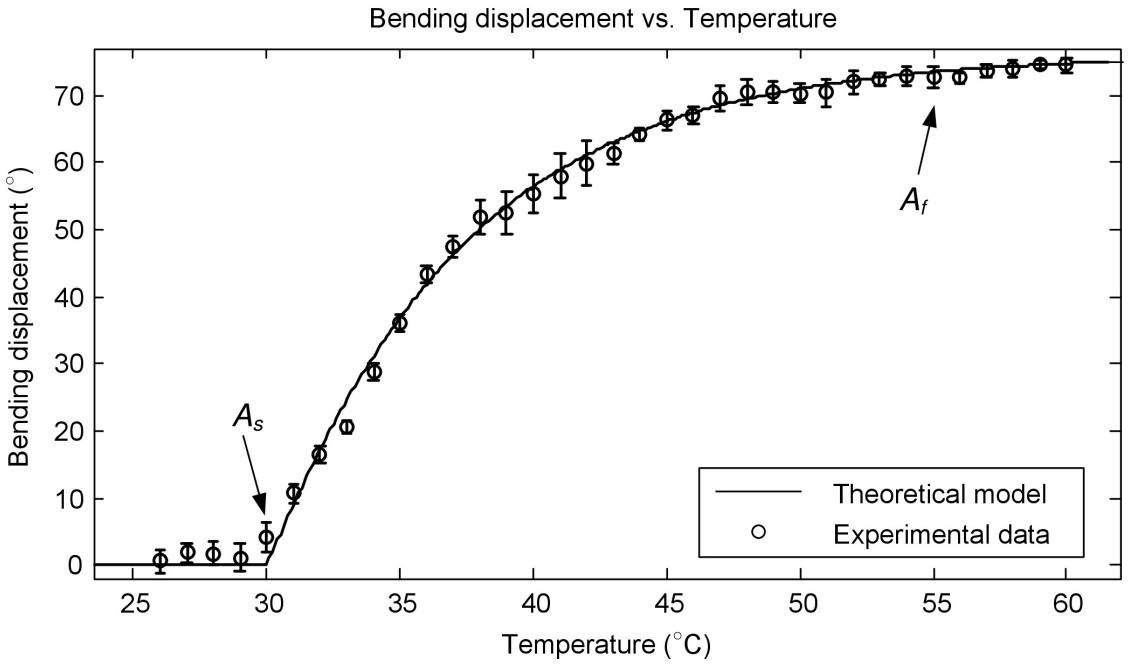

Figure 3.11: Bending displacement vs. temperature curve of a SMA wire.

3.3 Summary

In this chapter, we discussed the SME of SMA which occurs as a result of a transformation between martensite phase and austenite phases in the material. Phenomenological models have been developed to describe the phase transformation and the thermo-mechanical behavior of SMA. The analytical models assume the phase transformation depends on three primary variables: stress, strain and temperature in the material. The material parameters that are required for the models are determined experimentally. Therefore, we developed a customized experimental setup and systematic experimental procedures to determine important material parameters of SMA that are required for the analytical models. There are totally nine material parameters that are needed to be determined to fully define the models. The Young's moduli, E_M and E_A, were obtained from manufacturers. The transformation constant, C_A, and the maximum recoverable strain, ϵ_L, are material constants

that can be adapted from previous researches. Other material constants that are related to cooling transformation, *i.e.*, austenite phase to martensite phase, such as C_M, M_s and M_f are not required since we only considered the heating transformation of SMA, *i.e.*, martensite phase to austenite phase, in this research. As a results, the transformation temperatures, A_s and A_f, are what we are interested in measuring. We further presented the experimental results of the SMA wires that we used throughout this research and showed that the experimental results fitted the analytical models well.

The experimental procedures discussed in this chapter can be summarized as following steps:

1. Cut the SMA wire to 25 mm long

2. Make the connections on the SMA wire as shown in figure 3.10(a)

3. Heat the SMA wire to about 80°C and cool it down to room temperature to ensure the SMA is in 100% martensite phase

4. Placed the SMA wire in parallel with the back wall of the main structure and use a screw to pinch one end of the SMA wire on the column, as shown in figure 3.9(a)

5. Carefully bend the SMA wire to an arc shape and let the other end of it in contact with the corresponding pin on the extension plate, as shown in figure 3.9(b). Note that the radius of curvature of the bent SMA wire should not be smaller than 12.5 times the wire radius to prevent overstrain

6. Heat the SMA wire slowly to a desired temperature, wait for the temperature to stabilize to ensure quasistatic conditions, and then record the encoder reading

7. Repeat the above step 6 until the SMA is fully recovered, *i.e.*, the encoder reading does not change even the temperature increases

8. Remove the free end of the SMA wire from the pin on the extension plate and then cool the SMA wire down to room temperature

9. Go to step 5 to repeat the experiment for another date set

Chapter 4

Development of the SMA Wire Actuated MINIR

In this chapter, we discuss the detailed design features of the second generation of MINIR in section 4.1 and present the antagonistic SMA wire actuation in section 4.2. Section 4.3 describes the correlation between the joint motion of a link of MINIR and the temperature in the SMA wire actuator as well as the force modeling of the SMA wire actuator. Section 4.4 describes the implementation of the PWM temperature controller, the control circuit and the image feedback control system. In section 4.5, we show the results of controlling the temperatures of multiple SMA wire actuators, and hence the joint motion, by using only one power supply. We also present the results of the block force test of a link of MINIR and demonstrate that MINIR was able to move in a gelatin medium, electrocauterized the gelatin and sucked the melted gelatin out. Furthermore, we show that the image feedback control could be used reliably to control the motion of MINIR. Moreover, we prove that MINIR was MRI-compatible by testing it in a 3-T MRI scanner and analyzing the MR images. Finally, in section 4.6, we make some concluding remarks. Most contents of this chapter are published in [89, 90].

4.1 Robot Design

The first prototype of MINIR was developed by Pappafotis *et al.* [91]. The robot consisted of six revolute joints and the entire robot was made from acetal resin engineering plastic,

known as Delrin®, which is completely MRI-compatible. The robot was 72 mm long, 8.8 mm in diameter and actuated by two SMA wires. During trials, the robot motion was repeatable and it could generate 12 mN to 50 mN of force at the end-effector, depending on the robot configurations. The actuation time from the start to finish was about 2.5 seconds and the motion of the robot is shown in figure 4.1. The MR images of the various components of the robot showed that the robot was MRI-compatible and no significant image artifact was observed.

Although the prototype showed some desired functions of MINIR, there are some significant improvements that has to be added. First, individual actuation of the joints is required so that each joint can be controlled independently. The output force of the end-effector is small and thus the usage of lager-diameter SMA wire actuators has to be investigated. Moreover, feedback control system has to be implemented to control the motion of the robot. Additionally, electrocautery and suction systems used to remove tumors need to be implemented.

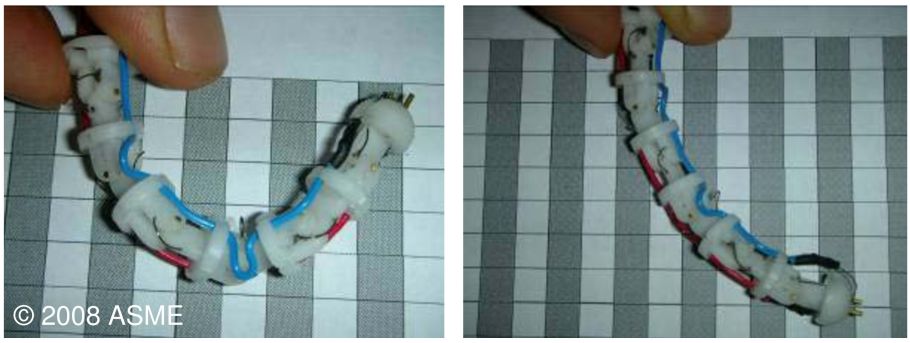

(a) (b)

Figure 4.1: Motion of the first prototype of MINIR: (a) Initial position and (b) fully-actuated position

To overcome the limitations of the first prototype of MINIR, we designed a second generation MINIR as shown in figure 4.2. The robot consisted of four major components:

they are tip link [figure 4.2(b)], base link [figure 4.2(c)], short link [figure 4.2(d)] and long link [figure 4.2(e)]. The detailed engineering drawings of each part of the robot can be found in appendix A.1. The larger holes on the short link and long link were drilled to allow the passage of the SMA wire actuators, and the remaining two small holes were for two columns to go through. These two columns were used for SMA wire actuators to push against during phase transformation and transmit the necessary actuation force to the link resulting in joint motion. Two additional holes have also been drilled in the base link for fastening to a fixed frame. Each joint of the robot was actuated by two 0.5 mm diameter SMA wire actuators. The two probes shown in the figure were the electrocautery tips for electrocauterizing brain tumors. The two tubes routing through the robot were the suction and irrigation tubes used to remove liquid, blood and electrocauterized debris in the brain. In this prototype of MINIR, all revolute joints were on the outside of the

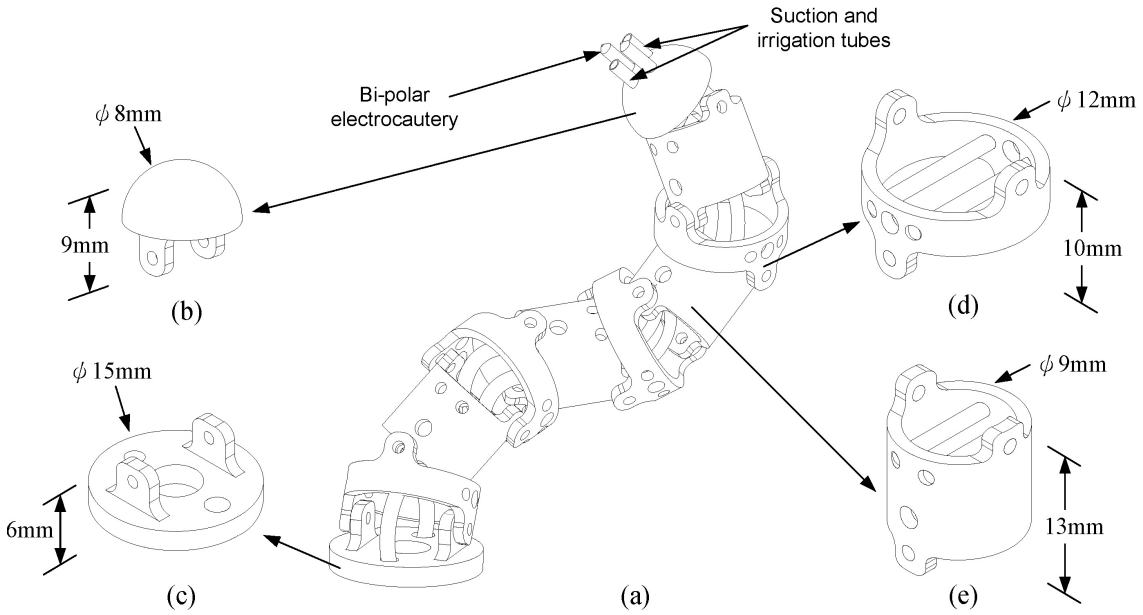

Figure 4.2: (a) The schematic of the second generation of MINIR, (b) tip link, (c) base link, (d) short link and (e) long link.

robot body which keeps the robot center hollow. The hollow center of MINIR allows the passage of electrical wiring that could be used to actuate individual SMA wire actuators, to transfer signals of sensors, as well as for the electrocautery wires, suction and irrigation tubes to reach the tip link of the robot. This design made the robot compact and easy to shield. The hollow cross-section area of the long link was 50.27 mm^2, and the total cross-section area of the two columns and two SMA wires was 17.01 mm^2. There is still 33.26 mm^2 (66%) left for wires and tubes to be routed through.

4.2 Actuation Design

We proposed to use a pair of antagonistic SMA wires to actuate each joint of MINIR and the actuation mechanism is shown in figure 4.3. Each SMA wire actuator was bent to an arc shape and one end of it was fixed to a link of MINIR while the other end was free and in contact with a column. In the neutral position [see figure 4.3(b)], both SMA wire actuators are bent to keep the link straight. Since the maximum recoverable strain of the SMA wire is about 8% [70], it implies that the pre-strain of the SMA wire actuators should not be over 4% in the neutral position to prevent over-strain. When actuating the left side of the SMA wire actuator, for example, it is heated by electric current and thus recovers to its original memorized straight shape. As a result, the long link is pushed by the SMA wire actuator and causes a clockwise rotation as shown in figure 4.3(c). Two antagonistic SMA wire actuators are used for each joint, so that each joint can be moved back and forth and controlled independently. This new design feature, with respect to the first generation of MINIR, not only gives the MINIR independent joint actuation

capability but also increases the range of joint motion as well as output force.

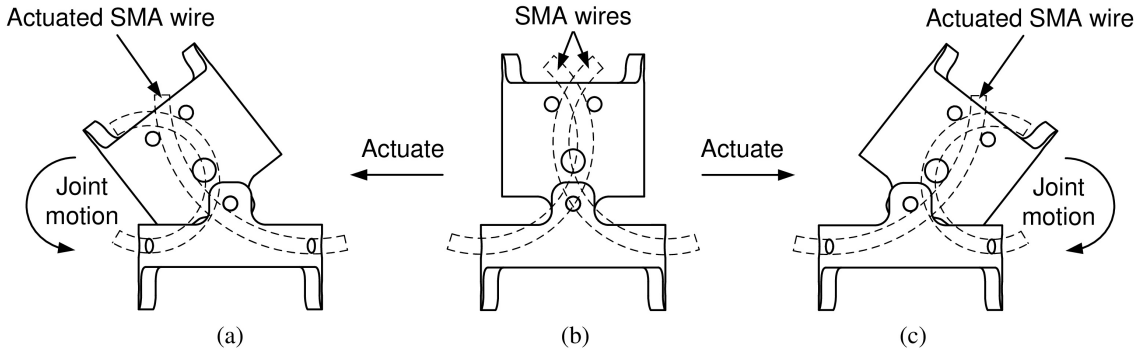

Figure 4.3: The actuation mechanism of the second generation of MINIR: (a) The SMA wire on the right side is actuated (b) neutral position and (c) the SMA wire on the left side is actuated.

The second generation of MINIR has a total of nine revolute joints and the motion range of each joint is $\pm 30^{\circ}$ due to the geometric limitation. The workspace of MINIR is shown as figure 4.4, and the motion range of the tip is 120 mm along x and y axes, and 80 mm along the z-axis. The origin (0, 0, 0) in figure 4.4 is the center of the base link of the robot.

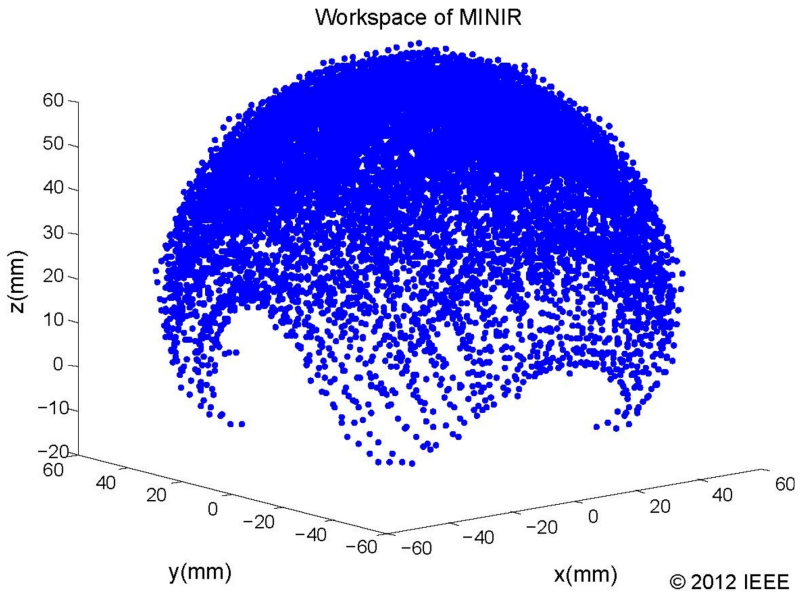

Figure 4.4: Workspace of the second generation of MINIR.

4.3 Modeling of SMA Wire Actuators

Due to the space constraint in the robot and the strong magnetic working environment of a MRI scanner, commonly used position sensors such as encoders, LVDT and strain gauges are not feasible for MINIR. In this research, we proposed to use temperature feedback and image feedback to control the motion of MINIR. To precisely control the motion of the robot using temperature feedback, it is important to model the thermo-mechanical behavior of the SMA wire actuators and use the parameters in the model to predict and control the motion of the actuators.

4.3.1 Correlating Joint Motion with Temperature

To control the motion of MINIR using temperature feedback, an analytical relationship between joint motion and the temperature in the SMA wire actuator is necessary. To derive the analytical model, we assumed that the SMA wire actuator is bent to a circular arc and fixed to a link of MINIR as shown in figure 4.5(a). We can see in the figure that the setup of the SMA wire actuator is exactly the same as we characterized the SMA wire in section 3.2 [see figure 3.7(b)]. Therefore, the same experimental setup will be used later in this chapter to test the performance of a joint of MINIR. According to figure 4.5(b), we have the correlation between strain, ε, and radius of curvature, r, of the SMA wire actuator, which is given by:

$$\begin{cases} \varepsilon = \frac{r - r_0}{r_0} \\ r_0 = r - \frac{d}{2} \end{cases} \Rightarrow r = \frac{d}{2\varepsilon}(1 + \varepsilon) \tag{4.1}$$

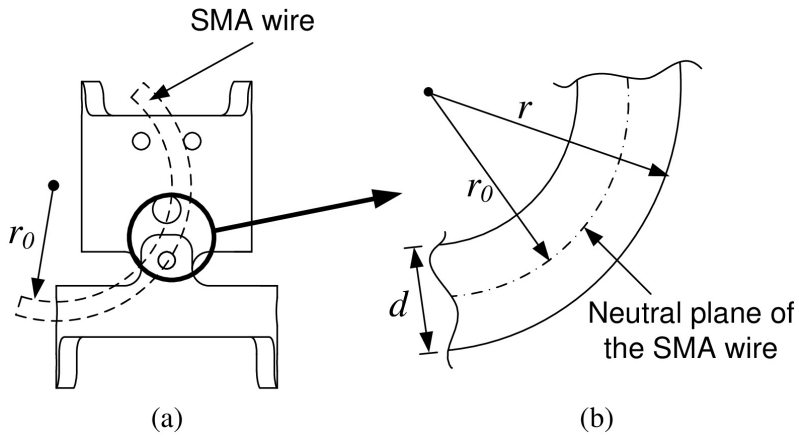

Figure 4.5: (a) A SMA wire actuator is attached to a link of MINIR and (b) correlation of strain to radius of curvature of the SMA wire actuator.

Since the diameter, d, of the SMA wire actuator is known and the strain in the SMA wire can be derived from equation 3.13 if the temperature in it is known and the external load remains constant ($\sigma - \sigma_0 = 0$), the radius of curvature of the SMA wire actuator can be computed using equation 4.1. A straightforward calculation using equation 4.1 shows that the radius of curvature of the SMA wire actuator should not be less than 12.5 times the wire radius for 8% maximum recoverable strain.

The next step is to derive the relationship between the radius of curvature of the SMA wire actuator and the joint motion, θ, of each joint. From the geometry of a link of MINIR as shown in figure 4.6, the following relationship is satisfied:

$$(Lsin\theta + x)^2 + (Lcos\theta + y - r)^2 = r^2 \tag{4.2}$$

Therefore, the joint motion of each joint can be derived from the radius of curvature of the SMA wire actuator using equation 4.2. Since the geometry of each link is also known, we can derive the coordinates of the joints for successive links by knowing the position

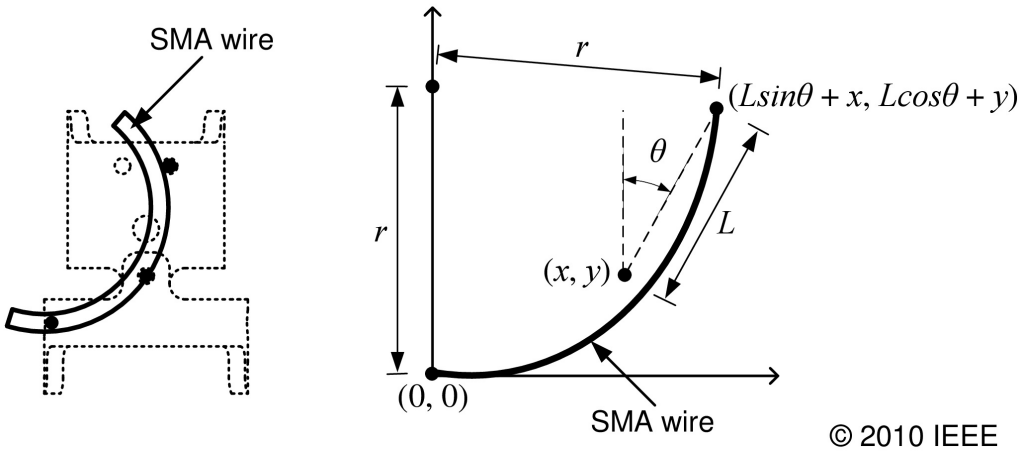

Figure 4.6: The geometry of a link of MINIR used to derive the relationship between the radius of curvature of the SMA wire actuator and the joint motion of the joint.

of each joint.

To summarize, we can measure the temperatures of the SMA wire actuators by the thermocouples attached to them and then use equation 3.13 to compute the strain in each SMA wire actuator. After obtaining the strain, we can use equation 4.1 to derive the radius of curvature of the SMA wire actuator and then compute the joint motion by using equation 4.2. We can compute the joint motion of each joint of MINIR by measuring the temperatures in the SMA wire actuators, and therefore the tip position of MINIR can be computed by forward kinematics. The simulation results of the joint motion at different temperatures are shown in figure 4.7. Essentially, this approach enables us to control the tip position of MINIR by monitoring the temperature of each SMA wire actuator through the thermocouple attached to it.

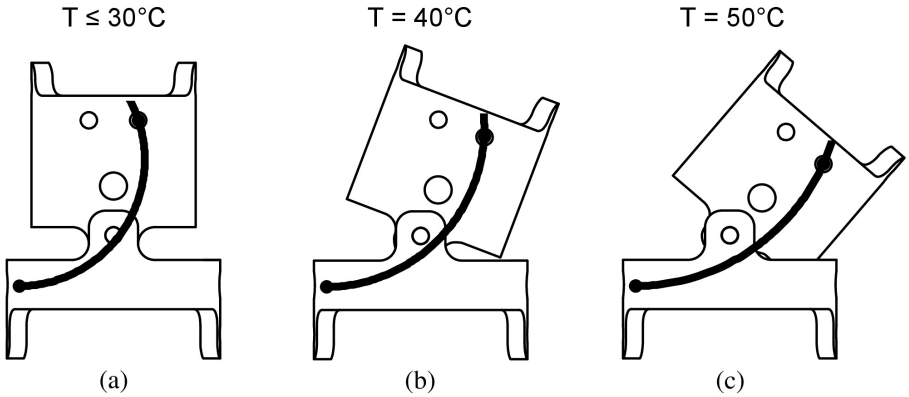

Figure 4.7: The simulation results of the joint motion and the shapes of the SMA wire actuator at different temperatures: (a) T $\leq$ 30 °C, (b) T = 40 °C and, (c) T = 50 °C.

4.3.2 Force Modeling of the SMA Wire Actuator

MINIR is required to be able to move in a tightly enclosed environment such as a human brain. Thus, we need to ensure that the force generated by a SMA wire actuator is sufficient. In our applications, it may not be necessary for the robot to exert a large force to move the tissue since electrocauterization of the tumor (through the electrocautery tips located on the tip link of MINIR as shown in figure 4.2) will enable removal of tissue. However, it is advantageous to be able to generate enough force at the end-effector through SMA actuation to push the tumor, if necessary, during electrocautery. To understand the force-temperature relationship of the SMA wire, we investigated the constrained recovery behavior of it. Constrained recovery means the strain in the SMA wire is kept constant and the testing involves measurements of force-temperature relationship under different strain conditions, *i.e.*, different positions of the joint. The space inside the robot is very limited, thus, the size of SMA wire actuators is extremely crucial. An analytical model that can be used to estimate the force capability of SMA wires can also be used as a guidance of sizing the SMA wire actuators.

In our design, the initial strain, ε_0, applied to each SMA wire actuator in MINIR is 2.5%, and the maximum recoverable strain, ε_L, of the SMA wire is about 8%. Since the initial strain is larger than the maximum recoverable strain, the initial strain can be fully recovered when the SMA wire actuator is actuated. As a result, the ε_L in equation 3.13 can be replaced by ε_0. Constrained recovery implies that the strain in the actuator is kept constant, therefore $\varepsilon - \varepsilon_0 = 0$. Moreover, considering the working environment of MINIR, the SMA wires are initially stress free and at room temperature, *i.e.*, $\sigma_0 = 0$ and $\xi_0 = 1$. Based on the above conditions, equation 3.13 can be re-written as:

$$\sigma = \varepsilon_0 E(\xi)(1 - \xi) \tag{4.3}$$

Equation 4.3 is only valid for uni-axial loading case because it is based on the tensile model of SMA. However, in the operation of MINIR, bending behavior is what we need to characterize. Thus, a new model that can describe the force-temperature behavior of the SMA wire actuator in bending configurations has to be developed.

In this derivation, only pure bending is taken into consideration, ignoring the effect of shear stresses and assuming that the neutral plane remains at the center of the cross-section of the SMA wire actuator. Considering that the SMA wire actuator is pre-strained to an arc shape and fixed to a link of MINIR as shown in figure 4.5(a), the strain distribution of the SMA wire can be defined as:

$$\varepsilon(y) = \frac{y}{r} \tag{4.4}$$

Where r is the radius of curvature and y is the distance from the neutral plane of the SMA wire. Since the SMA wire is at a pre-strained configuration, the strain at this state can be considered as the initial strain in the SMA wire, *i.e.*, $\varepsilon_0 = \varepsilon$. When the SMA wire actuator is heated, it intends to recover to its original straight configuration and thus tensile stresses are generated. The generated stresses then cause a bending moment, M, which can be expressed as a function of y and is given by:

$$M = \int_A \sigma(y)\, dA \tag{4.5}$$

To solve equation 4.5, the stress distribution, $\sigma(y)$, has to be solved, and equation 4.3 can be used to obtain the stress distribution. However, Tanaka's model assumes an exponential expression for the martensite volume fraction and is given as equation 3.3 for heating transformation. In the equation, we can see that the martensite volume fraction is dependent on the stress, *i.e.*, ξ is a function of σ, therefore the stress distribution has to be solved numerically.

Finite difference method are used to solve the stress distribution of the SMA wire in the bending configurations. We model the actuator to consist of i discrete layers along the y direction with t as the thickness of each layer and y_i as the distance from the neutral plane to layer i (see figure 4.8). Each layer is assumed to be under pure tensile stress and the neutral plane remains stress free. We assume that the thickness of each layer is small and all layers above the neutral plane are in tension. Therefore, the initial strain of each layer can be written as:

$$\varepsilon_i = \frac{y_i}{r} \tag{4.6}$$

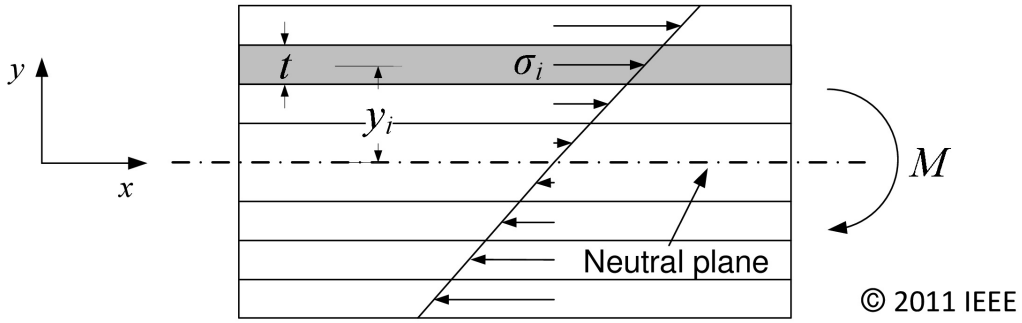

Figure 4.8: Decompose a SMA wire into layers.

The radius of curvature, r, in the above equation 4.3.2 can be derived from the geometry of a link of MINIR. After obtaining the initial strain in the SMA wire, the stress distribution can then be computed using Newton-Raphson's method to solve equation 4.3 iteratively after substituting the expression of the martensite volume fraction from equation 3.3. The Newton-Raphson's method used to solve stress distribution is expressed as:

$$\sigma_{new} = \sigma_{old} - \frac{f(\sigma_{old})}{f'(\sigma_{old})} \tag{4.7}$$

and the function $f(\sigma)$ and $f'(\sigma)$ are obtained from the following expressions:

$$\begin{aligned} f(\sigma) &= \sigma - \varepsilon_0 E(\xi)(1-\xi) \\ f'(\sigma) &= 1 - \varepsilon_0(E_M - E_A)b_A\xi + \varepsilon_0(E_M - E_A)b_A\xi^2 + \varepsilon_0 E(\xi)b_A\xi \end{aligned} \tag{4.8}$$

After obtaining the stress distribution, the generated moment of each joint can be computed by:

$$M = 2\sum_{i=0}^{n} \sigma_i y_i dA \tag{4.9}$$

Since the geometry of the link of MINIR is known, the moment arm, l, is known. There-

fore, the tip force of each link can then be obtained using:

$$F_{tip} = \frac{M}{l} \tag{4.10}$$

To summarize the force modeling of a bent SMA wire actuator, we first used the geometry of a link of MINIR to derive the distribution of the initial strain of the bent SMA wire actuator using in equation 4.6. We then used the constitutive model of SMA in equation 4.3 and Newton-Raphson's method in equation 4.7 to find out the generated stress distribution of the SMA wire actuator. Finally, we used the concept of finite difference to derive the generated moment given by equation 4.9 and thus the generated force at the tip of each link is given by equation 4.10.

The simulation results of a 0.5 mm diameter SMA wire actuator is shown in figure 4.9 and the parameters used here were experimentally determined in section 3.2 and as shown in table 3.1. The figure shows the simulated generated forces at the tip of each link of MINIR as a function of temperature for different pre-strains. By comparing the generated forces of different pre-strain, it is apparent that the generated forces in the motion range of MINIR (0° to 30°) are about the same. In other words, the generated force is relatively independent to the pre-strain in the SMA wire. This significant observation implies that each joint of MINIR is able to generate the same amount of force at different positions.

Based on the simulation results in this section, we can say that the 0.5 mm diameter SMA wire actuator can generate up to 1.5 N of force at the tip of each link of MINIR. In section 4.5.3, we show that the theoretical model matches the experimentally measured

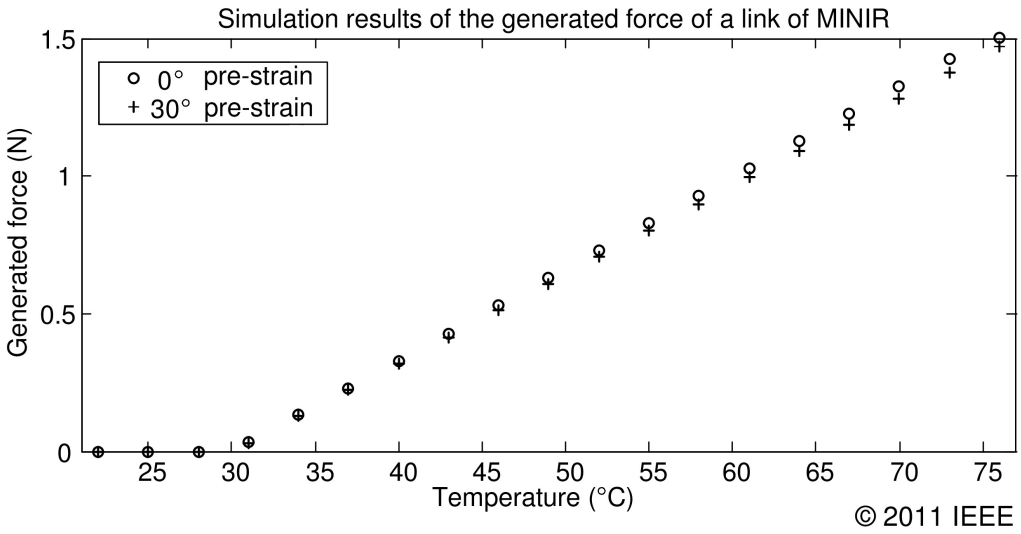

Figure 4.9: Simulation results of the generated force at the tip of a link of MINIR.

forces quite well. Later in the same section, we show that MINIR is able to move in a gelatin slab. Gelatin is commonly used in ballistic tests to simulate human muscle which is a lot stiffer than brain tissue. Hence, we hypothesize that if MINIR is able to move in the gelatin, then we do not anticipate any problem in moving it inside brain tissue.

4.4 Controller Design

We proposed two control strategies to control the motion of MINIR in this chapter. One is using temperatures in the SMA wire actuators as feedback signals to control the joint motion of MINIR through the model that we developed in section 4.3.1. The other one is the image feedback control. We proposed to use images to track specific features of the robot and use the positions of those features to compute the joint motion of MINIR. The feedback images can be obtained from a MRI scanner directly. At this point, however, we used a camera to get the images of MINIR since we could not obtained MR images from the MRI scanner directly. The frame rate, color depth and resolution of the camera were

adjusted to ensure the image quality that we get from the camera is closely to the image quality that we get from a MRI scanner. Temperature feedback control serves as a backup control scheme in case the image tracking algorithm fails due to loss of image or noise in the image.

The proposed control flow chart of the overall system of MINIR is shown in figure 4.10. The controller acquires image from the camera continuously and user can manually select the tracking features of the robot in the image. After selecting checking points, the user can then send control command to move the robot. Upon receiving the control command from the user, a logic algorithm will decide whether the tracking of the selected points is satisfactory or not. If the image tracking of the selected points is satisfactory, the system will control the robot motion based on image feedback. If, however, the answer is no, the user can choose to select alternatives tracking points or control the robot using temperature feedback. The system will then determine if the robot reaches desired position or not no mater temperature feedback or image feedback is used. If the desired position has been reached, the user can decide to stop the procedure or send another control command.

4.4.1 Temperature Feedback Controller

The joint motion of MINIR can be reliably computed by the temperature in the SMA wire actuators using the model that we developed in section 4.3.1. Therefore, we can control the joint motion using temperature feedback. To control the temperatures in the SMA wire actuators, a temperature controller is required. PWM is a powerful technique

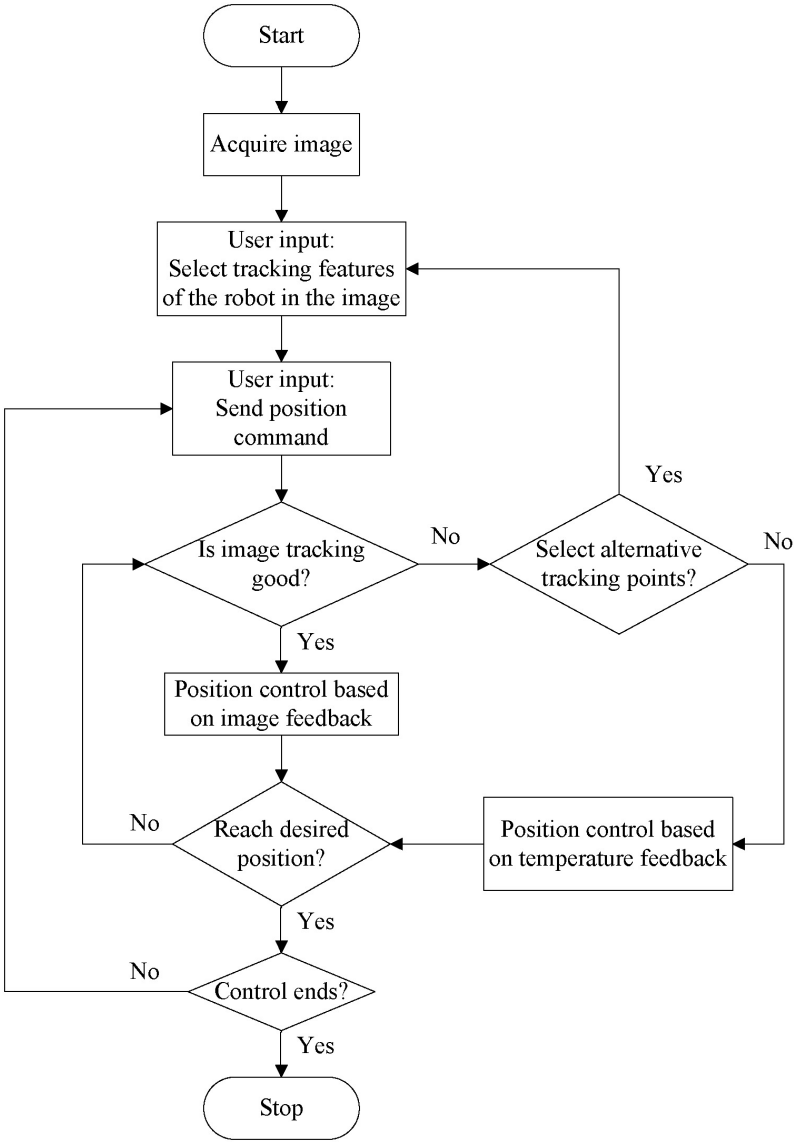

Figure 4.10: The proposed control flow chart of the overall system of MINIR

to control analog circuits using digital signals and therefore makes the system robust to disturbance. There are a variety of ways to realize PWM and we chose using software to generate PWM signal in our research. We also used multiplexed control to control multiple SMA wires by using only one power supply. The circuit that we developed to control the temperatures in four SMA wires is shown schematically in figure 4.11. The circuit is comprised of four switches, four SMA wire actuators, and a DC power supply. In the

figure, four SMA wire actuators were used as an example to explain how the circuit works and the circuit can be extended to control more SMA wire actuators if necessary. Note that only one power supply is required to control multiple SMA wire actuators using this circuit. A DC power supply is used to provide a constant current to SMA wire actuators and the multiplexed control is used to select which actuator should be controlled. The PWM control signal is used to control the state of the switches and it thus converts the continuously supplied current into an equivalent PWM output command which activates the corresponding SMA wire actuator and thereby induces joint motion. By switching current between multiple SMA wire actuators at a high frequency, 20 Hz in this case, multiple SMA wire actuators can be heated or maintained at desired temperatures by using one power supply.

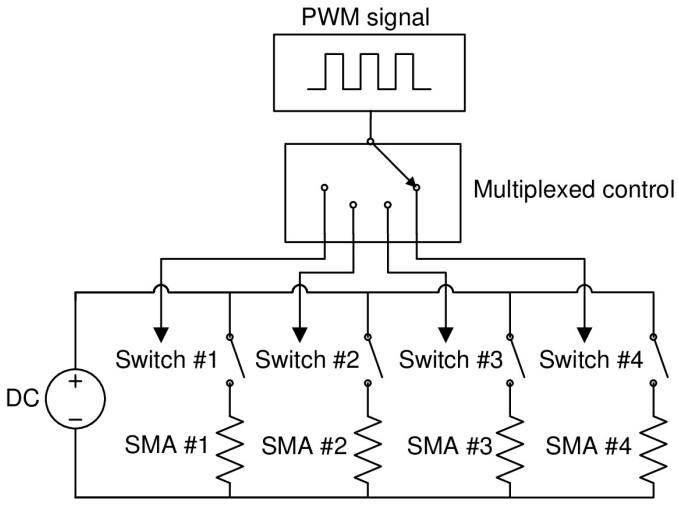

Figure 4.11: The control circuit used to control the temperatures in the SMA wire actuators.

To control the joint motion of MINIR using temperature feedback, the control command of each joint is first mapped to a temperature command, T_s, by the steps described in section 4.3.1. The measured temperature, T_m, of each SMA wire actuator is monitored

by a thermocouple attached to it. If the difference between T_s and T_m of a SMA wire actuator is larger than a threshold, δ, the heating time, t, will be computed by equation 4.11. The proportional gain, k, can be adjusted to change the system response.

$$t = k(T_s - T_m) \tag{4.11}$$

This control command, t, is the width of the "on" signal of the PWM signal. When it is sent to the control circuit, the corresponding switch closes for t seconds, enabling the assigned SMA wire actuator to be heated for t seconds. This time period should be limited to an upper value, t_{max}, which is used to prevent the temperature drop of other SMA wire actuators. When the wire is heated to a desired temperature, T_s, or heated for t_{max} seconds, the multiplexed control switches to monitor the next SMA wire actuator and therefore keeps all actuators under control. If the difference between T_s and T_m is smaller than the threshold, the system will switch to monitor next SMA wire immediately. The frequency of the control cycle should be high enough to prevent temperature drop. The control flow chart can be explained schematically in figure 4.12.

4.4.2 Image Feedback Controller

In the previous section, we designed a temperature feedback position controller based on the theoretical model that we developed. This approach enables us to control the joint motion of MINIR by monitoring the temperatures of the SMA wire actuators through the thermocouples attached to them. The temperature feedback control will only be used when the image tracking algorithm for the image feedback control fails.

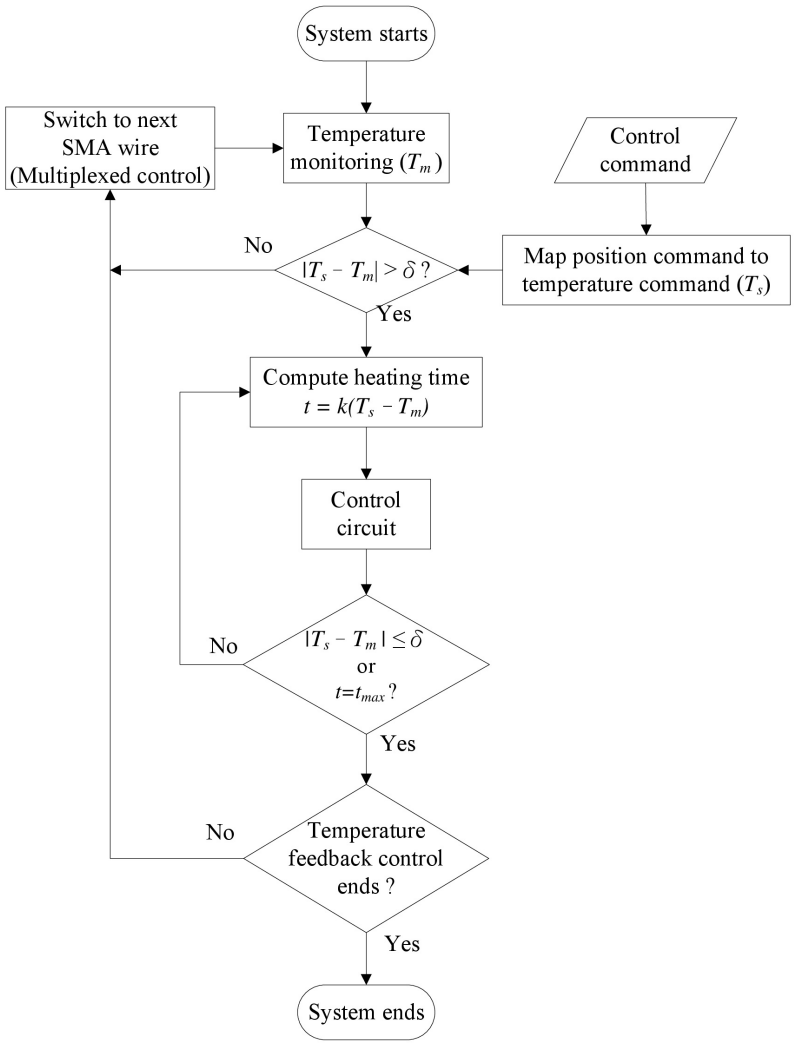

Figure 4.12: The proposed control flow chart of the temperature feedback controller.

The goal of this section is to design an image feedback controller for MINIR. The controller is used to track specific features on the robot and obtain the position of those features. After obtaining the positions of those features, we then use this information to compute the joint angle of each joint. The controller is required to control multiple joints simultaneously and independently, therefore, multiples points are tracked at the same time. To track the features of the robot, we used the Lucas-Kanade optical flow method [92]. Optical flow is widely used to track the motion of objects, surfaces, and

edges in an image sequence. It assumes that the flow is essentially constant in a local neighborhood of the pixel under consideration, and solves the basic optical flow equations for all the pixels in that neighborhood, by the least squares criterion.

The control flow of the image feedback control is similar to that of the temperature feedback control which we discussed in the previous section. Instead of monitoring temperatures in the SMA wires, we rely on the position information of each joint obtained using the image tracking algorithm. The current position, P_m, of each joint is computed from the tracking points that are selected manually in the images. The position command, P_s, of each joint can be sent either in real-time or pre-programed through a user interface. If the difference between P_s and P_m for a specific joint is larger than a threshold, δ, the corresponding SMA wire actuator will be activated for a period of time, t. The activation time can be computed using the following equation.

$$t = k(P_m - P_s) \tag{4.12}$$

The proportional gain, k, can be adjusted to change system response. Since MINIR is a serial robot, the payload of each link is different and thus the gain, k, is also different for each link. The control command, t, is the width of the "on" time of the PWM signal and it is sent to the same circuit discussed in section 4.4.1 (see figure 4.11). When the control command is sent to the circuit, the corresponding switch closes for t seconds, enabling the assigned SMA wire actuator to be heated for t seconds. This time period should be limited to an upper value, t_{max}, to prevent overheating of the SMA wire and the temperature drop of other SMA wire actuators. When the link is actuated to a desired

position, P_s, or activated for t_{max} seconds, the control system switches to monitor the next SMA wire actuator and therefore keeps all wires under control. If the difference between current position and desired position for a specific joint is smaller than the threshold, *i.e.*,$|P_s - P_m| < \delta$, the system will immediately switch to monitor the next SMA wire actuator. The control flow of the proposed image feedback control is shown schematically in figure 4.13.

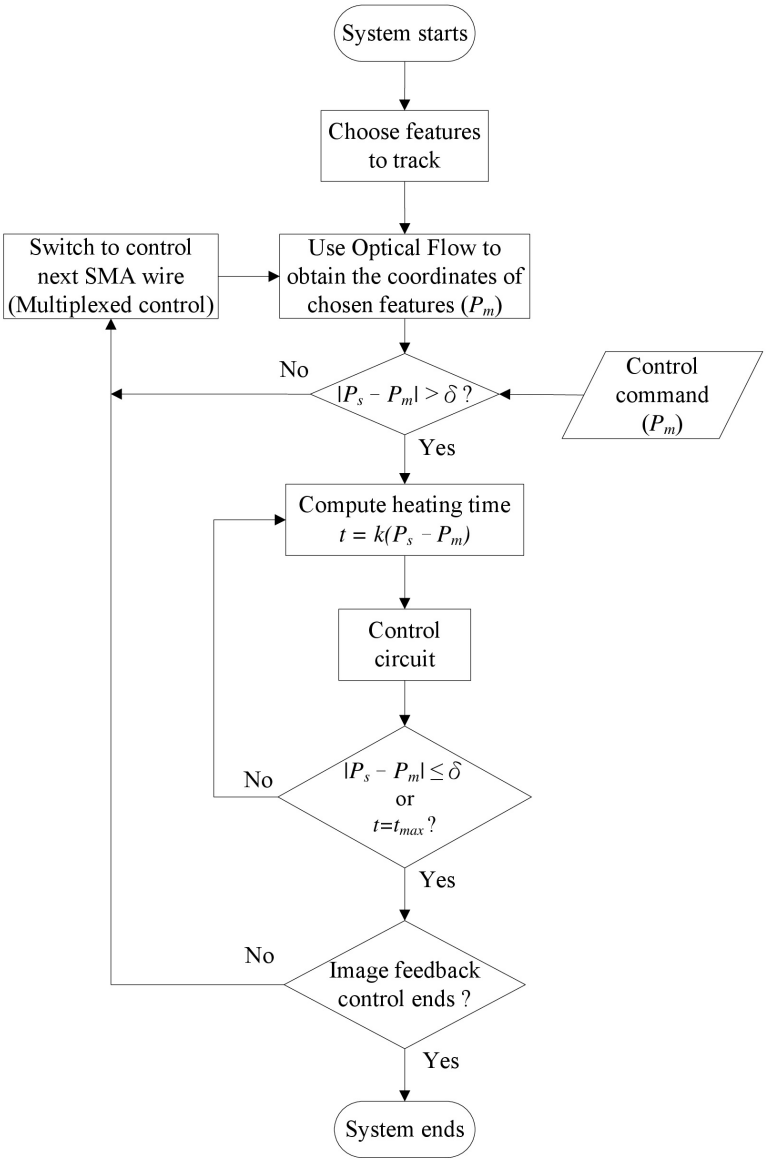

Figure 4.13: The proposed control flow of the image feedback controller.

4.5 Results

Since brass has been proven to be MRI-compatible and created no significant distortion in MR images [91], we chose brass to fabricate this prototype. Traditional machining was used to manufacture the links of this prototype, and the links were connected using plastic pins as shown in figure 4.14(a). The links, SMA wire actuators and electric wiring were assembled manually, and heat shrink tubes were used to isolate the SMA wire actuators from the brass links as shown in figure 4.14(b). As seen in the figure, all wires were routed inside the robot.

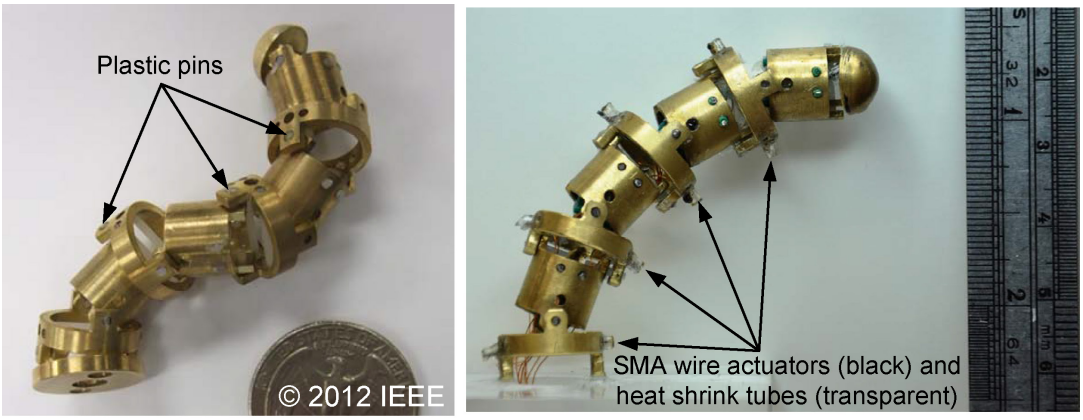

(a) (b)

Figure 4.14: (a) The manufactured brass prototype of MINIR and (b) the prototype with SMA waire actuators and electric wiring.

4.5.1 Single SMA Wire Actuation

We did experiments to demonstrate that the motion of a joint of MINIR with one SMA wire actuator was consistent with the theoretical model presented in section 4.3.1. In this case, one SMA wire actuator was pre-strained and attached to the joint. Constant current was applied to the SMA wire actuator through the PWM controller, and the thermocouple

readings and the joint motion were recorded continuously. The experimental setup is shown in figure 4.15 and the experimental results are shown in figure 4.16. The solid line in the figure is the theoretical model developed in section 4.3.1.

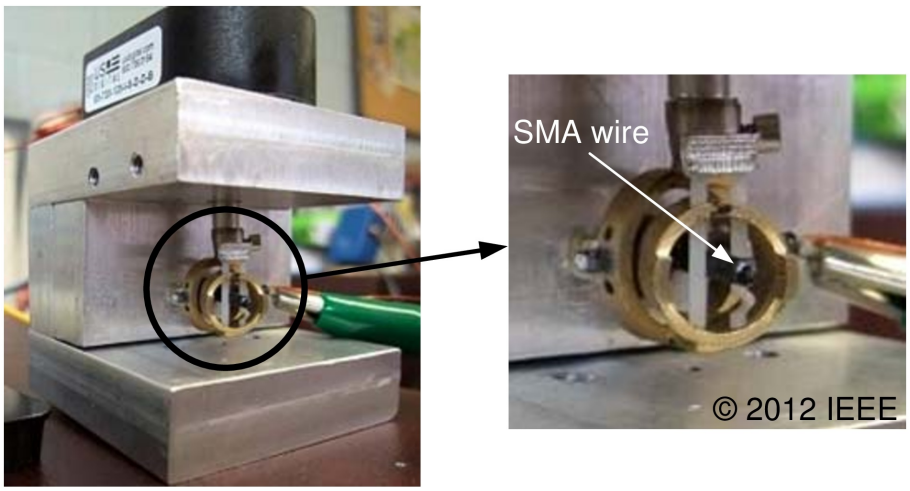

Figure 4.15: Experimental setup for the testing of a one-link MINIR actuated by a SMA wire actuator.

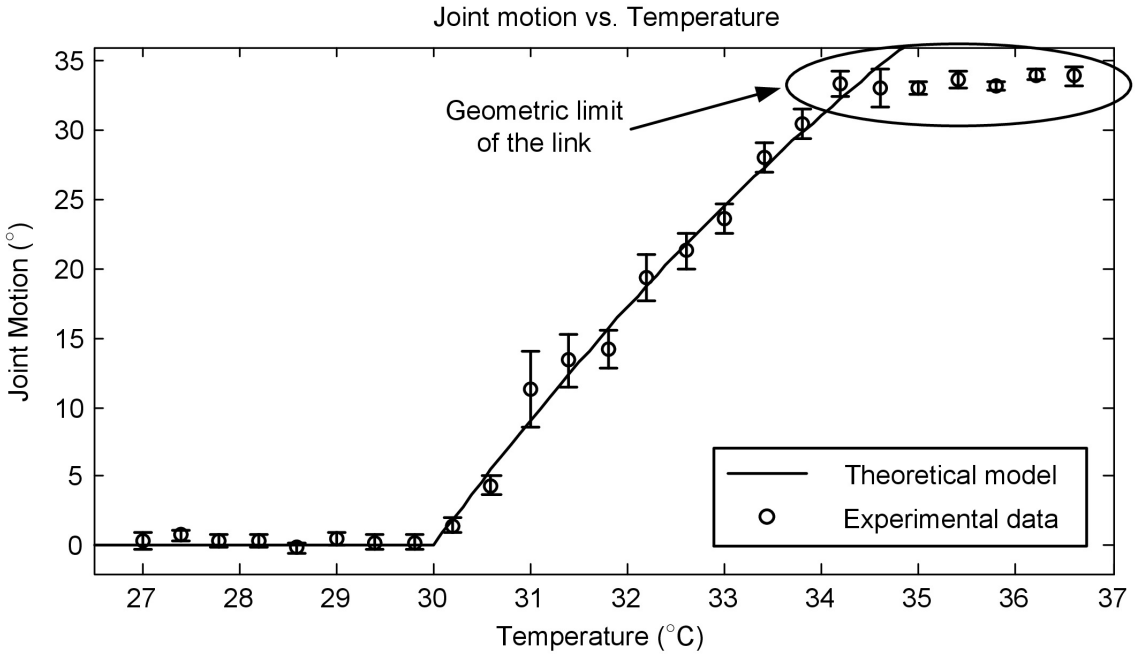

Figure 4.16: Experimental results of the joint motion vs. temperature for a joint of MINIR actuated by a SMA wire actuator.

The maximum error between experimental results and the theoretical model was

5.5° while the average error and standard deviation was 0.1° and 2.7°, respectively. The error arises primarily from different pre-strain levels of the wire because the space inside the robot is very tight. The SMA wire actuator cannot be bent to a perfect arc in a tight space. Thus, the initial strain was larger than expected and the SMA wire actuator tended to recover quickly with larger pre-strain which accounts for this discrepancy. The 5.5° maximum error leads to a 0.69 mm error in the horizontal displacement. Note that the maximum joint motion shown in the figure is due to the geometric limit of the joint.

4.5.2 Antagonistic SMA Wires Actuation

To verify the antagonistic actuation mechanism of MINIR, we actuated two antagonistic SMA wire actuators attached to a joint of MINIR to see if the joint can be moved back and forth as expected. The results are shown in figure 4.17, and we can clearly see that the antagonistic actuation mechanism works as expected.

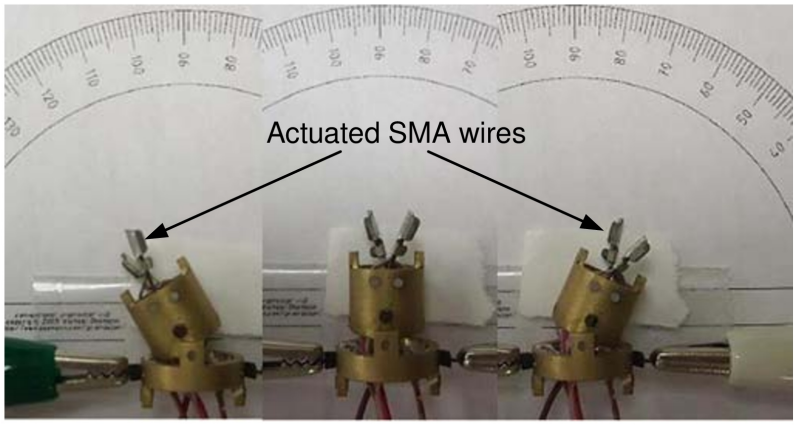

Figure 4.17: One joint of MINIR actuated by two antagonistic SMA wire actuators.

We then evaluated the positioning accuracy and the repeatability of the joint motion by measuring the temperatures in the SMA wire actuators and recording the correspond-

ing joint motion. The experimental setup is shown in figure 4.18 and the experimental results are shown in figure 4.19 and figure 4.20. Figure 4.19 shows the results when moving the link to the right side and figure 4.20 shows the results when moving the link to the left side. Experimental results fitted the theoretical model well, and the maximum error was 5.6° while the average error was 0.8°. The joint motion was observed to be repeatable across several trials with a standard deviation of 3.2°. The average maximum joint motion was about 30°. The results are very close to that of using one SMA wire actuator in the previous section but slightly different. This is because in the theoretical model, we assume that the SMA wire actuator is under a stress free condition. However, in the antagonistic mechanism, the actuated SMA wire has to bend the non-actuated SMA wire, which causes an external stress on the heated SMA wire. As we mentioned in Chapter 3, the transformation temperatures increase with stresses. Therefore, we can observe that the A_s in this experiment is slightly higher than the A_s that we measured in the stress free condition (*i.e.* 30°C). The increasing of the transformation temperature causes the theoretical model to shift to the right of the figures.

During actuation, the response time (from 0° to 30°) ranged from 12 seconds to 20 seconds, depending on the applied current, which was much faster than the cooling time (35 seconds under natural cooling). In the surgical application, we are not time constrained to carry out the procedure and thus the slow response is not a disadvantage. In fact, the robot should move slowly during electrocauterization to ensure that the tumor can be completely electrocauterized and thus the above heating and cooling times are acceptable. In general, electrocauterization takes several minutes at a single spot and the entire neurosurgical procedure usually takes hours to complete.

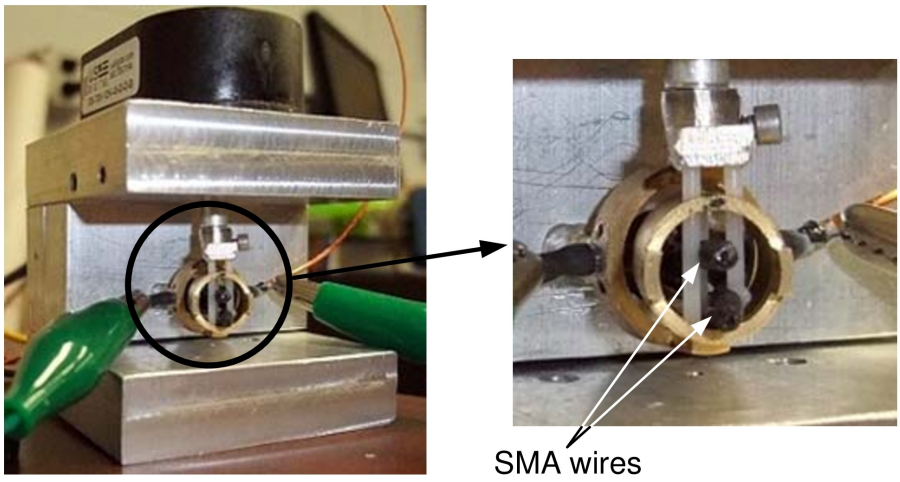

Figure 4.18: Experimental setup for the testing of a joint of MINIR actuated by antagonistic SMA wire actuators.

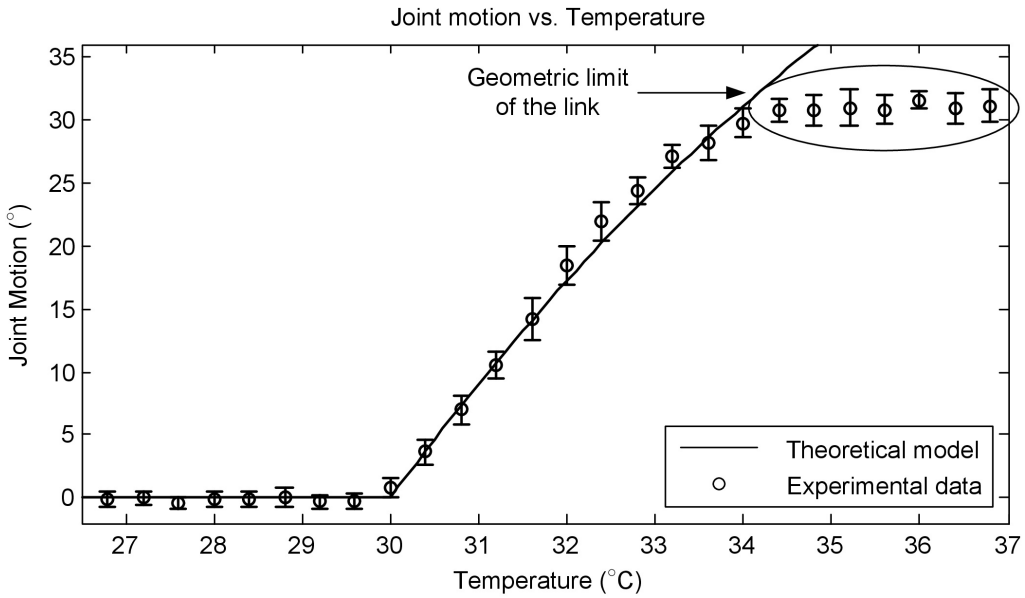

Figure 4.19: Experimental results of the joint motion vs. temperature curve for a joint of MINIR actuated by two antagonistic SMA wire actuators (move to left).

4.5.3 Force Test

For the force measurement, we used a similar experimental setup as that used to test SMA parameters in section 3.2. We extended the device to perform the tests of force-temperature relation by adding a force sensor, as shown in figure 4.21. The force sensor

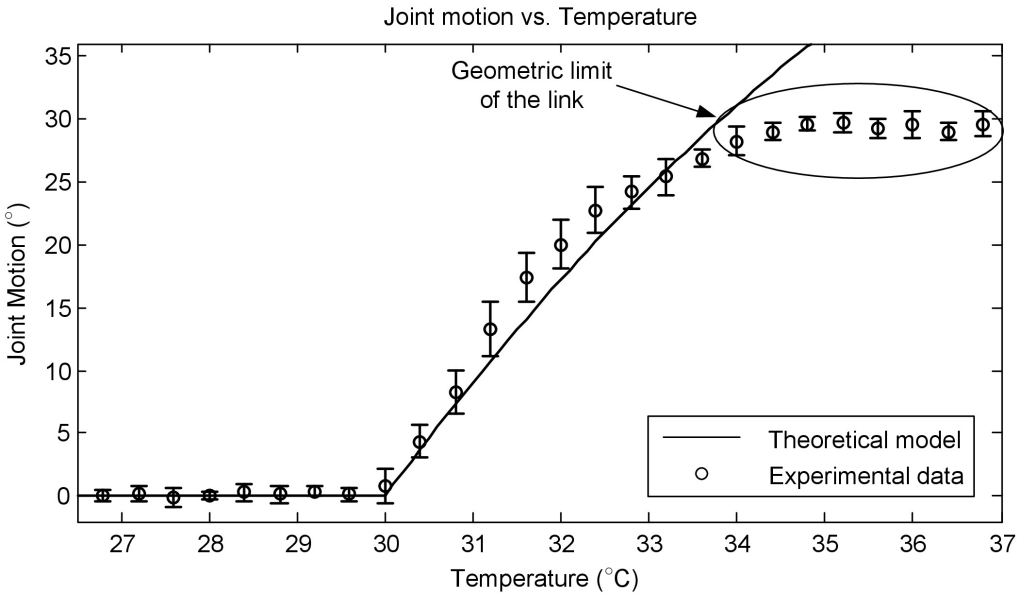

Figure 4.20: Experimental results of the joint motion vs. temperature curve for a one-link MINIR actuated by two antagonistic SMA wire actuators (move to right).

is MDB-2.5 load cell from Transducer Techniques, and the maximum force capacity is 10 N. Two 0.508 mm diameter SMA wire actuators were distributed antagonistically in a link of MINIR. The link was bent to a desired position and attached to the testing device. The SMA wire actuator was then heated to specific temperatures and the corresponding force readings were recorded.

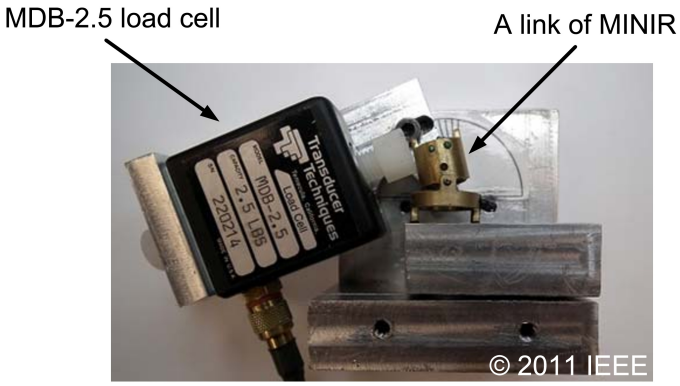

Figure 4.21: Experimental setup of force testing.

The experimental results are shown in figure 4.22 which were consistent with the

theoretical values that we derived in section 4.3.2. The maximum generated force at the tip of the link was about 1.4 N at 75°C, and the maximum forces at different positions were about the same.

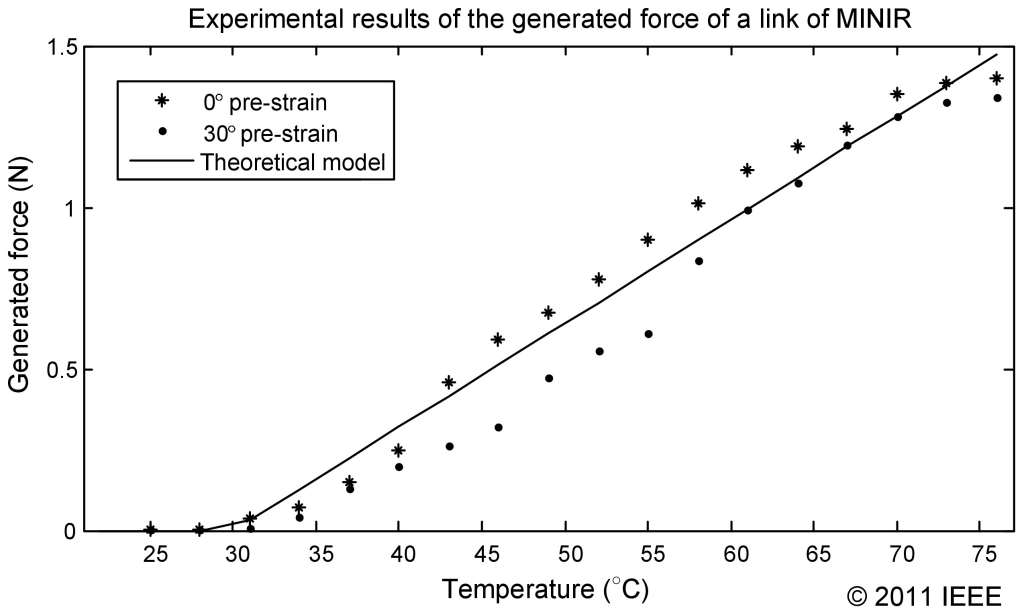

Figure 4.22: Experimental results of the generated force at the tip of a link of MINIR.

4.5.4 Test in Gelatin

We inserted a 3-DOF MINIR into a gelatin slab to make sure that the 1.4 N maximum force was enough for MINIR to move inside a tightly enclosed environment such as a human brain. We actuated each link independently with the tip link first and then the middle link followed the base link. The experimental results are shown in figure 4.23 and the width of each grid is 3.2 mm. The experimental results clearly demonstrate that the 3-DOF robot was able to move in a tightly enclosed environment and push the gelatin away. The horizontal displacement of the robot tip was about 20 mm, and the size of a typical brain tumor is in the order of 50 mm. Hence, we can say that the motion range of

MINIR is enough for our neurosurgical applications.

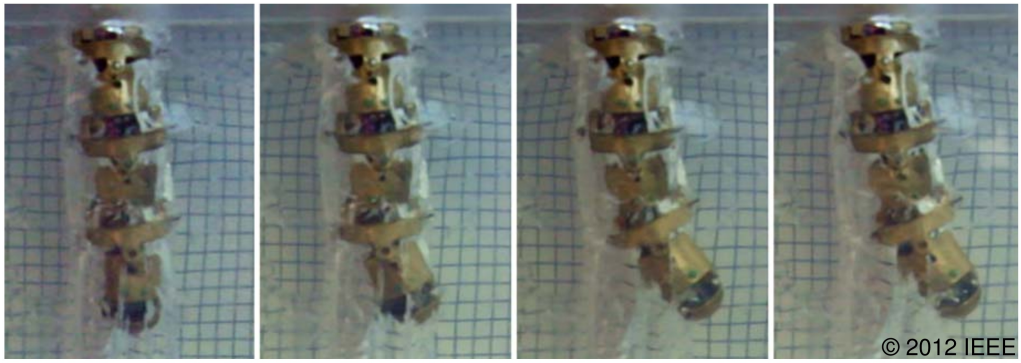

(a) (b) (c) (d)

Figure 4.23: Test of the 3-DOF MINIR in gelatin: (a) Neutral position, (b) tip link was actuated with a temperature of 50°C, (c) second link was actuated with a temperature of 60°C and (d) base link was actuated with a temperature of 60°C.

We also integrated electrocautery and suction systems to the prototype of MINIR. We tested them in the gelatin with MINIR to make sure they work as expected. We moved three joints of MINIR simultaneously to right and then to left. During the motion, we activated the electrocautery and suction systems to see if the electrocautery tips can melt the gelatin and if the suction system can suck the melted gelatin out. The experimental result is shown in figure 4.24. In the figure, we can see that the electrocautery tips melted the gelatin into liquid, and the suction tube sucked the melted gelatin liquid out creating a void in the gelatin. Furthermore, we can also see that only the gelatin which was in contact with electrocautery tips was melted. Other parts of gelatin was only pushed aside and left un-damaged after the test. This means MINIR will only electrocauterize the tumor which is in contact with the electrocautery tips and push healthy brain tissues aside during the procedure. Since brain tissue is highly compressible, the pushed brain tissue will not be damaged.

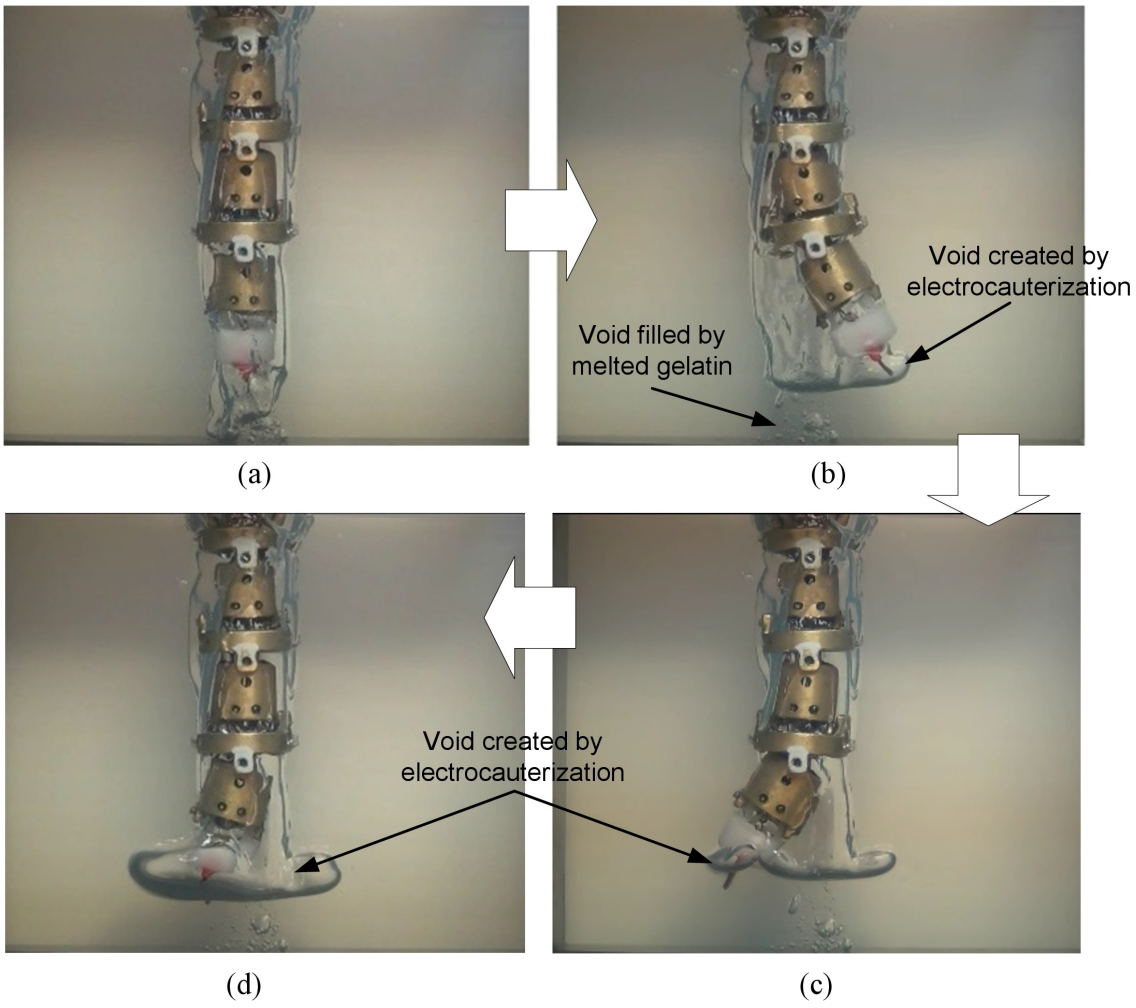

Figure 4.24: Test of electrocautery and suction systems with MINIR in gelatin

4.5.5 Temperature Feedback Control

For the testing of the PWM-P temperature controller, we used a D/A converter to generate PWM signals, and the control loop frequency was set to 20 Hz. Based on the open-loop response tests of SMA wires, the temperature threshold (δ) was set to 0.5°C and the maximum heating period (t_{max}) was set to 0.3 seconds. For the multiplexed control circuit, we chose to use solid state relays (SSRs) as switches. SSRs are more compact and faster than electromechanical relays; their switching time is on the order of milliseconds, which satisfies our requirement of high frequency switching. In the experiment, we heated four

SMA wires to 70°C individually and maintained the temperatures of the fours SMA wires at 70°C by using one power supply. The experimental results are shown in figure 4.25. The results show that the controller was capable of heating multiple SMA wires while maintaining the temperature of other wires and only one power supply was needed. At steady state, the average error in temperature was -0.6°C and the standard deviation was 2.1°C. The results were acceptable but not good enough since the 0.6°C error in temperature leaded to a 3.6° error in the joint motion.

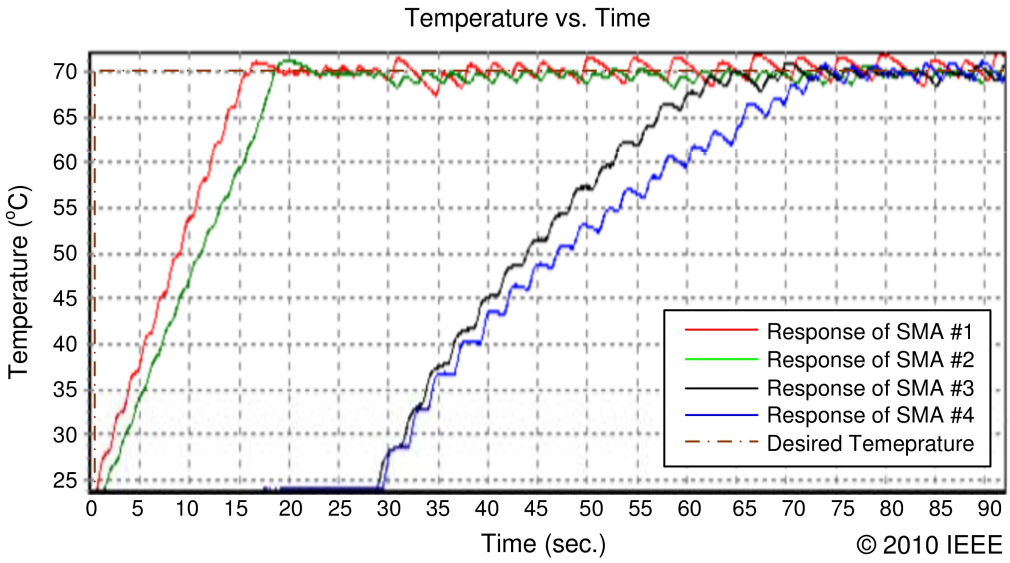

Figure 4.25: Test of the PWM-P temperature controller for four SMA wires.

To improve the control performance, we then used a PWM-PI controller instead of the PWM-P controller to repeat the same experiment. In the PWM-PI controller, the heating time was computed using:

$$t = K_p e + K_i \int (e) dt \tag{4.13}$$

The proportional gain, K_p, and the integral gain, K_i, can be tuned to adjust the system

performance, and e represents the difference between T_s and T_m, *i.e.* $e = T_s - T_m$. The experimental results of the PWM-PI temperature controller are shown in figure 4.26. Using the PWM-PI controller, the average error in temperature dropped from -0.6°C to -0.09° and the standard deviation dropped from 2.1°C to 0.58°C. The various slopes in the figure are the heating rates of the SMA wires. It is obvious that the heating rate of SMA Wire # 4 is slower than that of SMA Wire # 1 because the controller had to maintain the temperatures of the other three SMA wires while heating SMA Wire # 4. Since the energy provided by the power supply was constant, when more wires were controlled, the heating rates were slower. Through this temperature control test and the previously described joint motion vs. temperature results, we can control the motion of each joint of MINIR simultaneously and independently by using the PWM-PI control scheme with temperature feedback.

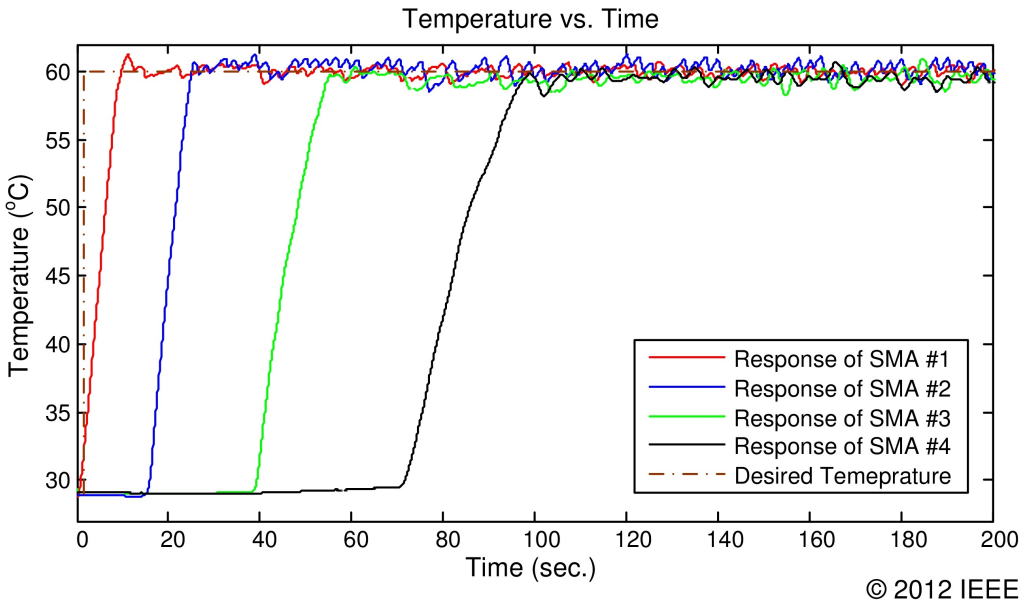

Figure 4.26: Test of the PWM-P temperature controller for four SMA wires.

4.5.6 Image Feedback Control

To determine if we can use an image feedback controller to reliably control the joint motion of MINIR, we implemented an image tracking algorithm using Lucas-Kanade optical flow method. By tracking the fiducial placed at each joint of the robot, we can compute the joint motion of each joint. The measured joint position can be compared with the desired joint position and a straightforward proportional control scheme was used. The experimental setup is shown in figure 4.27.

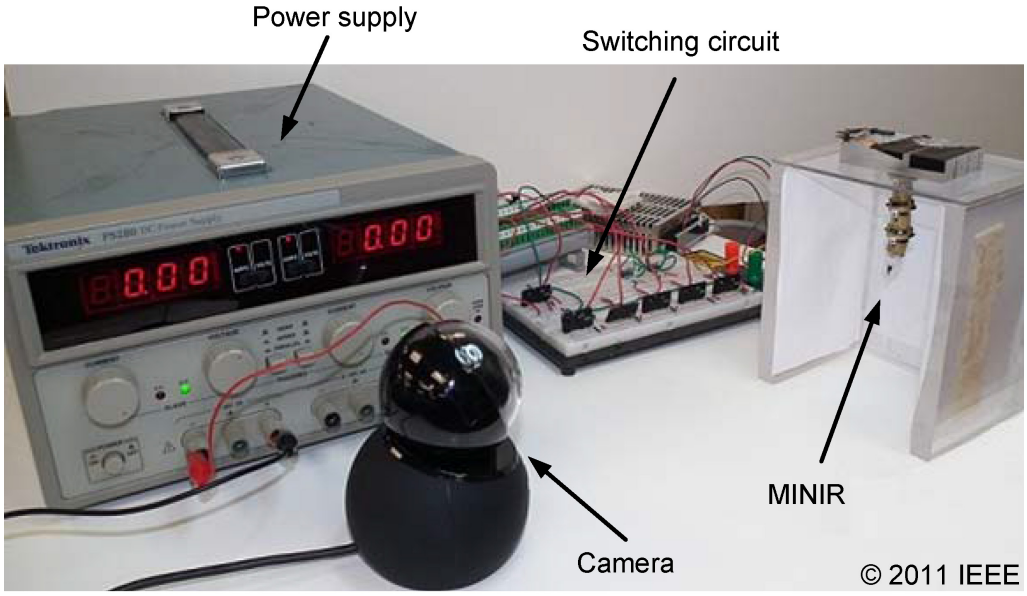

Figure 4.27: The experimental setup of the image feedback control of MINIR.

In the experiment, we first moved the robot to a specific configuration (base link: 10°, middle link: 20° and tip link: 35°) and then moved the tip link back and forth to simulate the motion of removing the tumor using electrocautery and maintained the other two links at the same positions. Note that after reaching the set point, the link cooled down for 20 seconds before the new command was sent. The positioning results are shown in figure 4.28, where it clearly shows that the image feedback controller can be used reliably

to control the motion of MINIR. It also demonstrates that the controller was capable of controlling multiple links simultaneously and independently while using only one power supply. Figure 4.29 shows three different positions of MINIR when controlled using an image feedback control scheme.

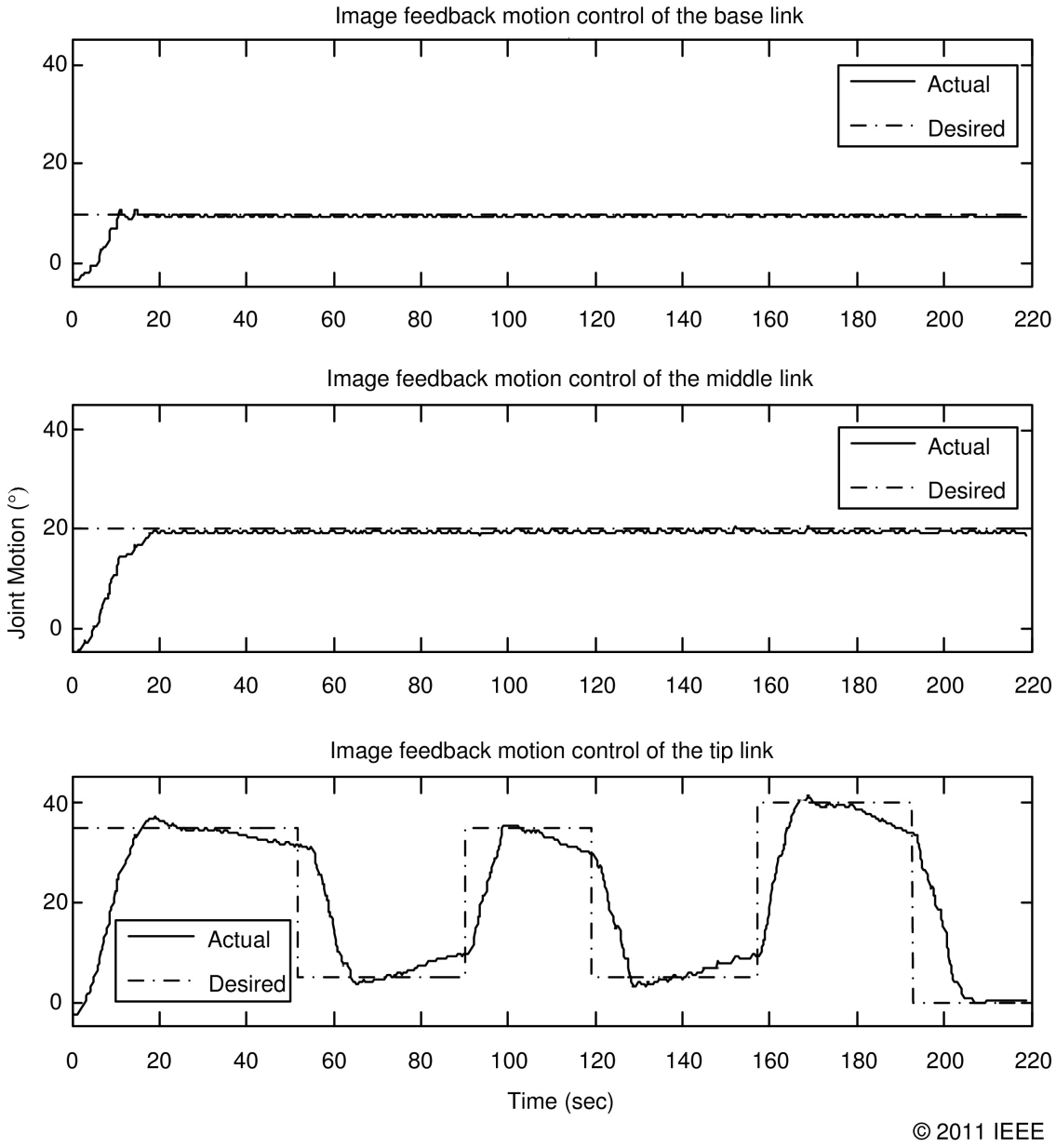

Figure 4.28: Experimental results of the image feedback position control of MINIR.

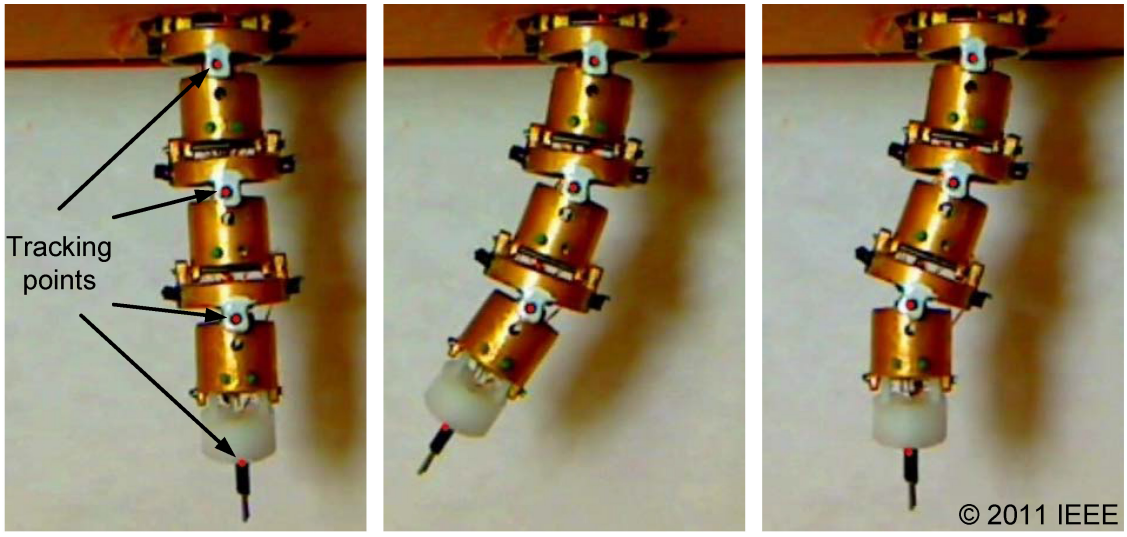

(a) (b) (c)

Figure 4.29: Three different configurations when performing image eedback control of MINIR: (a) Original position, (b) actuated to 10°, 20° and 35° and (c) actuated to 10°, 20° and 0° respectively.

4.5.7 MRI Compatibility Test

For the MRI compatibility test, we first took MR images of the two major links of MINIR to show that the materials were MRI-compatible. To quantify the induced disturbance to the images, we computed SNRs of the images, where SNR is defined as the ratio of the mean pixel intensity of signal in a Region Of Interest (ROI) and the standard deviation of the pixel intensity of the background noise in a ROI [93]. The links were put inside water to test their MRI compatibility. The SNR value computed without any links in the water was 111.7 which served as ground truth for comparison and the SNR with the links in water was computed to be 88.4. Though there was a decrease in SNR from the ground truth, it was still high and we were able to identify the various link components in the MR image as shown in figure 4.30. The bright white spots in the images were caused by the sharp edges of the link profiles, which could be fixed by rounding the edges.

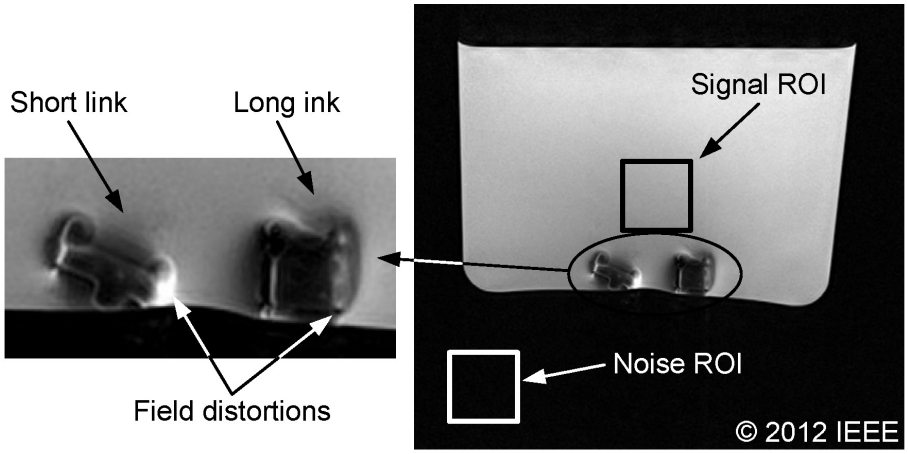

Figure 4.30: MR Images of the major links of MINIR: (a) side view of the links and (b) the regions of interest used to compute SNR.

We further evaluated the image quality of a 3-link MINIR with all wiring. The robot was put in the gelatin, and it was surrounded by gelatin to simulate the tightly enclosed environment in a brain as seen in figure 4.31(a). The MR image of the robot is shown in figure 4.31, where the electrocautery tips of the robot can be clearly identified. Since the electrocautery tips are at the tip of MINIR, the clarity of the tips in the MR images will enable us to control the motion of MINIR using MR images as feedback. Note that there were some blurred areas around other links. They were caused by air cavities which were created when we inserted the robot into the gelatin. The noise also came from the existing metal parts and wiring. When taking MR images, the magnetic field through the MRI scanner is changing. The varying magnetic field can generate Eddy current on a conductive object and thus create noise onto the MR images. Another reason is that the wiring served as antennas which collected all signals in the MRI room and thus reduced the image quality. The Eddy current on the MINIR links can be avoided by replacing brass links with plastic ones. The antenna effect can be minimized by using shield cables and

filters. However, since the profile and the tip position of the robot are identifiable in the image and there is no significant distortion on the surrounding gelatin, we will continue to use the brass prototype to do the following tests at this point.

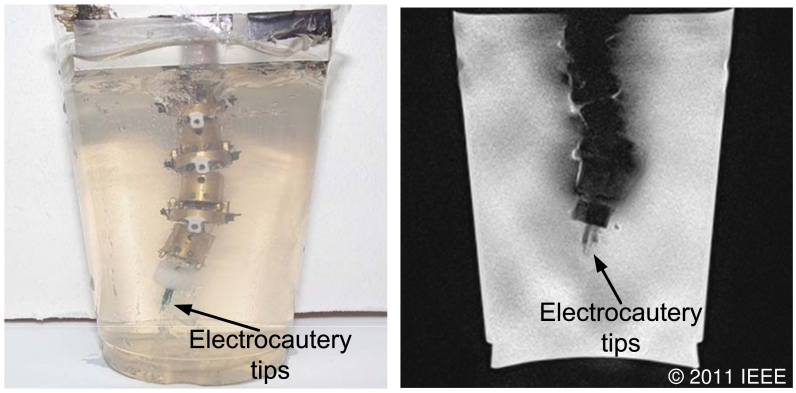

(a) (b)

Figure 4.31: (a) The 3-link MINIR in gelatin and (b) MR image of the 3-DOF MINIR in gelatin.

We have evaluated the MRI compatibility of MINIR when it was not actuated in the previous paragraphs, and the results showed that the hardware of MINIR brought no significant distortion to the MR images. We then continued to test the MRI compatibility of MINIR when it was actuated. We first actuated two joints of MINIR in a 3-Tesla MRI scanner to verify the MRI compatibility and to make sure that the range of motion was not affected by the strong magnetic field. We put the robot in the center of the MRI scanner and actuated it. The test result, shown in figure 4.32, shows that MINIR could be moved back and forth in the MRI scanner without significant interference from the strong magnetic field. The motion range was close but smaller compared to the result in figure 4.17 because one more link was added.

Finally, we evaluated the dynamic images that were taken continuously while MINIR was actuated. MINIR was successfully actuated in the gelatin while the MRI scanner was

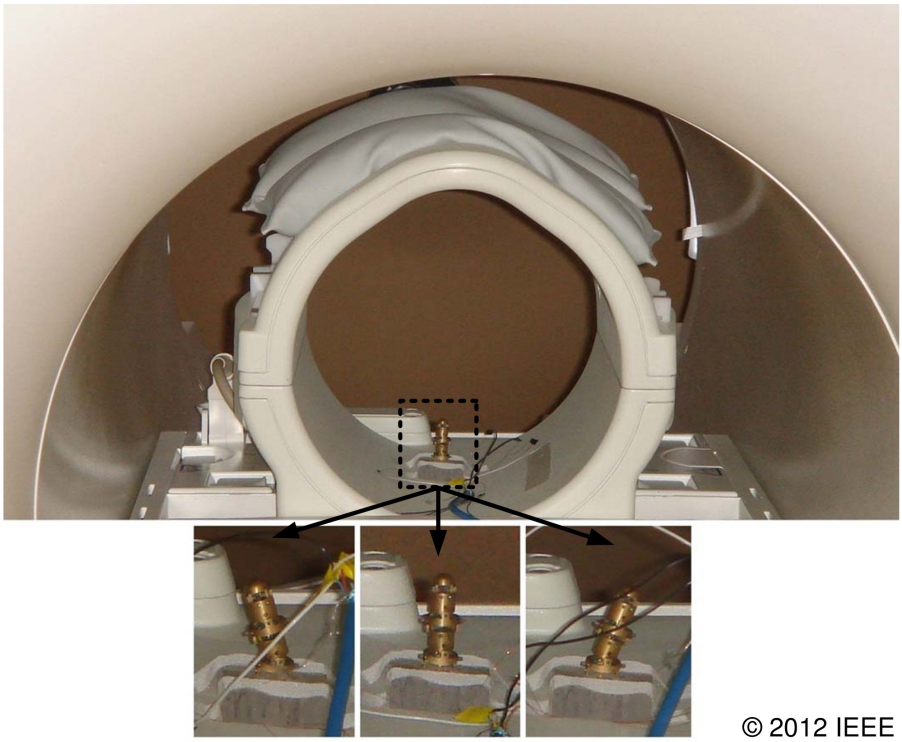

Figure 4.32: Test of two joints of MINIR in a MRI scanner.

running. The dynamic MR images are shown as figure 4.33 with no significant distortion in the images was observed. The figure shows three different configurations of MINIR when actuated inside a MRI scanner. The profile of the robot is clear and the tip position can be easily identified in the images. We observed very little distortion in the images during the operation of MINIR but this distortion did not lead to image loss or the inability to see the complete object. There were a total of 200 images taken during the actuation and we have computed the SNR of each image and it is shown in figure 4.34. MINIR was actuated at the 15^{th} second. The average SNR before actuation was computed to be 37.4 and it dropped to 31.4 during actuation. The SNR only dropped by about 16%, which implies that passing the current through MINIR did not cause significant noise in the MRI images.

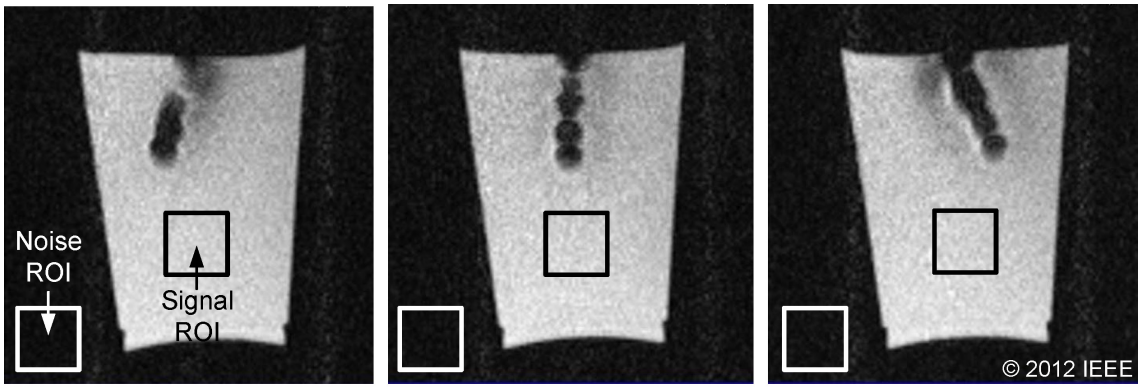

Figure 4.33: Dynamic MR images of the 2-DOF MINIR in gelatin.

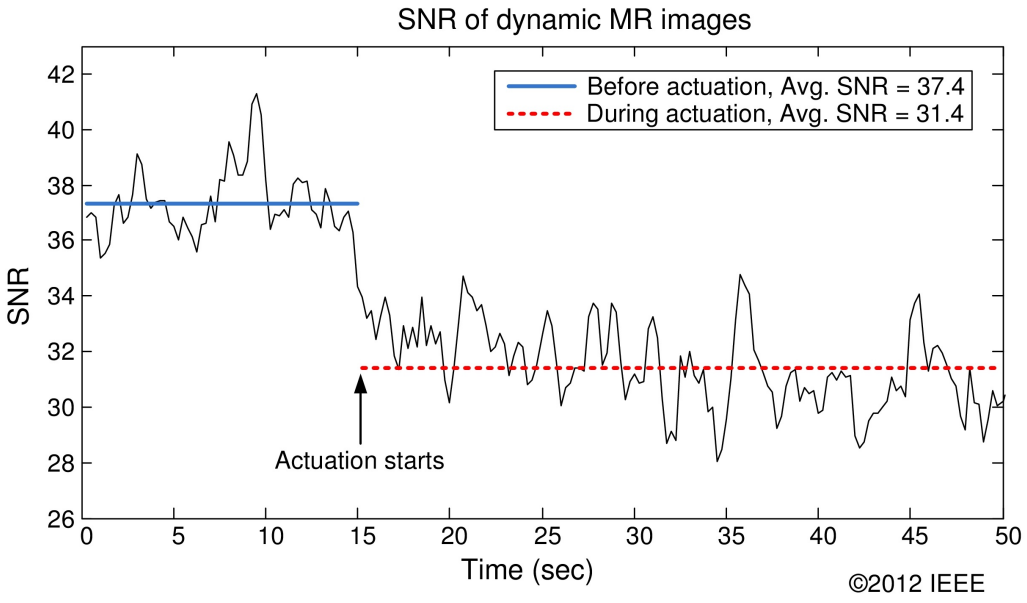

Figure 4.34: SNR of dynamic MR images.

The results also provided a feasibility that a physician can track the tip position of the robot visually under continuous MRI when performing deep brain tumor resection. Which can help physician to remove a brain tumor completely while minimizing trauma to the surrounding healthy brain during intracranial procedures.

We further demonstrated that we can control the robot to move toward the target based on the information from MRI. We used omentum from rats to simulate a brain

tumor and embedded it into gelatin as a target. Omentum is a large fold of peritoneum that hangs down from the stomach, and extends from the stomach to the posterior abdominal wall after associating with the transverse colon. The major composition of omentum is fat, which provides good contrast in MR images. We inserted the robot into the gelatin embedded with omentum (see figure 4.35), and the electrocautery tips of the robot were 12 mm from the omentum. The gelatin and the robot were placed at the center of the MRI scanner. We then took MR images continuously (the frame rate was 4 fps) while actuating the robot manually toward the omentum. Note that all devices except MINIR were outside the MRI room. All power and control signals were delivered to MINIR through shield cables and a filter panel on the wall of the MRI room. The MR images are shown as figure 4.36. The initial position of the robot is shown in figure 4.36(a), and the final position is shown in figure 4.36(b). The images of the tip link of the robot is clear, and the electrocautery tips can be easily identified in the images. The imaging results prove that physicians can track and control the tip position of the robot visually under continuous MRI when performing electrocauterization.

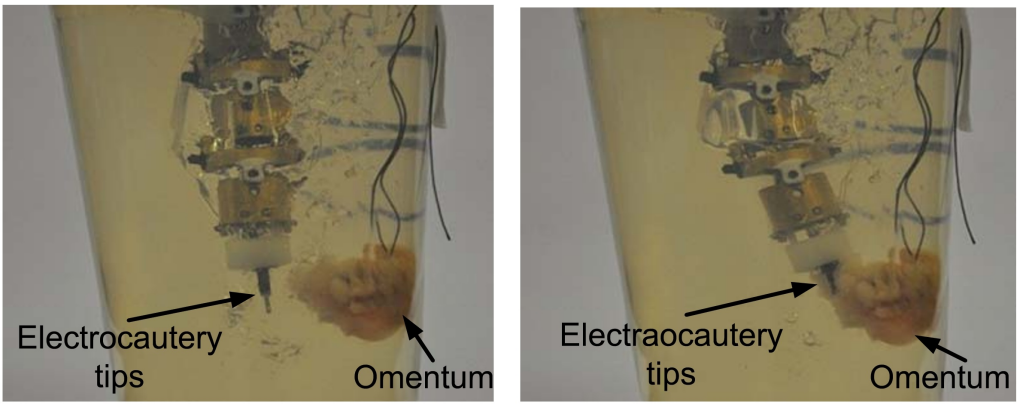

(a) (b)

Figure 4.35: (a) Initial position and (b) final position of MINIR when controlled to move toward the omentum target.

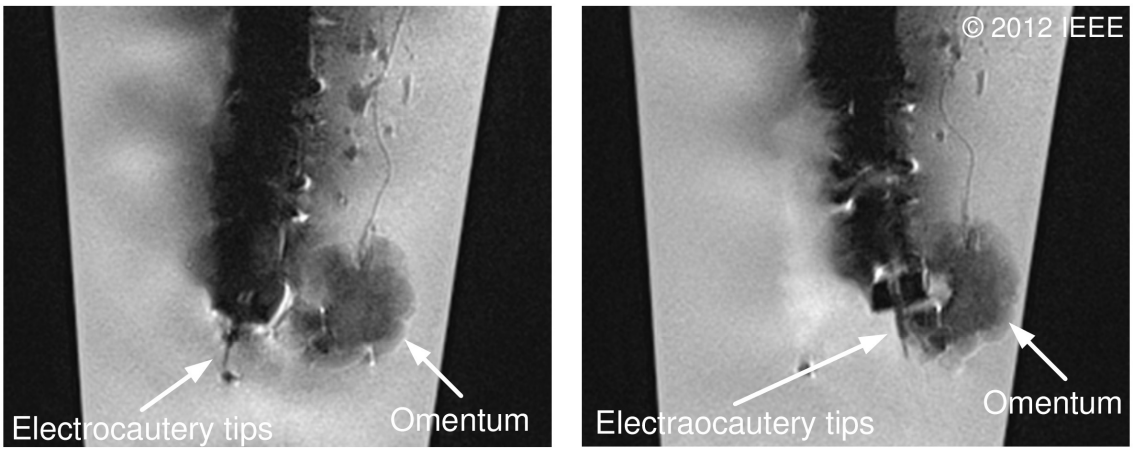

(a) (b)

Figure 4.36: MR images of the (a) initial position and (b) final position of MINIR when controlled to move toward the omentum target.

4.5.8 *Ex-Vivo* Test

For the *ex-vivo* experiment, we embedded omentum into the brain of a Yorkshire pig to simulate a brain tumor. The omentum provided a distinct contrast in comparison with the brain tissue in MR images. The major composition of omentum is fat so it could be liquefied during electrocautery procedures and thus could be used to verify the function of the implemented electrocautery system. The MRI images of the pig brain are shown in figure 4.37. A gradient echo acquisition with an echo time of 2.46 ms and a repetition time of 300 ms, *i.e.*, TE/TR = 2.46/300 ms, was used. In the images, the material that contains water is shown in white which is the color of water in MR images while black represents the material that contains no water, for example, air, metal, and plastic. The skin, skull, brain tissue and omentum can be clearly identified in the images and the opening on the skull can also be seen in the images.

To evaluate the performance of MINIR in brain tissue, we tested the MINIR in the

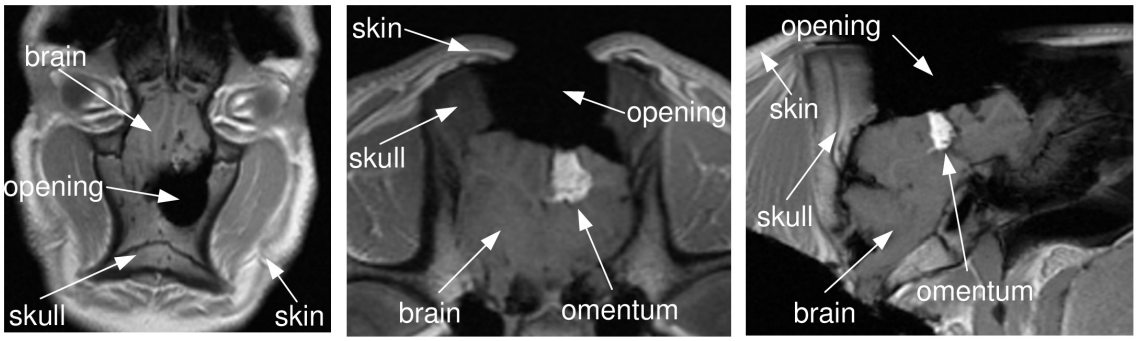

(a) (b) (c)

Figure 4.37: MRI images of the pig brain with omentum embedded: (a) top view, (b) front view, and (c) side view of the brain.

pig brain. MINIR was covered with a plastic sheath to isolate from tissue, blood and other liquids and only the electrocautery tips are outside the isolation as seen in figure figure 4.38(a). We inserted MINIR into a surgical opening created on the skull as shown in figures 4.38(b) and 4.38(c). Before actuating MINIR, we also put gelatin into the opening of the brain to fill the air gap in between brain tissue and MINIR and therefore increased the visibility of MINIR in the MR images. We then actuated MINIR to move back and forth under dynamic MRI and the MR images are shown in figure 4.39. In this test, the TE/TR was set to 2.24/100 ms. In the images, we can see that MINIR was successfully actuated to move back and forth while creating no significant image distortion. Moreover, the electrocautery tips can also be identified, which enables us to track the tip position in the image feedback control.

In the following experiment, we took continuous MRI images to qualitatively and quantitatively compare the influence of the actuation of MINIR in the MR images. There were totally 400 images taken during the test. In the first 100 images, all devices used in MINIR including power supply and electrocautery signal generator were off. This set of images were used as the ground truth for comparison in this experiment. In the

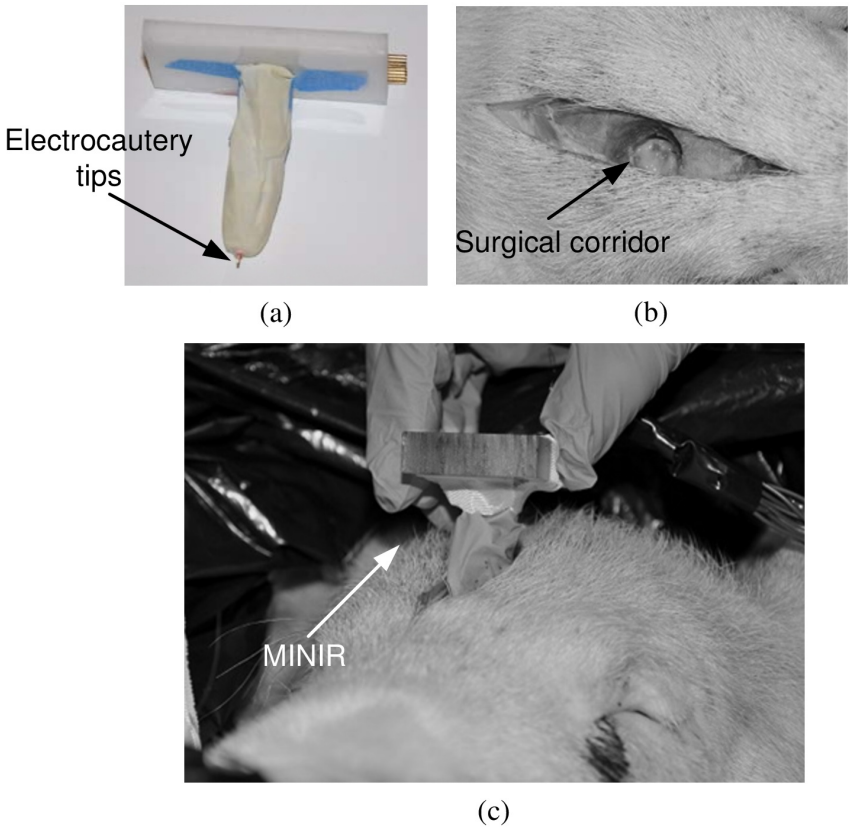

Figure 4.38: Photos of (a) MINIR cover with plastic sheath and only electrocautery tips are outside, (b) the surgical corridor created on the skull of the pig and (c) the introduction of MINIR.

next 100 images, the power of all above mentioned devices were turned on but MINIR was not actuated, *i.e.*, no electric current passing through SMA wire actuators. MINIR were then actuated, *i.e.*, passing electric current through SMA wire actuators, for 100 images and kept un-actuated for the next 100 images. Four MR images are shown in figure 4.40 which represent four conditions of MINIR in the experiment. There were no observable differences between the images of all devices off and all devices on [see figures 4.40(a), 4.40(b), and 4.40(d)]. However, there was some image distortion showed up during actuation (see figure 4.40(c)).

To quantitatively compare the influence of the actuation of MINIR in the MR im-

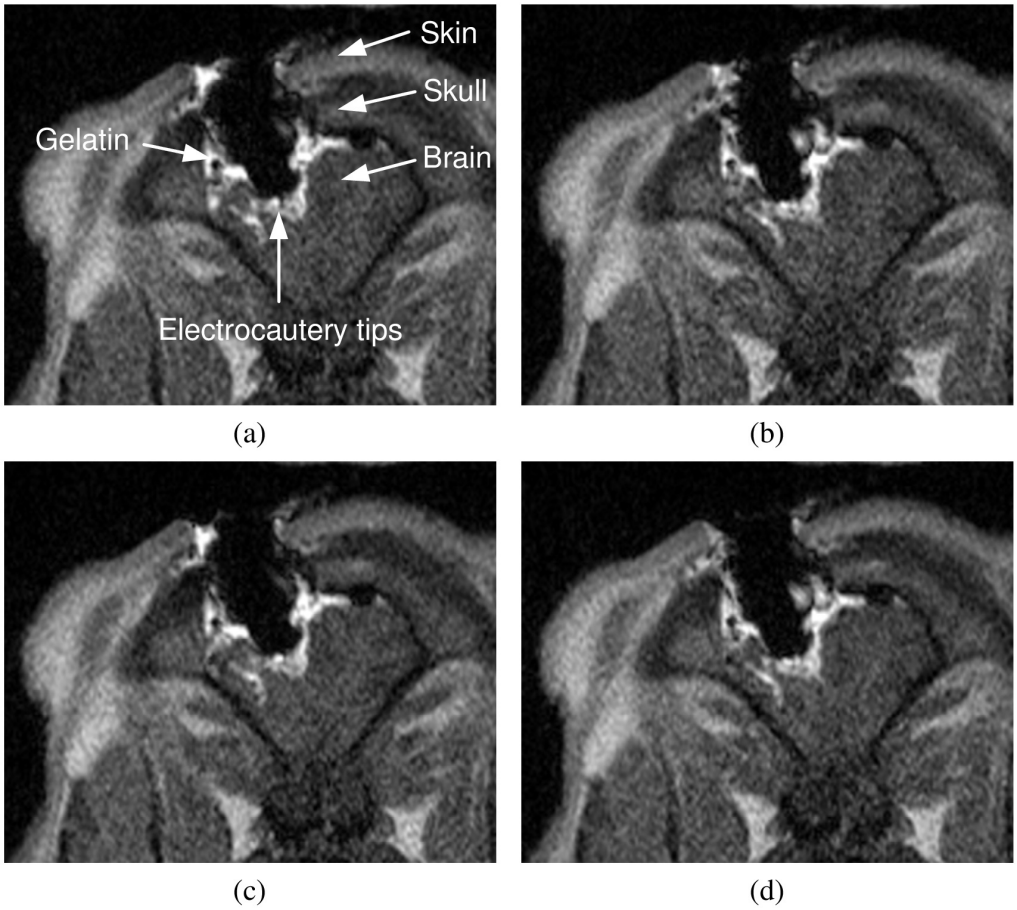

Figure 4.39: MR images of MINIR actuated to move back and forth in a pig brain: (a) Neutral position, (b) move to left, (c) move to right, and (d) back to neutral position.

ages, we computed the SNR of all images. The results are shown in figure 4.41 and the values are consistent with what we concluded from previous paragraph. The SNR values were the same for the devices power off condition and the devices on condition. However, the SNR dropped by 6.6% (25.9→24.2) during actuation. The results clearly indicated that the actuation of SMA wire actuators do bring noise to MR images. Although the influence was not significant, it is still advantageous for MINIR if the noise in the MR images can be completely eliminated. Therefore, we will proposed a new design of MINIR to address this issue in the next chapter.

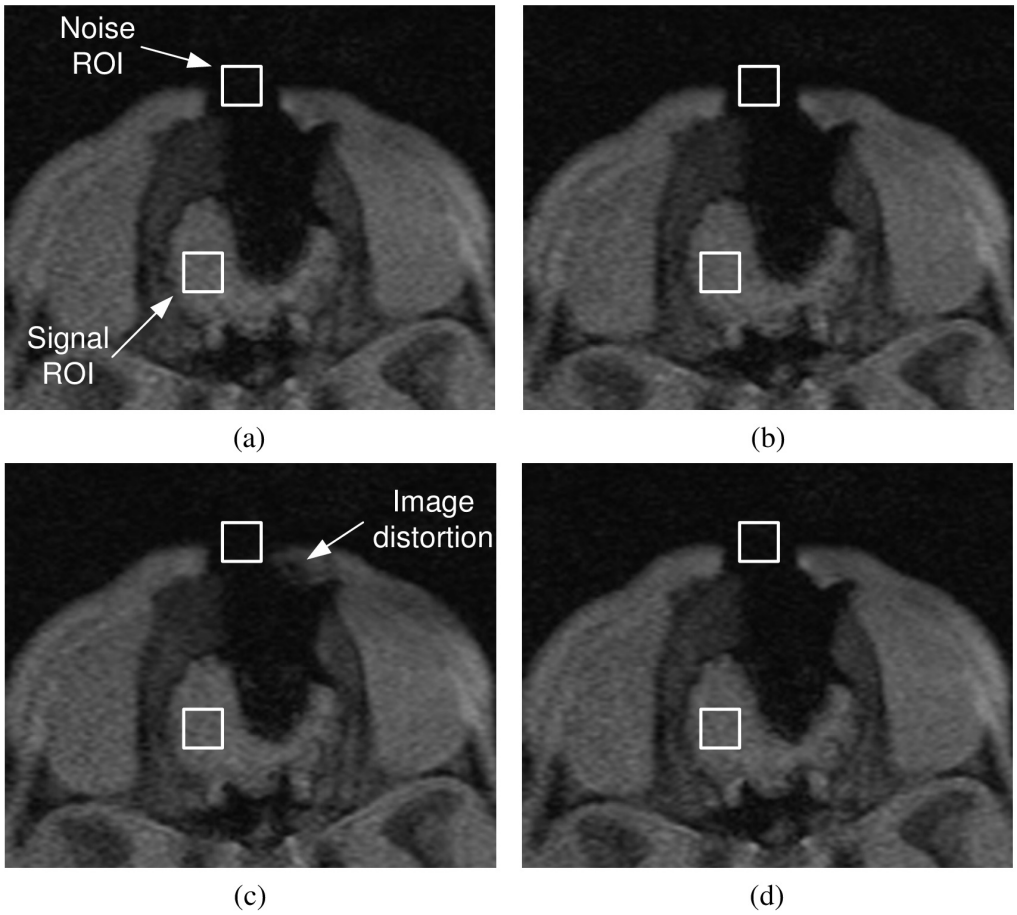

Figure 4.40: MRI images of MINIR at different conditions in a pig brain: (a) Power off, (b) power on but no actuation, (c) during actuation, and (d) power on but no actuation.

4.6 Summary

In this chapter, we presented the second generation of MINIR. In this prototype, each joint can be independently actuated and all wiring can be put inside the robot. This new design gave MINIR a larger motion range and better controllability than the first generation. An experimental setup for obtaining SMA material parameters of analytical model and the performance evaluation of MINIR was also presented. We further investigated the behavior of the SMA wire actuator and determined material parameters experimentally. The experimental results of motion test showed that the motion of MINIR could be controlled

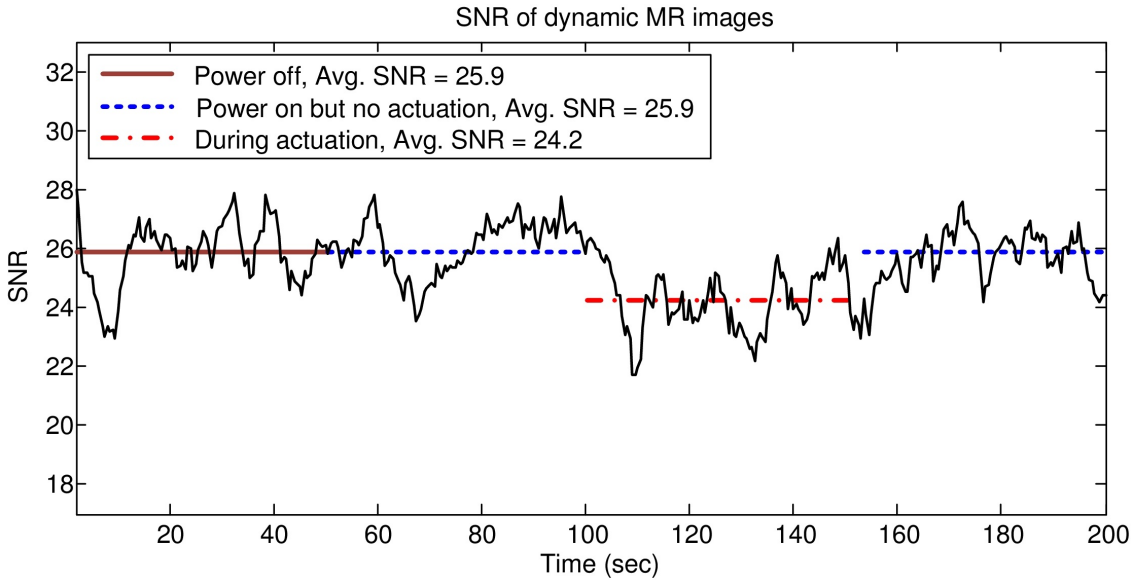

Figure 4.41: SNR of dynamic MR images.

through temperature feedback based on the theoretical model that we developed. Moreover, we successfully used PWM and multiplexed control to control multiple joints, for example, SMA wire actuators, simultaneously and independently using only one power supply. Image feedback control has been successfully used to precisely control the joint motion of multiple joints of MINIR. The results provided a feasibility of using real-time MR images to control the motion of MINIR.

We also modeled and measured the force behavior of SMA wire actuators in bent configurations. The model can be used as a guideline to correctly select the size of the SMA wire actuator. In addition, we evaluated the motion of the robot in gelatin and observed that the generated force was enough for the robot to move inside the gelatin and the motion range was sufficient for neurosurgical applications. During the experiments, we noticed that when more links were added to MINIR, the joint motion was not the same for all joints while the motion was repeatable for a single link. However, this is expected

since additional loading on the proximal link due to distal links causes increased stress on the SMA wires. This can be addressed by using larger diameter SMA wires for the base joint compared to the distal joints in our future prototype. The embedded electrocautery and suction systems were also tested. The electrocautery tips successfully melted the gelatin and the melted gelatin liquid was sucked out by the suction tube.

A series of tests have been done to demonstrate that MINIR is MRI compatible. The motion range of MINIR was not affected by the strong magnetic field of MRI. We took both dynamic and static MR images of the robot. The results showed very limited image distortion which will not affect the image quality of the surrounding tissue. Although the SNRs of the images dropped by up to 16% when the robot was actuated, the dynamic MR images showed no significant artifacts and the robot profile could still be identified in the images. This result provided a possibility to use the MRI images as visual feedback when performing a deep brain tumor resection and therefore greatly increase the survival rate of patients who suffered from this most feared complications of cancer. Although the quality of MR images was good enough for physicians to control the robot manually, it is still not good enough for automating or semi-automating the procedure.

Overall, the prototype of a minimally invasive intracranial robot was successfully implemented and tested with good results. The next step of this research will focus on improving the MR image quality by using plastic material rather than brass to make the robot and by developing new actuation mechanisms that can minimize the SNR drop when it is actuated.

Chapter 5

Development of the SMA Spring Actuated MINIR

In this chapter, we present the design and experimental results of the latest prototype of MINIR. The third generation of MINIR was made of Delrin® and used SMA spring actuators along with tendon-sheath actuation mechanisms to actuate. The design of the robot and the antagonistic SMA spring actuation mechanisms are presented in section 5.1. The modeling of the SMA spring actuator is discussed in section 5.2. Section 5.3 describes the characterization of SMA springs and section 5.4 shows the experimental results of motion test, force test, control test and MRI compatibility of MINIR. Finally, in section 5.5, we make some concluding remarks. Most contents of this chapter are published in [94–96].

5.1 Robot Design

5.1.1 Design of MINIR using Cable-Driven Mechanisms

To eliminate the noise in MR images completely, we investigated the use of a cable-driven mechanism to actuate MINIR. Using cable-driven mechanisms, the actuators can be placed far away from the robot and only cables and pulleys would be inside the robot. Since actuators are away from the imagining region and cables and pulleys can be made of plastic, we believe that the noises in MR images can be minimized. Moreover, using cable-driven mechanism in the design of MINIR leads to lesser weight of the robot. Therefore, we decided to use cable-driven mechanisms in the preliminary design of the

third generation of MINIR. Figure 5.1 shows the schematic of our preliminary design of the third generation of MINIR. The robot had four revolute joints and the joints were placed orthogonally to have out-of-plane motion capability. Each joint had an independent single degree of freedom and the motion range of each joint was $\pm 60^{\circ}$. Each joint was actuated by an actuator through the cables connected to the corresponding pulley. The robot was hollow which allowed the cables to be routed inside the links. Each cable had to be routed through a pulley at each joint to decouple interactions between joints. The robot was 63.5 mm long and the largest diameter was 14.5 mm. The maximum horizontal displacement of the end-effector was about ± 80 mm which is larger than the size of a typical brain tumor.

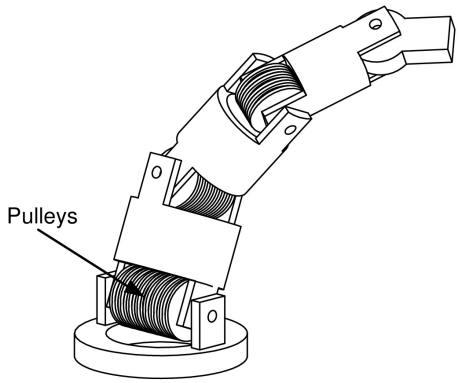

Figure 5.1: Preliminary design of the third generation of MINIR using cable-driven actuation mechanisms.

The actuation using cable-driven mechanisms was successful but it had some limitations. A pulley was required for each cable and all cables were required to be continuously under tension. The pulleys occupied a significant amount of space in the hollow robot body making the routing of suction tubes and electrocautery wiring difficult. Since MINIR is to be inserted into a brain through a flexible surgical corridor, it is difficult to keep all cables in tension.

5.1.2 Design of MINIR using Tendon-Sheath Mechanisms

To overcome the above limitations, we re-designed the robot with tendon-sheath actuation mechanisms. The major advantage of tendon-sheath actuation mechanism is that it can be used to transfer force through a long, narrow and flexible route while taking up very little space. For this reason, the mechanism is widely used in robotic areas.

Tendon-sheath actuation mechanisms consist of hollow tubes, usually helical coils, and cables routing through the tubes. The cable serves as the tendon and the hollow tube acts as the sheath to guide the cable. When a tendon is pulled at one end, it moves inside the sheath and transmits the pulling force to the other end of the cable. In the design, two antagonistic SMA spring actuators were connected to a pulley through the tendon-sheath mechanism for each joint. The pulley rotates in different directions while the corresponding SMA spring is actuated. Since each SMA spring can be controlled independently, each joint could also be moved back and forth independently. The proposed actuation mechanism is shown schematically in figure 5.2.

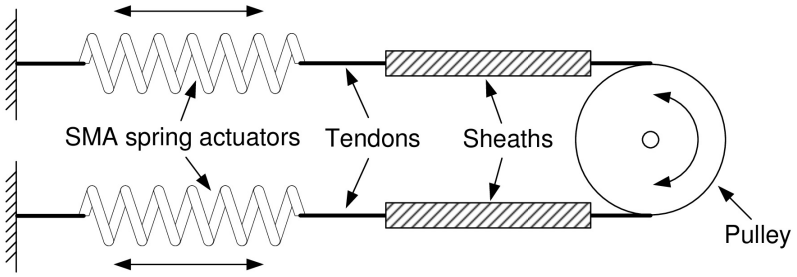

Figure 5.2: The tendon-sheath actuation mechanism with antagonistic SMA spring actuators for a joint of MINIR.

The design of the latest prototype of MINIR was modified based on the features of the previous design discussed in section 5.1.1 and is shown schematically in figure 5.3. The robot consisted of a tip link, a base link, three cylindrical links and four revolute

joints. The detailed engineering drawings of each part of the robot can be found in appendix A.2. The electrocautery tips are also embedded to the tip link as shown in the figure. All components of the robot were made of plastic, except the electrocautery tips, to ensure its MRI compatibility and the four revolute joints were placed orthogonally to have the required out-of-plane motion capability. The robot was hollow and allowed suction tubes and electrocautery wiring to be routed through the inside hollow core of the robot. Each cable was routed within a flexible tube and the tube was used to guide the cable through a non-straight path. The tubes were more rigid than the cables and acted as a kinematical decoupling of the joints. The robot was 63.5 mm long and the largest diameter was 11.5 mm. Each joint had an independent single degree of freedom controlled by a pair of antagonistic SMA spring actuators and the motion range of each joint was designed to be $\pm 60^{\circ}$.

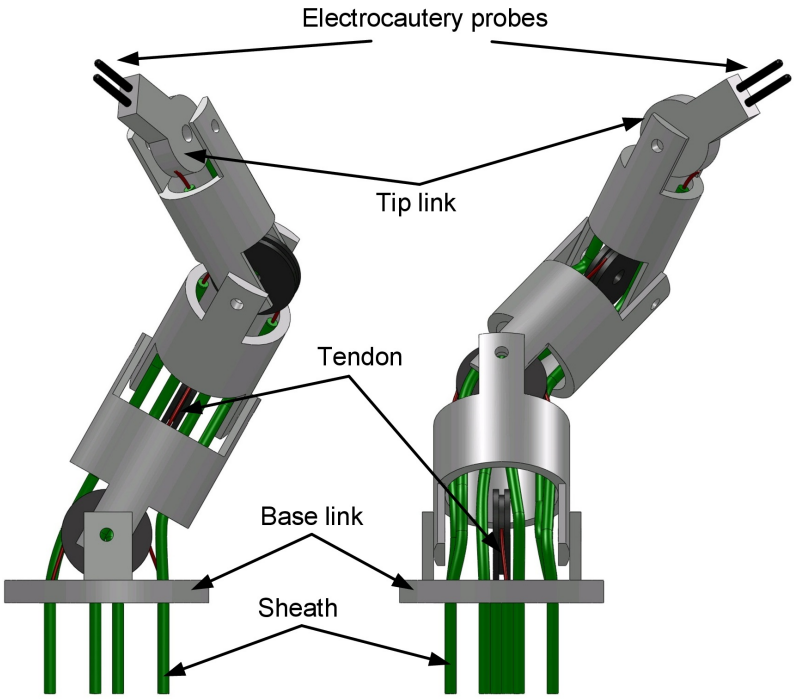

Figure 5.3: Schematic of the third generation of MINIR.

SMA is MRI compatible, however, in our application, the electric current used for resistive heating may cause noise in MR images and image distortion as discussed in section 4.5.8. In this design, we removed SMA actuators from the robot body. Instead, we used SMA spring actuators and tendon-sheath mechanisms to design the new actuation mechanism so that the actuators can be placed away from the robot body, outside the imagining region of the MRI scanner, and outside the patient's brain. This design not only minimized the noise in MR images but also prevented the damage to healthy brain tissue caused by the heat generated by the electric current passing through the SMA actuators. The envisioned system of MINIR is shown in figure 5.4 and the electrocautery and suction systems are also shown in the figure.

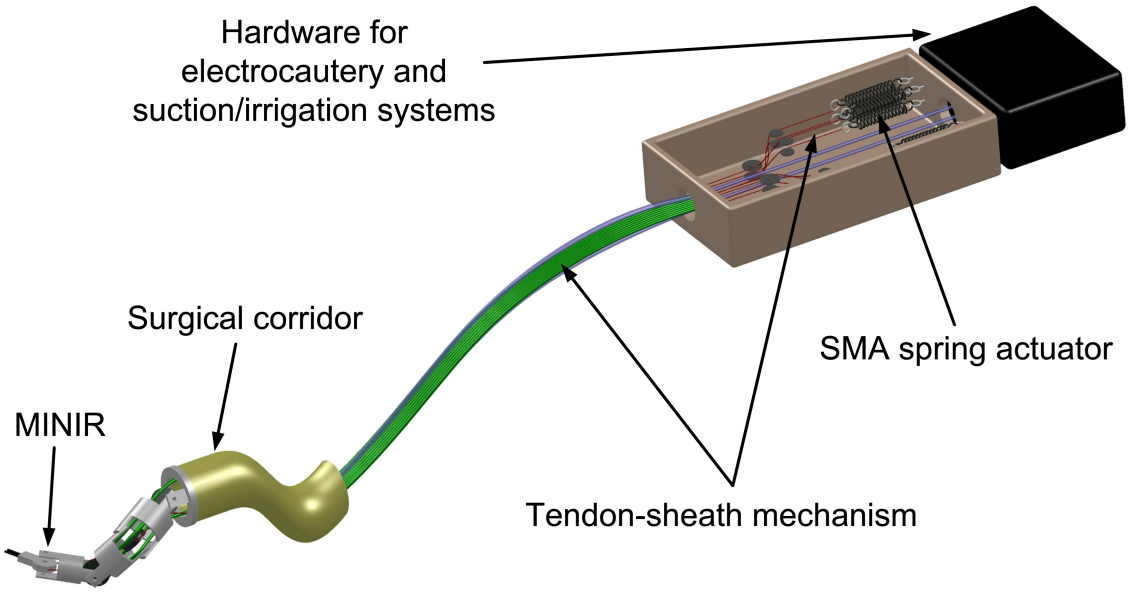

Figure 5.4: Schematic of the envisioned system of MINIR.

5.2 Modeling of SMA Spring Actuators

5.2.1 Constitutive Model of SMA under Pure Shear Stress

We continued to use temperature feedback to control the SMA spring actuators as the backup control scheme in this prototype, therefore, we had to develop a model that can describe the relationships of temperature and recovery length of the SMA spring. The details of the tensile constitutive model of SMAs have been explained in chapter 3. Based on the tensile model, Tobushi and Tanaka [97] further used similar equations to describe SMA behavior under pure torsional load. Considering there is a pure shear stress in the cross-section of a SMA wire of a spring, the general relation between shear stress, τ, and shear strain, γ, can be expressed as:

$$\dot{\tau} = G\dot{\gamma} + \frac{\Omega}{\sqrt{3}}\dot{\xi} + \frac{\Theta}{\sqrt{3}}\dot{T} \tag{5.1}$$

where G, Θ, T, Ω and ξ represent shear modulus, thermal expansion coefficient, temperature, phase transformation coefficient and martensite volume fraction of SMAs, respectively. In this model, strain, temperature, and martensite volume fraction are assumed to be independent state variables. Thus, the constitutive equation can also be written as [71]:

$$\tau - \tau_0 = G(\gamma - \gamma_0) + \frac{\Omega}{\sqrt{3}}(\xi - \xi_0) + \frac{\Theta}{\sqrt{3}}(T - T_0) \tag{5.2}$$

where τ_0, γ_0, T_0 and ξ_0 are initial conditions of the SMA. This equation shows that the shear stress consists of three parts: mechanical stress, thermal expansion stress and phase

transformation stress. A major drawback of Tanaka's [97] and Liang and Rogers' [71] constitutive models of SMA is that they do not capture the stress-induced detwinning of the martensite phase. They assumed martensite volume fraction only changes with temperature. However, if a SMA is initially stress free, strain free, in 100% martensite phase, *i.e.*, $\tau_0 = 0$, $\gamma_0 = 0$, $\xi_0 = 1$ and stretched by γ at a constant temperature, *i.e.*, $T = T_0$, $\xi = 1$, equation 5.2 yields the expression:

$$\tau = G\gamma \tag{5.3}$$

Equation 5.3 is a purely linear elastic stress-strain relation and cannot represent the non-linear behavior of SMAs as shown in figure 3.2. Brinson [74] addressed this issue by separating the martensite volume fraction into two parts and defined it as:

$$\xi = \xi_s + \xi_t \tag{5.4}$$

where ξ_t represents the temperature-induced martensite volume fraction and ξ_s denotes the stress-induced martensite volume fraction. With this definition, the constitutive model of SMAs can be written as:

$$\tau - \tau_0 = G(\gamma - \gamma_0) + \frac{\Omega_s}{\sqrt{3}}(\xi_s - \xi_{s0}) + \frac{\Omega_t}{\sqrt{3}}(\xi_t - \xi_{t0}) + \Theta(T - T_0) \tag{5.5}$$

To determine the phase transformation coefficients Ω_s and Ω_t, we first let the SMA be initially stress free, strain free, in 100% austenite phase , *i.e.*, $\tau_0 = 0$, $\gamma_0 = 0$, $\xi_{s0} = 0$, $\xi_{t0} = 0$ and then deformed by γ_L at a constant temperature, *i.e.*, $T = T_0$. As a result, the

material starts transforming from the 100% austenite phase to the 100% stress-induced martensite phase, *i.e.*, $\xi_s = 1$, $\xi_t = 0$, $\tau = 0$, $\gamma = \gamma_L$. Applying the conditions to equation 5.5, we get:

$$\Omega_s = -\sqrt{3}\gamma_L G \tag{5.6}$$

Consider another case where the SMA is at a low temperature, *i.e.*, $T < A_s$ and in 100% undeformed martensite phase, *i.e.*, $\xi_{t0} = 1$, $\xi_{s0} = 0$, $\tau_0 = 0$, $\gamma_0 = 0$, and deformed by γ_L at a constant temperature, *i.e.*, $T = T_0$, $\xi_s = 1$, $\xi_t = 0$, $\tau = 0$, $\gamma = \gamma_L$. Applying the conditions to equation 5.5, we get:

$$\Omega_t \equiv 0 \tag{5.7}$$

Thus, the constitutive model of the SMA in pure shear condition, *i.e.* equation 5.5, becomes:

$$\tau - \tau_0 = G(\gamma - \gamma_0) - \gamma_L G(\xi_s - \xi_{s0}) + \Theta(T - T_0) \tag{5.8}$$

Applying the conditions of the 100% un-deformed martensite phase at a constant temperature , *i.e.*, $\tau_0 = 0$, $\gamma_0 = 0$, $\xi_{s0} = 0$, $T = T_0$ to equation 5.8 yields:

$$\tau = G\gamma - \gamma_L G\xi_s \tag{5.9}$$

Comparing equation 5.9 with equation 5.3, it is clear that Brinson's model can accommodate the nonlinear stress-strain behavior of the SMA. In Brinson's model, two parameters were defined to describe the start and end points of stress-induced martensite transformation. τ_s^{cr} is the critical stress for the start of transformation and τ_f^{cr} is the critical stress at the end of transformation. These values were approximated from the stress-strain curve

shown in figure 3.2, where the SMA was initially in 100% undeformed martensite phase. The stress-induced martensite volume fraction during detwinning , *i.e.*, $T < M_f$ and $\tau_s^{cr} < \tau < \tau_f^{cr}$ is defined as [74, 98]:

$$\xi_s = \frac{1-\xi_{s0}}{2} cos\left[\frac{\pi}{\tau_s^{cr}-\tau_f^{cr}}(\tau-\tau_f^{cr})\right] + \frac{1+\xi_{s0}}{2} \tag{5.10}$$

When the SMA transforms from martensite phase to austenite phase, *i.e.*, heating transformation, the martensite volume fraction is defined as [74]:

$$\xi = \frac{\xi_0}{2}\left\{cos\left[a_A\left(T - A_s - \frac{\sqrt{3}\tau}{C_A}\right)\right] + 1\right\} \tag{5.11}$$

In equation 5.8, shear modulus, G, of SMAs is a function of the martensite volume fraction based on Tanaka's assumption [97] and it is expressed as:

$$G(\xi) = G_A + \xi(G_M - G_A) \tag{5.12}$$

5.2.2 Force-Displacement Relationship of SMA Springs

To derive the theoretical model that describes the force behavior of a SMA spring, we first assumed that there was pure shear in the cross-section of a SMA wire of a spring when the spring is under tension. Since the analysis of conventional springs is standard and available in most mechanical design textbooks, such as [99], only some important concepts will be mentioned here for continuity. The displacement of a spring can be computed from the deformation of an element in the spring as shown in figure 5.5. The

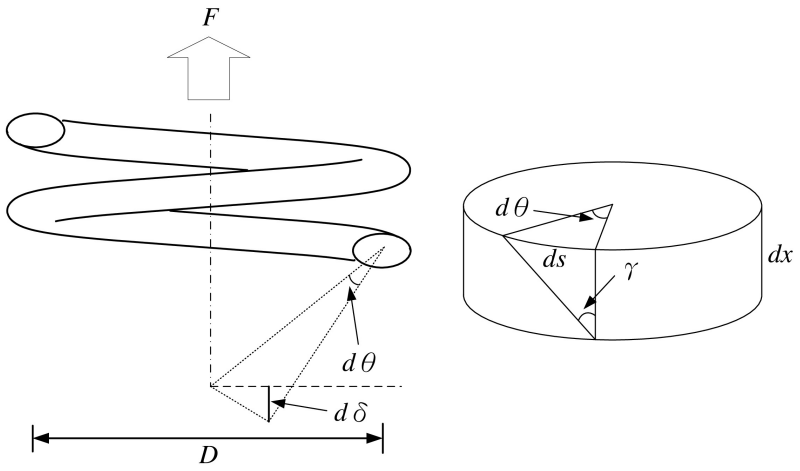

Figure 5.5: Schematic of a spring and an element of the spring.

length of the element is dx and the diameter of the spring wire is d. An external force, F, acting on the spring results in a pure shear stress, τ, in the element. The shear stress causes a rotation of $d\theta$ in the element and the shear strain, γ, can be defined as:

$$\gamma = \frac{ds}{dx} \tag{5.13}$$

Based on the geometry of the element, we have:

$$ds = \gamma dx = \frac{d}{2} d\theta \tag{5.14}$$

In the figure, we can see that the rotation, $d\theta$, will contribute towards spring deflection in the vertical direction by an amount of $d\delta$. Based on the geometry of a spring, the vertical displacement, $d\delta$, is given as:

$$d\delta = \frac{D}{2} d\theta = \frac{D}{2} \frac{2\gamma}{d} dx = \frac{D\gamma}{d} dx \tag{5.15}$$

where D is the diameter of the spring. The total deflection of the spring, δ, can be obtained by integrating the above expression for entire length of the spring and is given by:

$$\delta = \int d\delta = \frac{D\gamma}{d} \int_0^{\pi DN} dx = \frac{\pi D^2 N}{d}\gamma \tag{5.16}$$

where N is the total number of active coils in the spring. According to [99], the shear stress, τ, in the spring caused by external force, F, is given by:

$$\tau = \frac{8FD}{\pi d^3} + \frac{4F}{\pi d^2} = k_s \frac{8FD}{\pi d^3} \tag{5.17}$$

where k_s is the Wahl correction factor which accounts for both curvature effect and shear stress correction factor and is expressed as:

$$k_s = \frac{4c-1}{4c-4} + \frac{0.615}{c} \tag{5.18}$$

where c is spring index (c = D/d). With the above discussed equations, the thermomechanical behavior of a SMA spring can be modeled by substituting equation 5.16 and equation 5.17 into equation 5.8. Assume the stress from thermal expansion is small compared to the other two terms in equation 5.8, equation 5.8 can then be written as:

$$C_1(F - F_0) = C_2 G(\xi)(\delta - \delta_0) - C_2 \delta_L G(\xi)(\xi - \xi_0) \tag{5.19}$$

where C_1 and C_2 are constants and defined as:

$$C_1 = 8\frac{k_s D}{\pi d^3} \qquad C_2 = \frac{d}{\pi D^2 N} \tag{5.20}$$

Equation 5.19 can be used to describe the force-displacement relationship ,*i.e*, ($F \sim \delta$) of a SMA spring.

5.2.3 Force Modeling of SMA Springs

Consider a SMA spring attached to a force sensor at one end and fixed at the other end, as shown in figure 5.6. Assume that initial force and initial displacement in the spring are F_0 and δ_0 when the spring is at room temperature, T_0. As the spring is heated above the transformation temperature, it starts to contract and causes the recovery force in the spring to increase. Assume the recovery force increases from F_0 to F and the displacement changes from δ_0 to δ. We assumed that the stretch in the tendon is small and hence negligible in this thesis. The recovery force, spring displacement and temperature of the spring are related according to equation 5.19. Since the two ends of the spring are fixed, the displacement of the spring will not change ($\delta = \delta_0$) when the spring is heated. As a result, equation 5.19 can be re-written as:

$$C_1(F - F_0) = -C_2\delta_L G(\xi)(\xi - \xi_0) \tag{5.21}$$

According to equation 5.11, ξ is dependent on the shear stress, τ. Therefore in equation 5.21, the recovery force, F, can be solved numerically using Newton-Raphson's method

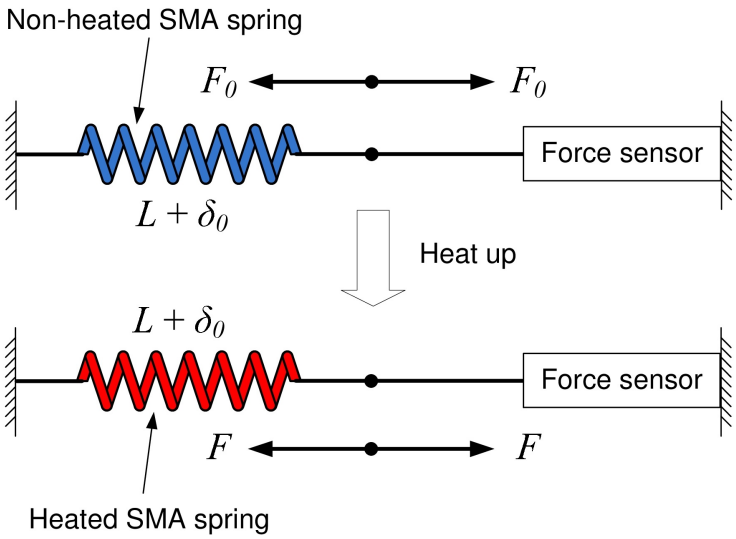

Figure 5.6: Schematic for the recovery force analysis of a SMA spring.

which is expressed as:

$$F_{new} = F_{old} - \frac{f(F_{old})}{f'(F_{old})} \tag{5.22}$$

where $f(F)$ and $f'(F)$ are obtained as

$$\begin{aligned} f(F) &= C_1(F - F_0) + C_2\delta_L G(\xi)(\xi - \xi_0) \\ f'(F) &= C_1 + C_2\delta_L(\xi - \xi_0)\frac{\partial G(\xi)}{\partial F} + C_2\delta_L G(\xi)\frac{\partial \xi}{\partial F} \end{aligned} \tag{5.23}$$

and

$$\begin{aligned} \frac{\partial G(\xi)}{\partial F} &= (G_A - G_M)\frac{\partial \xi}{\partial F} \\ \frac{\partial \xi}{\partial F} &= \frac{\sqrt{3}\xi_0 C_1 a_A}{2C_A} sin\left[a_A\left(T - A_s - \frac{\sqrt{3}C_1 F}{C_A}\right)\right] \end{aligned} \tag{5.24}$$

Equation 5.22 and equation 5.23 can be used to compute the recovery force of a SMA spring at different temperatures and displacement. Since the desired motion range of

each joint of MINIR was $\pm 60^{\circ}$ and the diameter of the pulley used for MINIR was 7 mm, the required displacement of each SMA spring actuator was ± 5 mm. Therefore, we used 0 mm to 10 mm as the testing range of the displacement in the SMA recovery force experiment. Note that each SMA spring actuator will be pre-stretched to 5 mm before conducting the experiment, therefore, the ± 5 mm motion range results in a 0 mm to 10 mm displacement.

5.2.4 Modeling of Antagonistic SMA Springs

Consider two SMA springs with original length L placed antagonistically, as shown in figure 5.7, pre-stretched by δ_0 and then recovered by δ_r when one of them was heated above the transformation temperature.

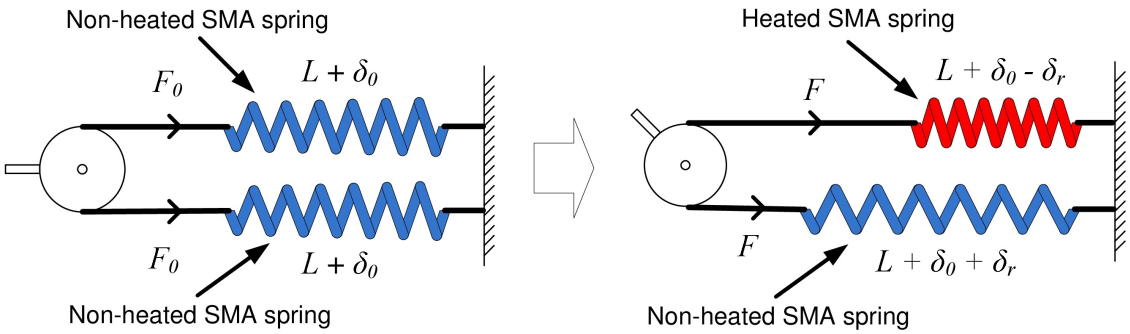

Figure 5.7: Modeling of the antagonistic SMA springs

For the non-heated SMA spring, there is no temperature induced martensite phase ($\xi_t = 0$). Therefore, $\xi = \xi_s$ since $\xi = \xi_s + \xi_t$. As a result, the thermomechanical relation of the non-heated SMA spring can be obtained from equation 5.19 and expressed as:

$$C_1(F - F_0) = C_2 G_M(\delta - \delta_0) - C_2 \delta_L G_M(\xi_s - \xi_{s0}) \tag{5.25}$$

where G_M is the martensite shear modulus of the SMA spring. Based on Brinson's model [74], when the shear stress in the SMA spring is smaller than τ_s^{cr}, there is no stress induce martensite phase in the SMA ($\xi_s = \xi_{s0} = 0$) and hence equation 5.25 can be written as:

$$C_1(F - F_0) = C_2 G_M(\delta - \delta_0) \tag{5.26}$$

Therefore, the recovery displacement, δ_r, can be expressed as:

$$\delta_r = \delta - \delta_0 = \frac{C_1(F - F_0)}{C_2 G_M} \tag{5.27}$$

Equation 5.27 indicates that the non-heated SMA spring serves as a normal extensional spring with a spring constant, k, equals:

$$k = \frac{C_2}{C_1} G_M \tag{5.28}$$

For the heated SMA spring, it recovered by δ_r upon heating so that $\delta - \delta_0 = -\delta_r$. Combining equation 5.19 and equation 5.27, we get

$$C_1(F - F_0) = C_2 G(\xi) \left(-\frac{F - F_0}{k} \right) - C_2 \delta_L G(\xi)(\xi - \xi_0) \tag{5.29}$$

Since ξ is a cosine function of spring force, F, equation 5.29 can be solved numerically when T is known using Newton-Raphson's method, which is given by:

$$F_{new} = F_{old} - \frac{f(F_{old})}{f'(F_{old})} \tag{5.30}$$

where

$$f(F) = C_1(F - F_0) + C_2\frac{F - F_0}{k}G(\xi) + C_2\delta_L(\xi - 1)G(\xi)$$

$$f'(F) = C_1 + C_2\frac{F - F_0}{k}\frac{\partial G(\xi)}{\partial F} + \frac{C_2}{k}G(\xi) + C_2\delta_L(\xi - 1)\frac{\partial G(\xi)}{\partial F} + C_2\delta_L G(\xi)\frac{\partial \xi}{\partial F} \quad (5.31)$$

and

$$\frac{\partial G(\xi)}{\partial F} = (G_M - G_A)\frac{\partial \xi}{\partial F}$$

$$\frac{\partial \xi}{\partial F} = \frac{\sqrt{3}C_1\xi_0 a_A}{2C_A} sin\left[a_A\left(T - A_s - \frac{\sqrt{3}C_1 F}{C_A}\right)\right] \quad (5.32)$$

Equation 5.29 describes the force-temperature behavior of a pair of antagonistic SMA springs which is used as the governing equation to control the SMA springs using temperature feedback described in this chapter. To conclude, we can calculate the recovery force, F, in the SMA spring actuator using equation 5.29 if temperature, T, is known. We can then use equation 5.27 to compute the recovery length of the SMA spring and hence the joint motion of the robot.

5.3 SMA Spring Characterization

The goal of this chapter is to experimentally determine the material constants such as shear moduli, transformation temperatures, critical shear stresses and maximum recoverable shear strain of the SMA spring. These parameters are essential for the model that we derived in section 5.2. The parameters are dependent on the thermal and mechanical history of the material such as the composition of the material, annealing temperature, annealing time and heat treatment. Therefore, it is necessary for us to characterize the

SMA spring before using it.

5.3.1 Characterization of a Single SMA spring

The first experiment we did was the force-elongation test of a single SMA spring. The goal of this experiment was to determine the shear moduli, critical shear stresses and maximum recoverable shear strain of the SMA spring. In this experiment, we stretched the SMA spring at two different temperatures , *i.e.*, $T < A_s$ and $T > A_f$. We developed a PC-based system to conduct the experiment and the experimental setup is shown in figure 5.8. The system consists a DC motor, a force sensor, a thermocouple, a DC power supply, a PWM controller and an AD/DA data acquisition card. The motor is controlled by the PC to stretch the SMA spring to desired displacement and is equipped with a rotary encoder used for position feedback. The force sensor is used to measure the recovery force generated by the spring. A T-type thermocouple is used along with thermally conductive paste to measure the spring temperature. Thermally conductive paste has high thermal conductivity and high resistance, which is used to ensure heat transfer while preventing electric noises. The thermocouple was attached at the center of the spring and we assumed that the electric resistance of the SMA spring was constant throughout the entire spring. Thus, we could say that the temperature distribution was homogeneous in the SMA spring. A DC power supply and resistive heating were used to heat up the SMA spring. A PWM-PI temperature controller was used to control the temperature in the SMA spring and the details of the temperature control scheme has been discussed in chapter 4. All experimental data and control signals were transferred to a PC through a data acquisition card which

has sixteen 16-bit A/D channels and four 14-bit D/A channels with 15k Hz sampling rate. The entire experimental setup except the PC was put inside a chamber to ensure stable measurements of temperature. The experimental results are shown in figure 5.9. From

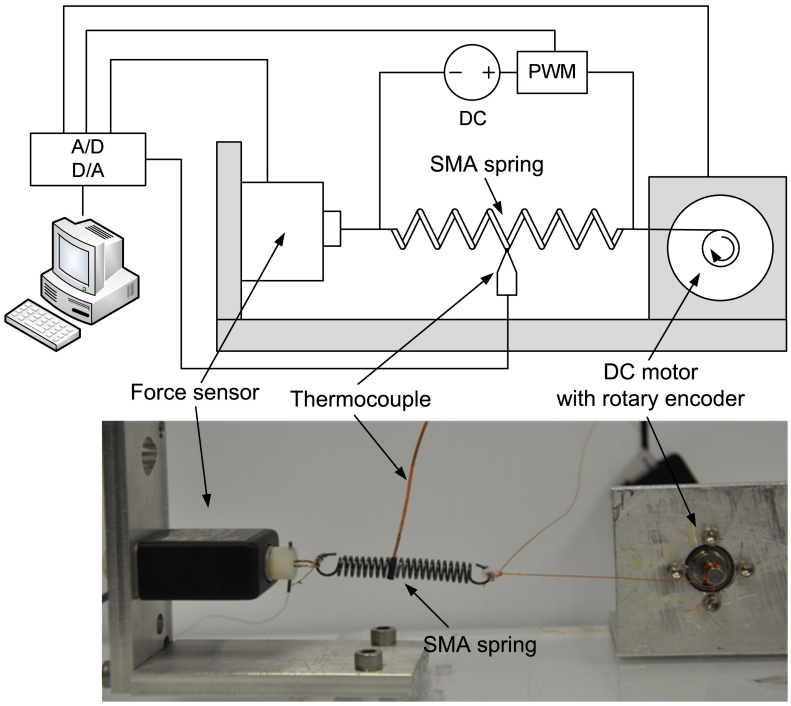

Figure 5.8: Experimental setup for force-elongation test.

the experimental results when $T < A_s$, the spring constant, k, can be determined from the linear region of the curve and the martensite shear modulus, G_M, can then be computed using equation 5.28. The austenite shear modulus, G_A, can be determined using the same way based on the experimental results when $T > A_f$. The critical shear stress, τ_s^{cr}, was determined by finding the maximum force of the linear region of the curve when $T < A_s$ and then computed using equation 5.20. Another critical stress, τ_f^{cr}, and the maximum recoverable shear strain, γ_L, were approximated by fitting the experimental curve when $T < A_s$ using equation 5.10 and equation 5.25 since we did not stretch the SMA spring to its maximum length.

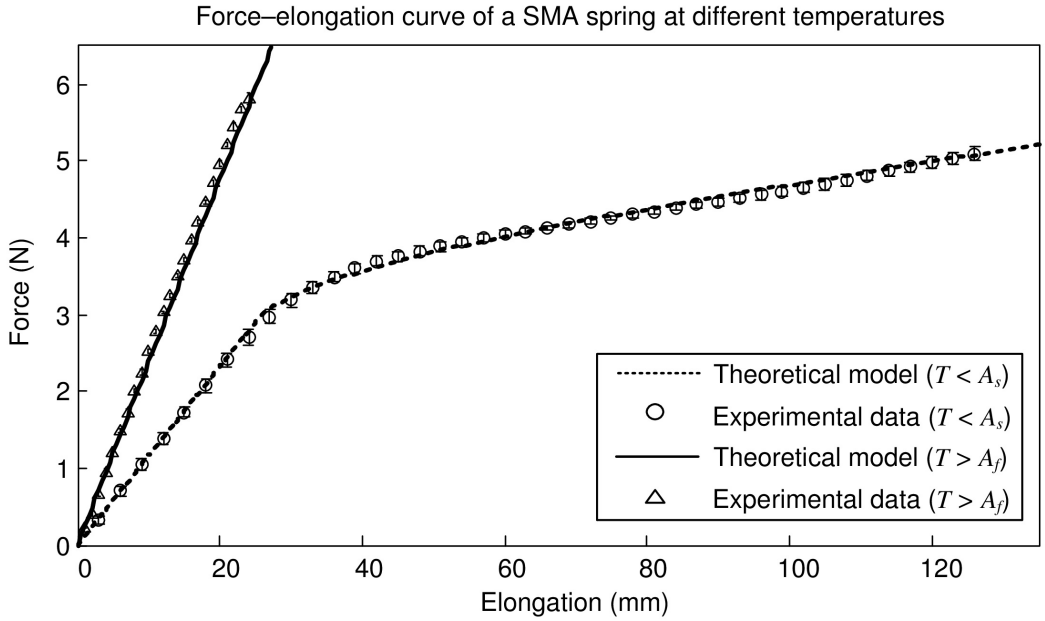

Figure 5.9: Experimental results of the force-elongation curve of a SMA spring at different temperatures.

The theoretical curves in figure 5.9 were computed using equation 5.10, equation 5.11, equation 5.19 and equation 5.25 with the material parameters listed in Table 6.1. From the results, we also found that when the elongation of the SMA spring was less than 25 mm, the SMA spring behaved like a regular extensional spring and it fully recovered when released after stretching. Since we plan to use the non-heated SMA spring as a bias spring in the antagonistic setup, the initial stretch, δ_0, of the SMA spring should be less than 12.5 mm to ensure its full recovery when released. Therefore, the initial stretch of the SMA springs were set to 12 mm in all the experiments throughout this chapter.

In the second experiment, we conducted free recovery tests to find the transformation temperatures of the SMA spring. The experimental setup was similar to the one that we used for the previous experiment as shown in figure 5.8 but the DC motor was replaced with a rotary encoder. The SMA spring was stretched by 12 mm before the experiment

Table 5.1: Material parameters determined experimentally

Shear moduli	**Transformation temperatures**	**Critical shear stresses**	**Maximum recoverable shear strain**
$G_M = 15.12$ GPa	$A_s = 28$ °C	$\tau_s^{cr} = 120$ MPa	$\gamma_L = 0.05$
$G_A = 31.84$ GPa	$A_f = 39$ °C	$\tau_f^{cr} = 290$ MPa	

started. During the experiment, the temperature and recovered length of the SMA spring were measured by the thermocouple and the rotary encoder. The SMA spring started to recover when the temperature was higher than the austenite start temperature, A_s, and recovered to its original length when the temperature was higher than the austenite finish temperature, A_f. The experimental results are shown in figure 5.10 and the transformation temperatures, A_s and A_f, were determined to be 28 °C and 39 °C respectively. The theoretical model in the figure was computed using equations 5.11 and 5.19 with the parameters listed in table 6.1.

5.3.2 Characterization of Antagonistic SMA springs

After obtaining all necessary material parameters of the SMA spring, we need to further verify the validity of the antagonistic model that we developed in section 5.2.4. The experimental setup is shown in figure 5.11 and the experimental results are shown in figure 5.12. The theoretical model in figure 5.12 was computed using equation 5.29 with the material parameters listed in table 6.1.

The experimental results fit the theoretical model well, which proved that the re-

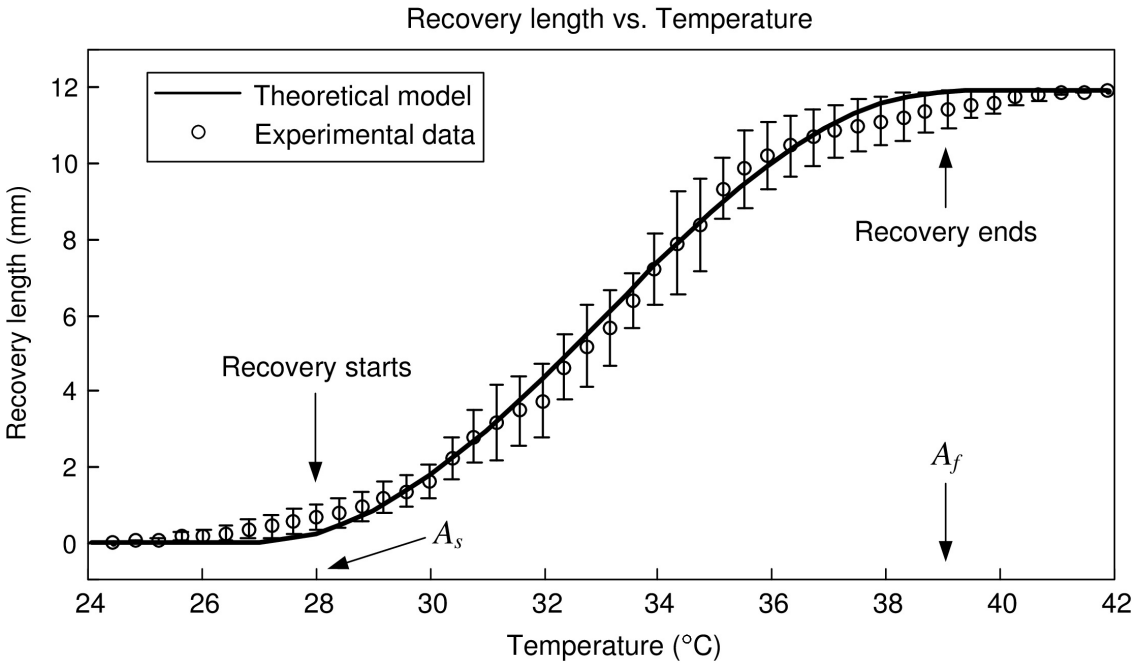

Figure 5.10: Experimental results of the free recvery test.

covery length of the actuated SMA spring can be computed using equation 5.29 if the temperature in the actuated SMA spring is known. In other words, we can control the length of the SMA spring using temperature feedback and hence control the joint motion of the robot. The SMA spring recovered by 8 mm when heated to 40 °C while the initial elongation was 12 mm. The maximum motion range of each joint of MINIR was designed to be $\pm 60°$. Since the diameter of the pulley used in the robot was 7 mm, the 8 mm recovery length in the SMA spring was sufficient to move the joint to its maximum bending angle.

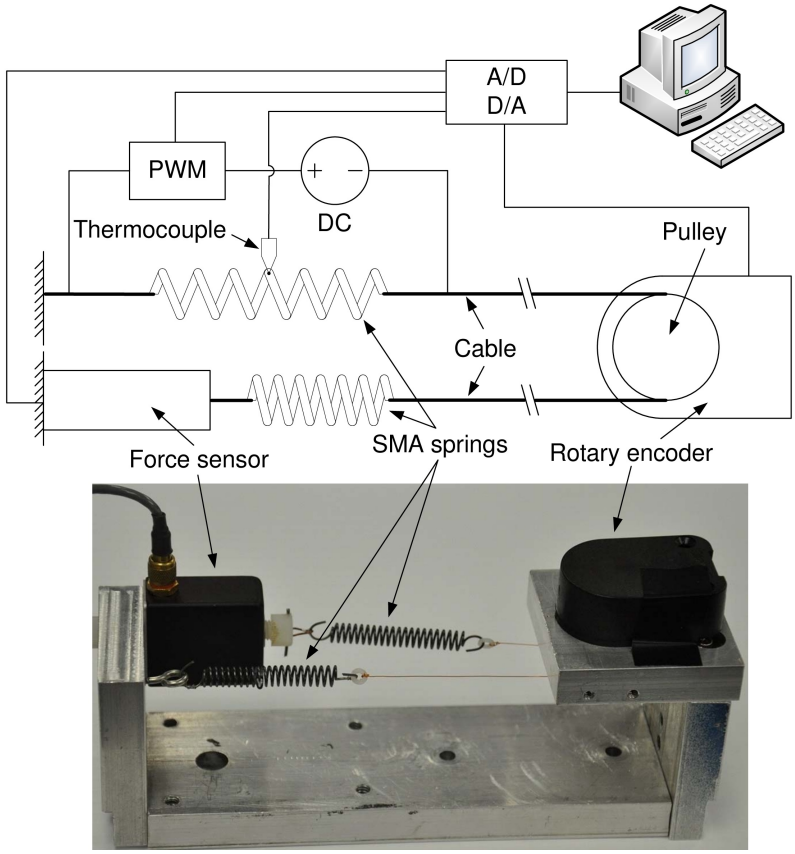

Figure 5.11: Experimental setup for antagonistic SMA springs test.

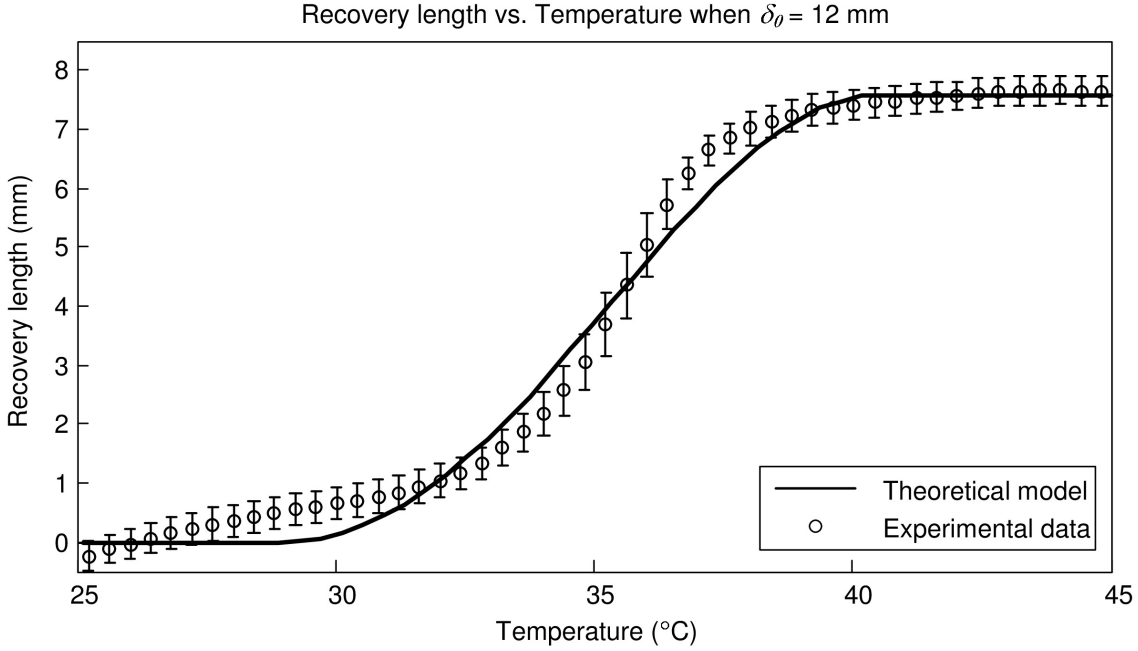

Figure 5.12: Experimental results of the antagonistic SMA springs chracterization.

5.4 Results

5.4.1 Motion Test

The overall system of MINIR with SMA spring actuators are shown in figure 5.13. The robot was 65 mm in length and the maximum diameter was 11 mm. The goal of this experiment was to evaluate if the tendon-sheath mechanism and the SMA spring actuators could be used to actuate various joints of MINIR to move in orthogonal directions and if each joint could be controlled independently. Therefore, we only used four SMA springs to actuate two joints of MINIR.

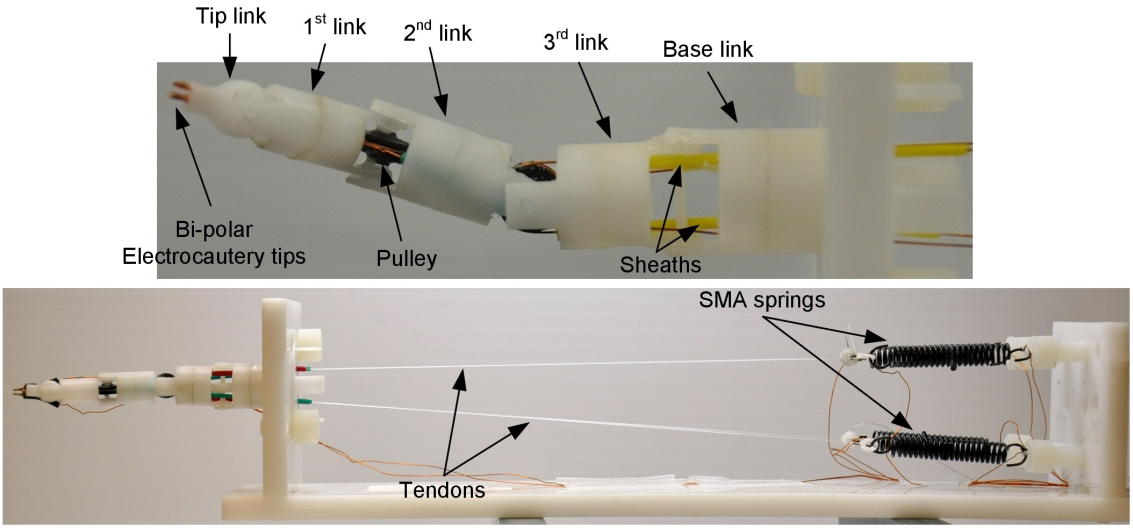

Figure 5.13: Overall system of MINIR with a close-up view.

Figure 5.14 shows the robot in three different configurations and the two joints can move in orthogonal directions. The experimental results also proved that the two joints of MINIR can be controlled independently. The first link was able to move to its maximum bending angle, $\pm 60^{\circ}$, while the second link can only be moved to $\pm 45^{\circ}$ due to the resistant force imposed by the sheaths.

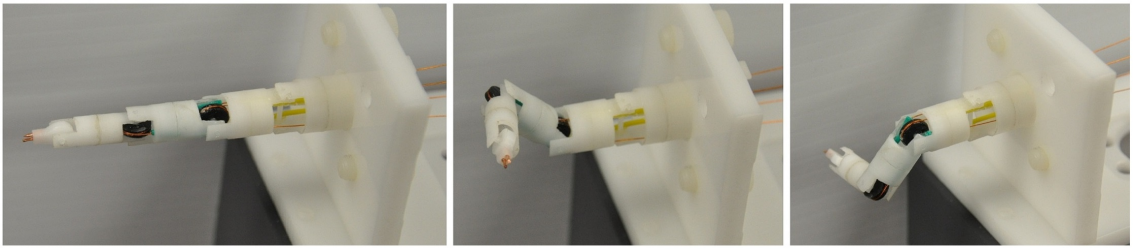

Figure 5.14: Motion test of MINIR when actuated by antagonistic SMA spring actuators.

5.4.2 Force Test

The goal of this experiment was to estimate the joint force of MINIR at different bending angles. The SMA spring was stretched to 12 mm and 8.3 mm in two different trials by a DC motor as shown in figure 5.8. Note that 12 mm is the initial stretch of the SMA springs used in MINIR. Therefore, when the SMA spring is stretched to 12 mm, the bending angle of the MINIR joint is 0°. Similarly, when the SMA spring is stretched to 8.3 mm, the bending angle of the MINIR joint is 60° since the diameter of the pulley used in MINIR was 7 mm. The SMA spring was then heated to specific temperatures while the corresponding force readings were recorded.

The experimental results are shown in figure 5.15. In the figure, we can see that the SMA spring could generate 3.9 N and 2.5 N of force when the SMA spring was stretched to 12 mm and 8.3 mm respectively. Which means MINIR could generate up to 3.9 N of force when the joint was in a straight configuration and 2.5 N of force when the joint bent to 60°. Moreover, the results were repeatable and consistent with the theoretical model presented in section 5.2. This implies that the recovery force-temperature-displacement relation of a SMA spring is predictable using equation 5.19. Since the force behavior of a SMA spring is predictable, equation 5.19 can be used as a governing equation for

force control of the SMA spring. For example, if the displacement, δ, is measured, the temperature, T, can be used as a feedback signal to control the output force of the SMA spring. This is a very important observation since there are not many sensors that can be used in a MRI environment.

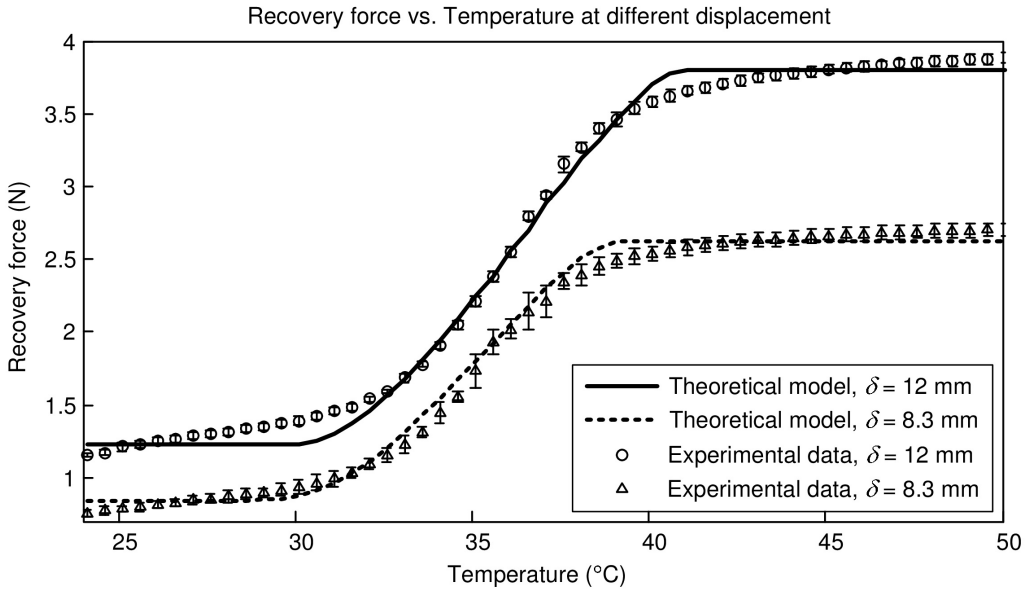

Figure 5.15: Experimental results of the recovery force of a SMA spring at different temperatures and displacement.

5.4.3 Test in Gelatin

To make sure the robot can move in a tightly enclosed environment, we tested it in a gelatin slab. The gelatin slab was used to simulate brain tissue. The electrocautery and suction systems were also integrated to the robot and tested in the gelatin to make sure that they were functioning as expected. The experimental results are shown in figure 5.16. The robot was inserted into the gelatin and the first link and second link were then actuated independently to move back and forth. The electrocautery and suction systems were activated when the robot was moving.

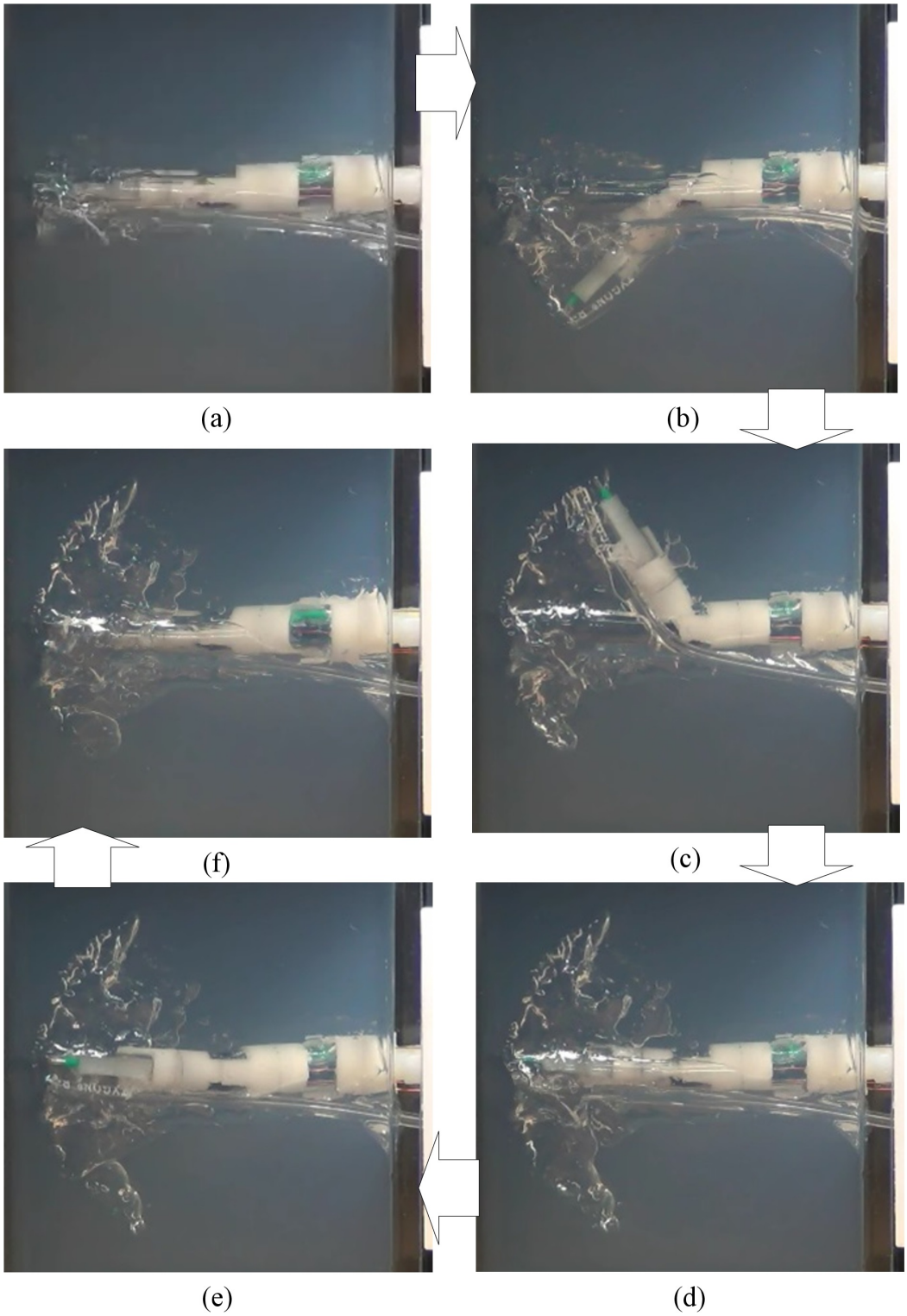

Figure 5.16: Test of the third generation of MINIR in gelatin.

The experimental results clearly demonstrated that the robot was functioning as expected. The robot could generate enough force to move in the gelatin and the two joints could be controlled to move back and forth independently. Moreover, the electrocautery and suction systems were able to electrocauterize the gelatin and sucked the melted gelatin liquid out creating voids in the gelatin.

5.4.4 MRI Compatibility Test

Since MINIR was desired to be operated in MRI scanners, we did a series of experiment to qualitatively and quantitatively evaluate the influence of MINIR in a MRI scanner. The experimental setup for the MRI compatibility experiment is shown in figure 5.17. We used gelatin to simulate brain tissue and the robot was inserted into the gelatin slab through a channel that was created in advance as seen in figure 5.17(a). The robot and gelatin were then be placed in a head coil at the center of a MRI scanner as shown in figure 5.17(b). The same experimental setup was used throughout the series of experiment. Figure 5.18 shows the gelatin slab as well as two MR images that show the channel we created in the gelatin for insertion of MINIR. The four slices indicated in figure 5.18(b) show the locations where we took the MR images in the following experiments and each slice is 2 mm apart.

The experiments include the following eights steps:

Step 1. Took high resolution MR images of the gelatin slab only

Step 2. Inserted MINIR into the gelatin slab and take high resolution MR images. Note that there was no any devices connected to MINIR

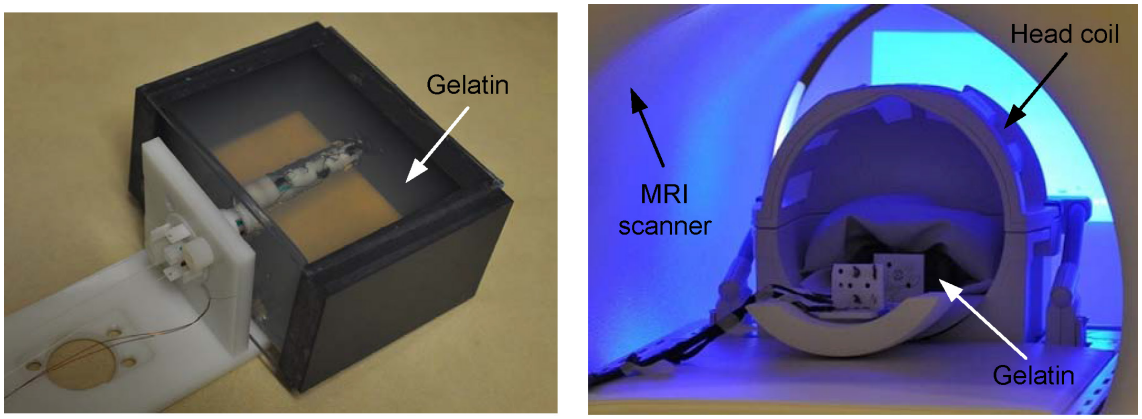

(a) (b)

Figure 5.17: Experimental setup for MRI compatibility test.

Step 3. Connected all required connections to MINIR and turned on all required devices for operating MINIR but MINIR was not actuated. Then took high resolution MR images

Step 4. Took dynamic MR images without actuating MINIR

Step 5. Took dynamic MR images while the fist link of MINIR was actuated to left following by actuating the second link down. The electrocautery was not used

Step 6. Took high resolution MR images after actuation

Step 7. Took dynamic MR images while the fist link of MINIR was actuated to right following by actuating the second link up and electrocautery was activated after actuation

Step 8. Took high resolution MR images after actuation

The MRI scanner was set to TE/TR = 97/10200 ms for high resolution images and TE/TR = 1.51/4.1 ms for dynamic images. The settings were kept the same for all above eight

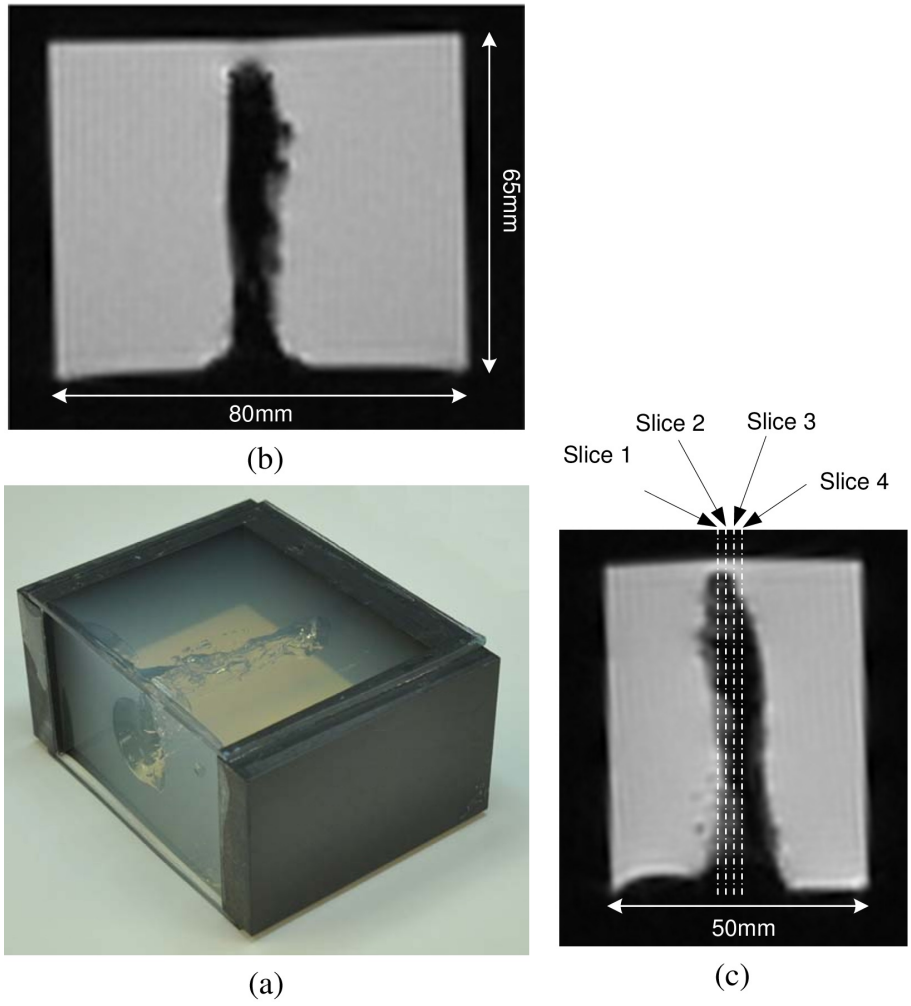

Figure 5.18: The (a) isometric view of the gelatin slab, (b) MR image of the top view and (c) side view of the gelatin.

scans.

In step 1, we took high resolution images of the gelatin slab itself. The images were shown in figure 5.19 and they were used as the ground truth for comparison in this series of experiment. The images were clear without any observable image distortion and the average SNR was computed to be 179.6.

For step 2, MINIR was inserted to the gelatin slab without any connections. This experiment was to evaluate the disturbance that the MINIR itself caused in the MR im-

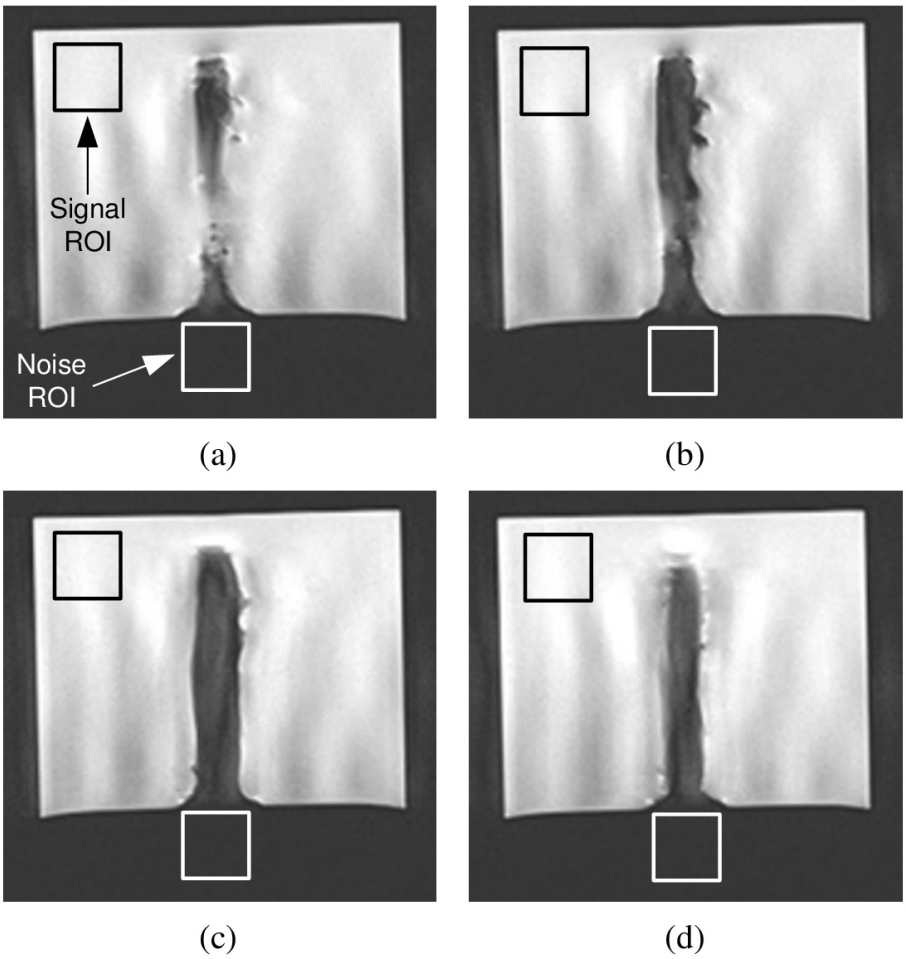

Figure 5.19: High resolution MR images of step 1: (a) slice 1, (b) slice 2, (c) slice 3, and (d) slice 4 of the gelatin slab.

ages. The results are shown in figure 5.20. The robot profile can be clearly seen and no observable distortion in the images. To quantify the noise caused by the robot itself in the images, the SNR was computed and compared with ground truth. The average SNR dropped to 158.1 after inserting the robot and it was a 12% drop compared with the SNR in step 1, *i.e.*, dropped from 179.6 to 158.1.

We then connected all required connections to MINIR and turned on all devices connected to it, such as electrocautery signal generator and power supply, in step 3. A high resolution scan was performed to evaluate the noise that the connections and de-

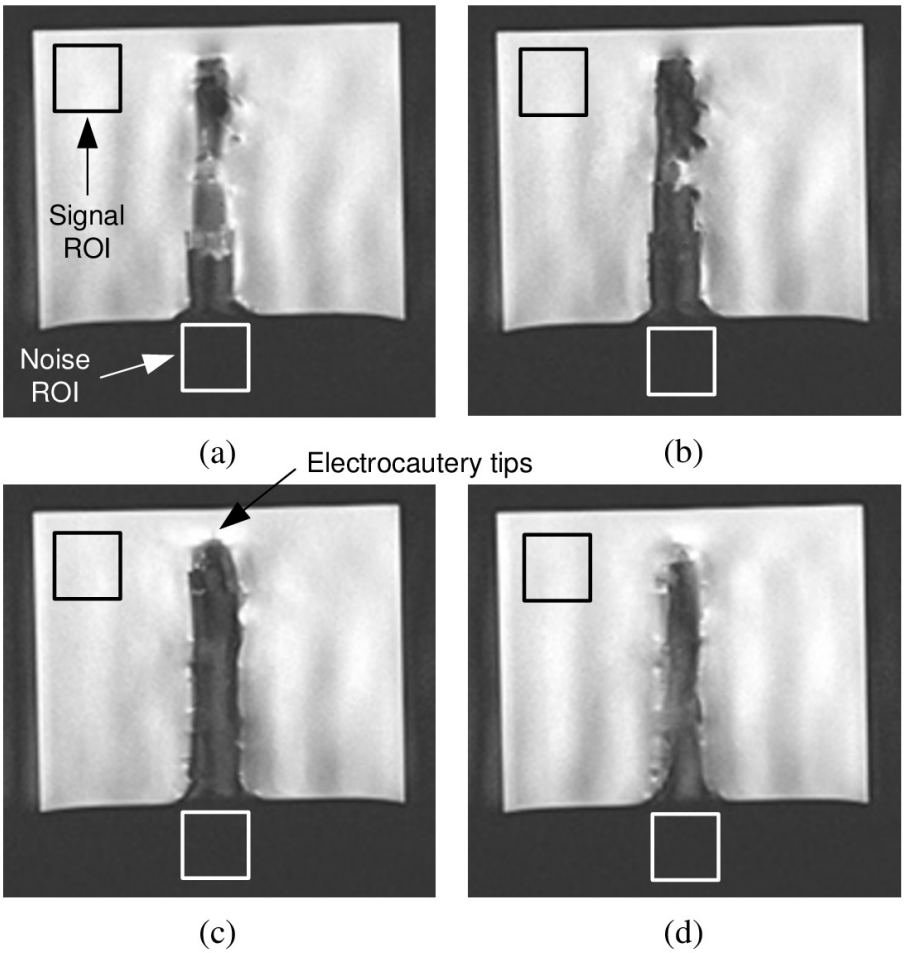

Figure 5.20: High resolution MR images of step 2: (a) slice 1, (b) slice 2, (c) slice 3, and (d) slice 4 of the gelatin slab with MINIR inside.

vices caused in the MR images. The MR images are shown in figure 5.21. Comparing figure 5.21 with figure 5.20, some image distortion was observed near the base link of MINIR. However, the distortion did not appear around the tip link of MINIR and electrocautery tips can still be clearly seen, *i.e.*, can be tracked by the image tracking algorithm, therefore, we believe the distortion is not significant. The average SNR was computer to be 152 which was 3.9% less than the SNR of step 2. This suggested that the connections and the devices did not cause significant noise in the MR images.

In step 4, we used the same setup as step 3 but a dynamic scanning sequence was

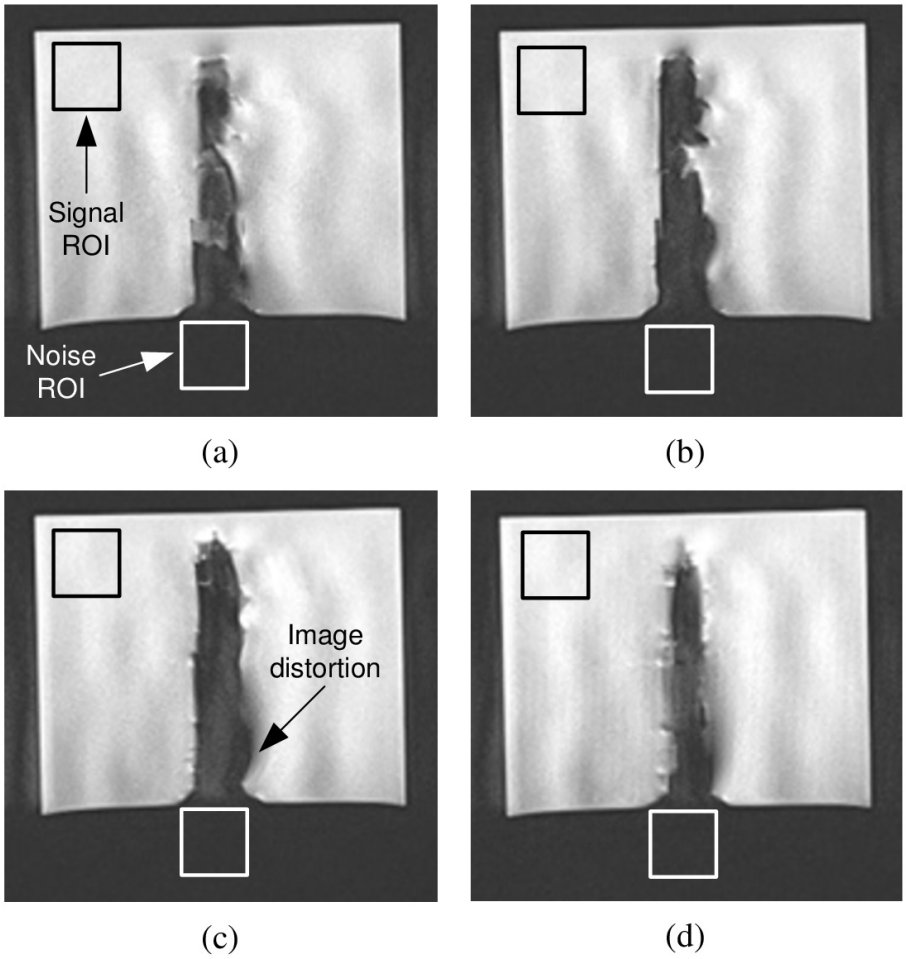

Figure 5.21: High resolution MR images of step 3: (a) slice 1, (b) slice 2, (c) slice 3, and (d) slice 4 of the gelatin slab and MINIR with all connections and devices power on.

used. In this dynamic scan, 200 images were taken continuously in 60 seconds. This experiment was used to qualitatively evaluate if there is any image distortion caused by the robot in dynamics scanning as well as quantitatively see how the SNR changes during scanning. The experimental results in this step were used as the ground truth for comparison with the dynamic MR images obtained later in step 5 and step 7. The MR images are shown in figure 5.22 and the SNR of each image is shown in figure 5.23. The MR images did not show any image distortion and the SNR did not change significantly during scanning. The average SNR of the 200 images was 29.7.

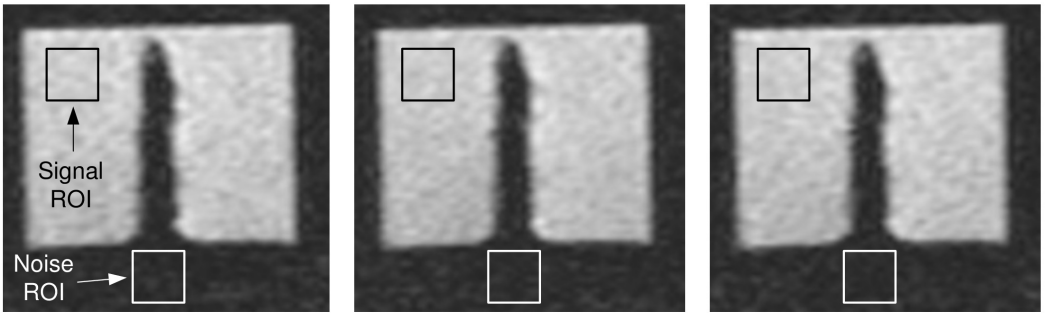

(a) (b) (c)

Figure 5.22: Dynamic MR images of step 4 at diferent time points.

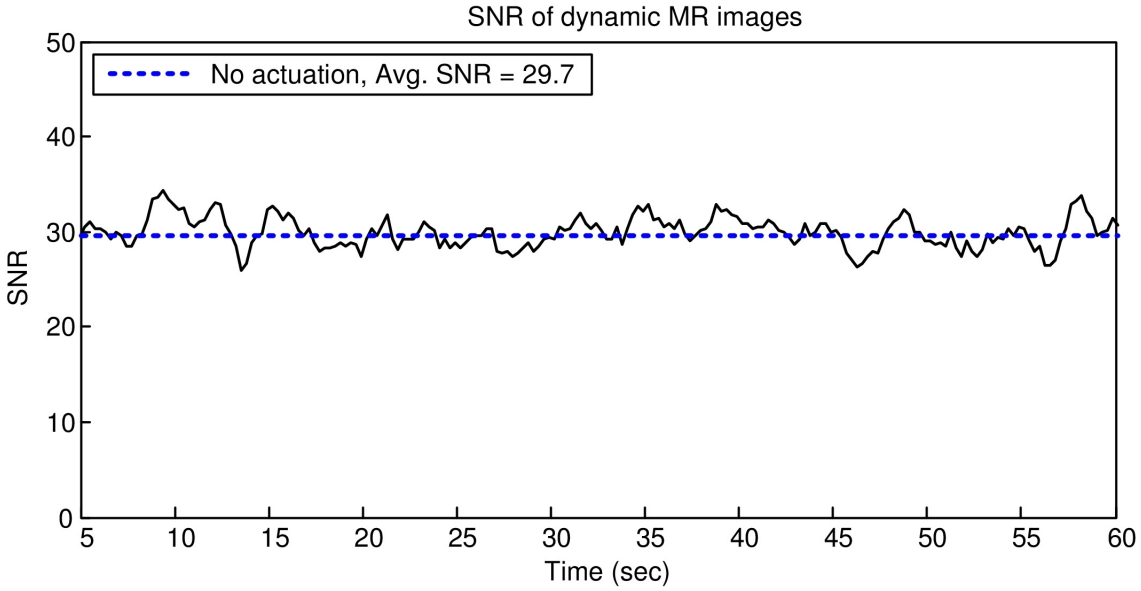

Figure 5.23: SNR of each image obtained in step 4.

In step 5, we actuated MINIR in the middle of scanning to evaluate image noise caused by the electric current used to actuate SMA spring actuators. The first link of MINIR was actuated at 10^{th} second to move to right for about 10 seconds and the second link was then actuated to move down for about 10 seconds. The MR images at different time points are shown in figure 5.24. The images show no significant image distortion and that the joints of MINIR were successfully actuated. It can be clearly seen that the first link of MINIR was actuated to right [(see figure 5.24(b)] and then disappeared from the

image because it moved out of the image plane [(see figure 5.24(c)]. This result demonstrated that MINIR could be operated under continuous MRI while causing no significant image distortion in the MR images. The SNR of each image is shown in figure 5.25, which quantitatively confirms that the actuation of MINIR did not bring significant noise to the MRI scanner because the SNR did not drop during actuation, *i.e.*, the average SNR of no actuation and during actuation both equals 28.6.

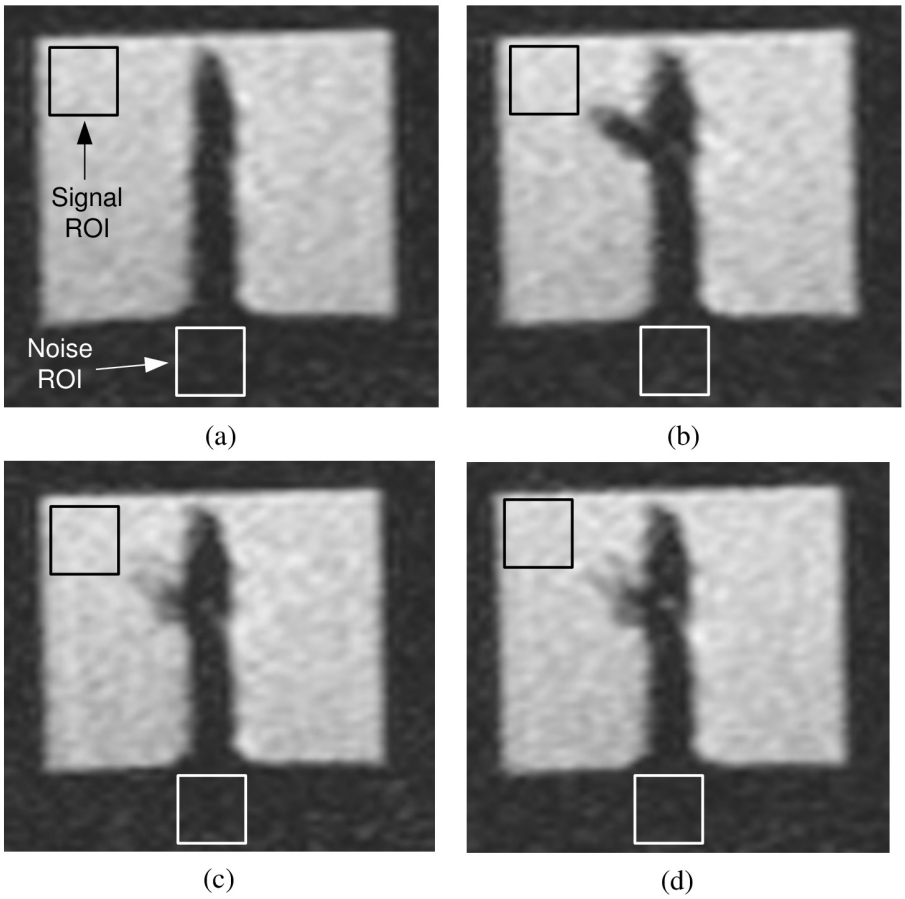

Figure 5.24: Dynamic MR images of step 5 at four diferent time points: (a) No actuation, (b) actuating the first link to left, (c) actuating the second link down, and (d) no actuation.

A high resolution scanning was performed after the actuation in step 5 to see if the configuration of MINIR was as expected. The images are shown in figure 5.26. The images clearly show that the first link of MINIR was actuated to left and the second link

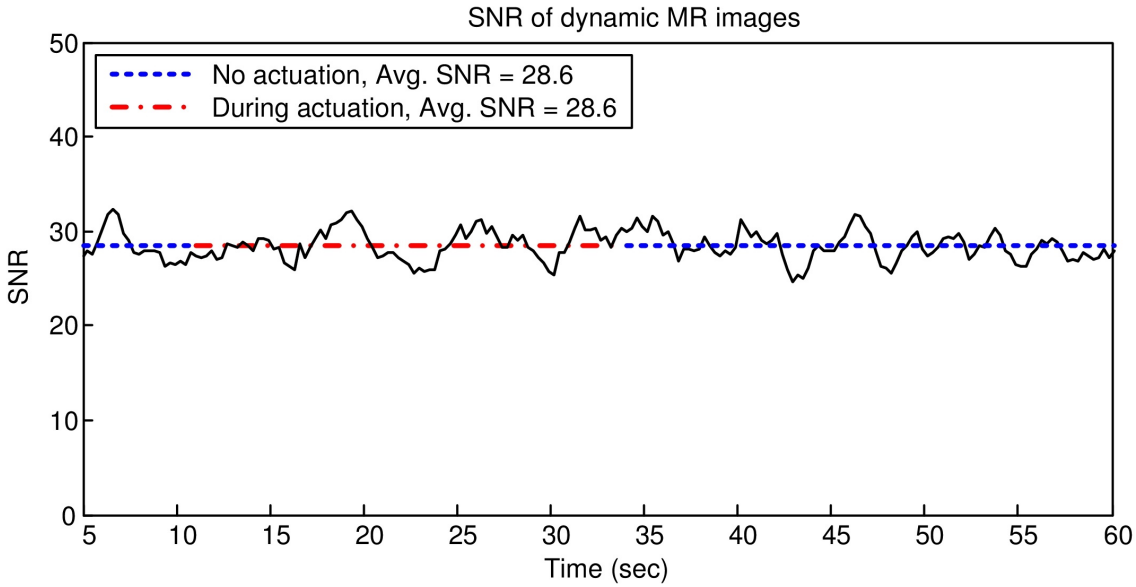

Figure 5.25: SNR of each image obtained in step 5.

was moved down because the links can only be seen in the images of lower slices [see figures 5.26(c) and (d)].

In step 7, we actuated the robot and then started electrocauterization while taking dynamic images to evaluate the influence that the electrocauterization procedure caused in the MR images. The experiment can again be used to verify that the actuation of MINIR did not bring noise to the images. During the experiment, we actuated the first link to right and then moved the second link up. After actuation, we started to electrocauterize the gelatin. The MR images at five different time points are shown in figure 5.27. The images show that MINIR was successfully actuated to right [see figure 5.27(b)] and then out of plane [see figure 5.27(c)]. The electrocauterization was started right after the actuation and successfully created a void in the gelatin [see figure 5.27(d)] because the gelatin was melted. A quantitative analysis of the SNR of each image is shown in figure 5.28. The SNR dropped by 0.7% during actuation, *i.e.*, dropped from 27.6 to 27.4 and 1.4%

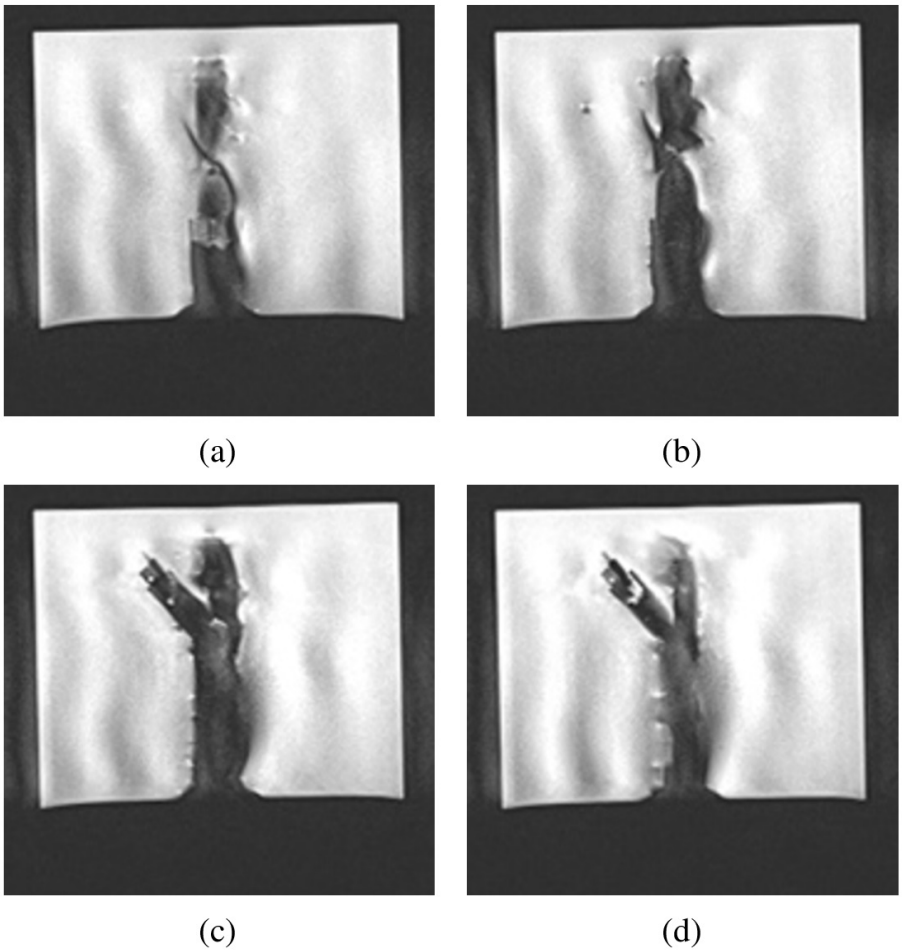

Figure 5.26: High resolution MR images of step 6: (a) slice 1, (b) slice 2, (c) slice 3, and (d) slice 4 of the gelatin slab and MINIR after the actuation in step 5.

during electrocauterization, *i.e.*, dropped from 27.6 to 27.2. This results show that the electrocauterization did not caused significant noise in the MR images and also again confirms that the actuation of MINIR did not affect the image quality.

The last scan of this section was to perform a high resolution scan to make sure MINIR worked as expected in step 7. The images are shown in figure 5.29. The images show that the fist link of MINIR has been moved to right and the second link was moved up because the links can only be seen in the upper layers of the gelatin [see figures 5.29(a) and (b)]. The void in the gelatin created by electrocauterization is also seen in the figure.

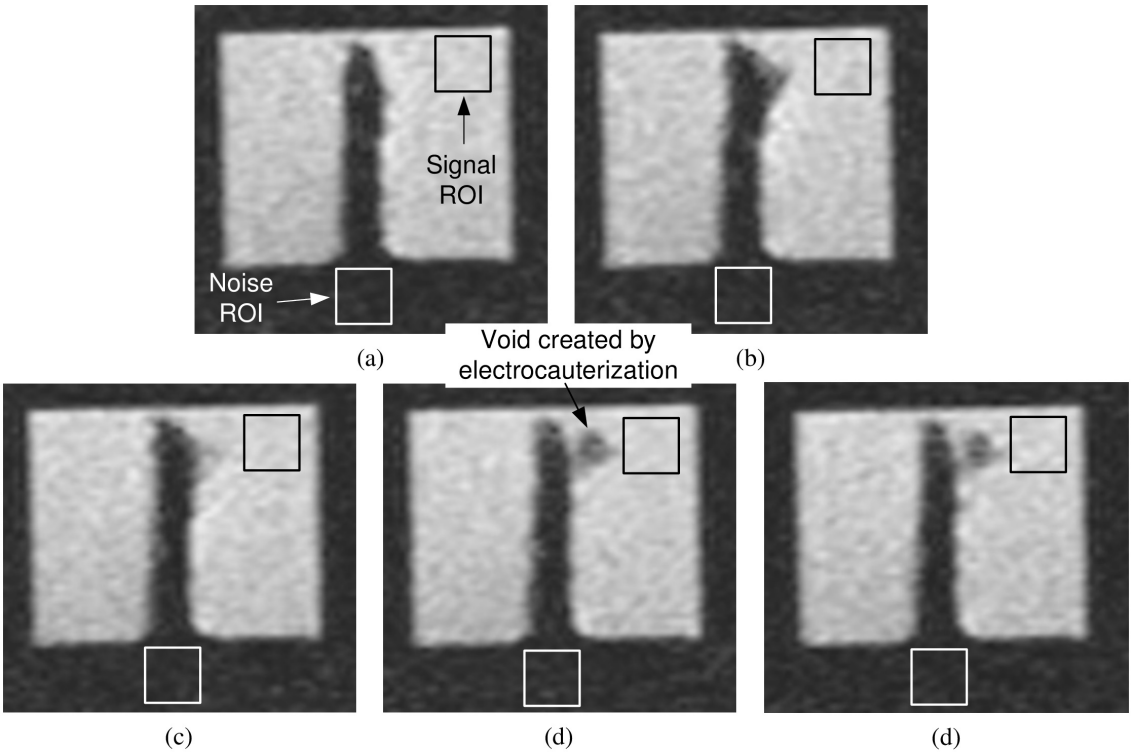

Figure 5.27: Dynamic MR images of step 7 at five diferent time points: (a) No actuation, (b) actuating the first link to right, (c) actuating the second link up, (d) during electrocauterization, and (e) no actuation.

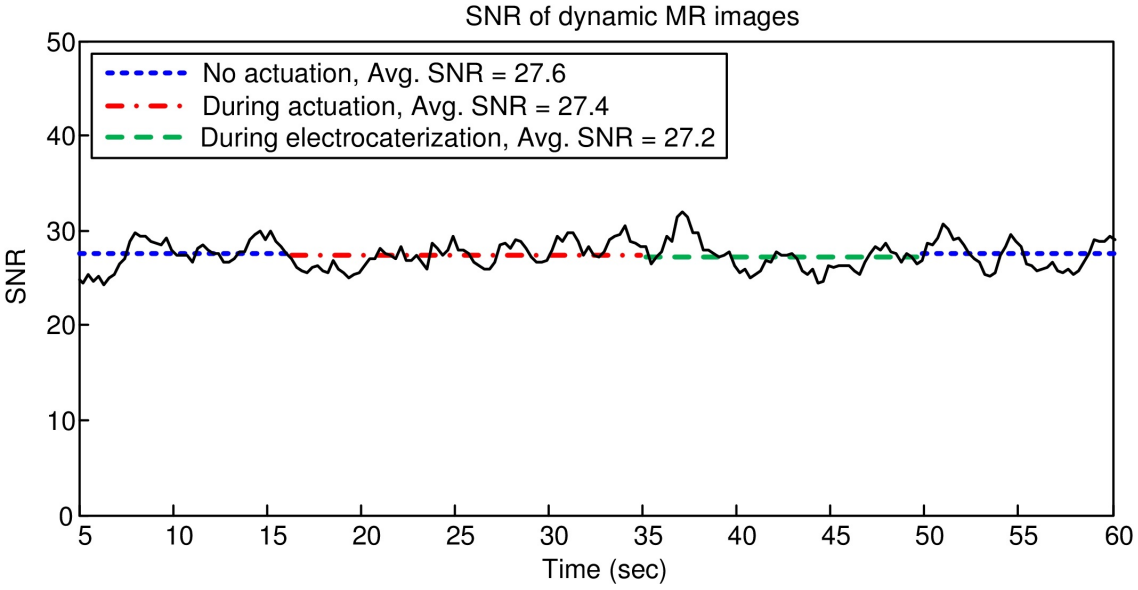

Figure 5.28: SNR of each image obtained in step 7.

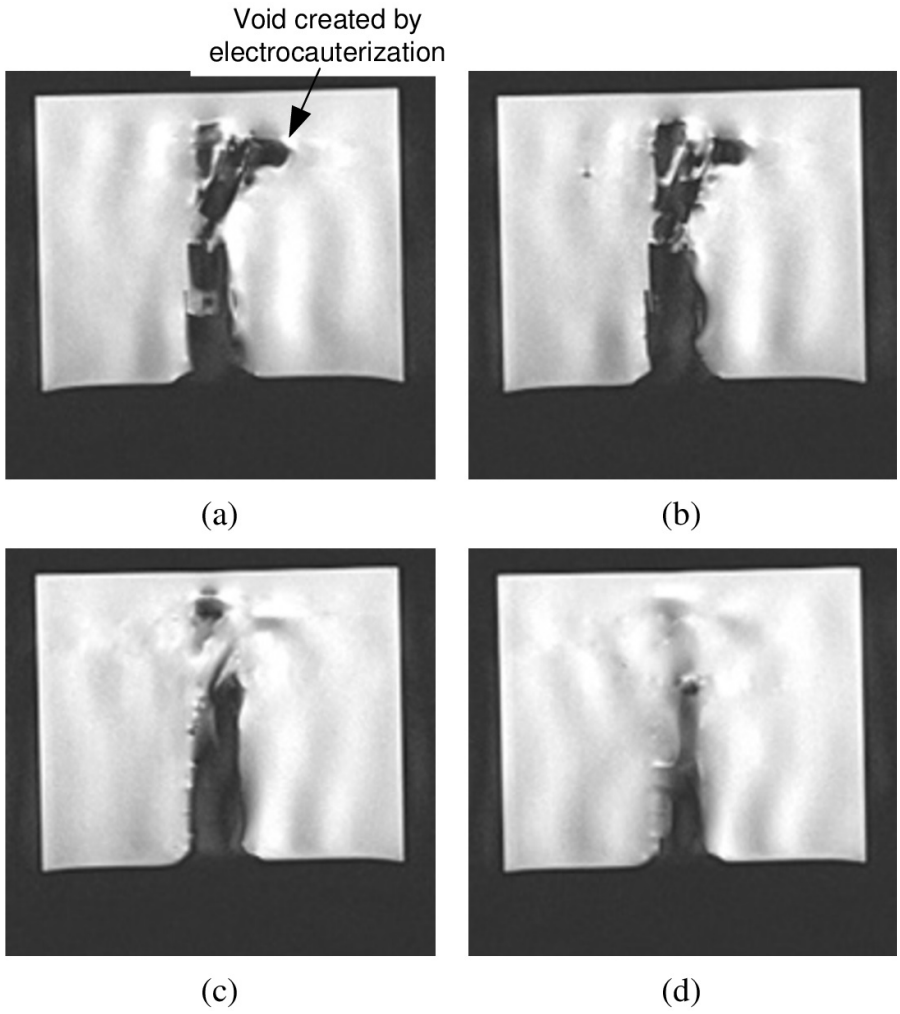

Figure 5.29: High resolution MR images of step 8: (a) slice 1, (b) slice 2, (c) slice 3, and (d) slice 4 of the gelatin slab and MINIR after step 7.

We have confirmed that the entire MINIR system was MRI compatible and effect of the current that was used to actuate SMA spring actuators and the electrocautery probes were not significant after a series of experiment in this section. Therefore, we can conclude that the MRI can be used to provide real-time visual feedback for physicians when performing brain tumor resection using MINIR. With real-time visual feedback, physicians can remove the brain tumor completely and precisely while minimizing trauma to the surrounding healthy brain during intracranial procedures.

5.4.5 *Ex-Vivo* Test

After testing MINIR in gelatin, we further test it in a pig brain to see if it can work as expected. MINIR was covered with a layer of plastic sheath to isolate it from tissue, blood and other liquid in the brain as shown in figure 5.30(a). Figure 5.30(b) shows MINIR was inserted to a pig brain through an opening on the skull.

(a) (b)

Figure 5.30: Photos of the *Ex-Vivo* test: (a) MINIR cover with plastic sheath and only electrocautery tips are outside and (b) MINIR inside a pig brain.

The thickness of the skin and skull was 39 mm, however, MINIR was only 60 mm long. Therefore, only one link of MINIR could be inserted inside the brain. As a result, we only actuated the first link of MINIR in this experiment and the link was actuated while taking dynamic scanning. 400 hundred images were taken during the scanning and TE/TR = 2.46/8 ms. All devices were turned off in the first 100 images and then turned on for 100 images. MINIR was actuated to move to right for 100 images and then stopped for the rest 100 images. The MR images at four different time points are shown in figure 5.31. The images show no observable changes for the first 200 images [see figures 5.31(a) and (b)] and MINIR was moved to right during actuation [see figure 5.31(c)]. The SNR of each image is shown in figure 5.32 and there is no significant change in the four different

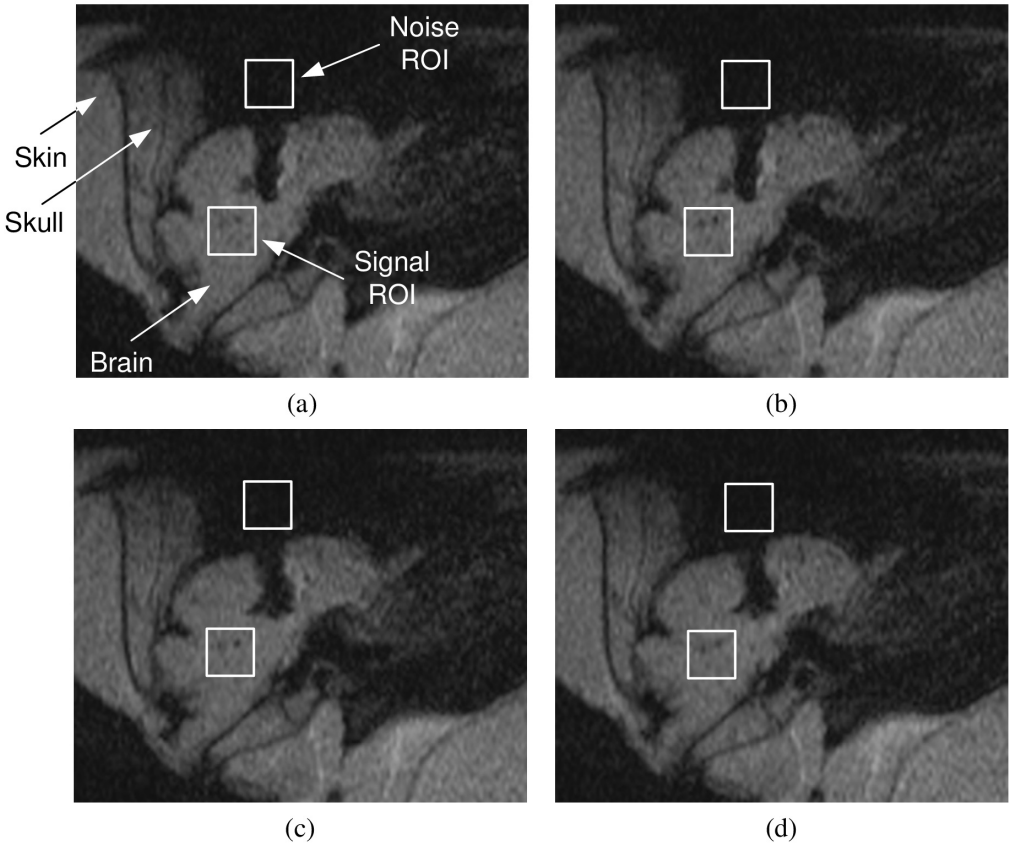

Figure 5.31: Dynamica MR images at four different time pints when MINIR was operating in the brain: (a) All devices power off, (b) all devices power on but no actuation, (c) during actuation, and (d) after actuation (power on but no actuation).

conditions. The SNR only dropped by 0.5%, *i.e.*, dropped from 19.7 to 19.6 after turning on the power of all devices and dropped by 0.5%, *i.e.*, dropped from 19.6 to 19.5 during actuation. The results indicated the noise caused by turning on the power of all devices and passing electric current through the SMA spring actuators was very small and could be neglected.

5.4.6 Image Feedback Control

We have shown that the MR images of the current prototype of MINIR were clear without significant image distortion in sections 5.4.4 and 5.4.5. Therefore, we expect MINIR to

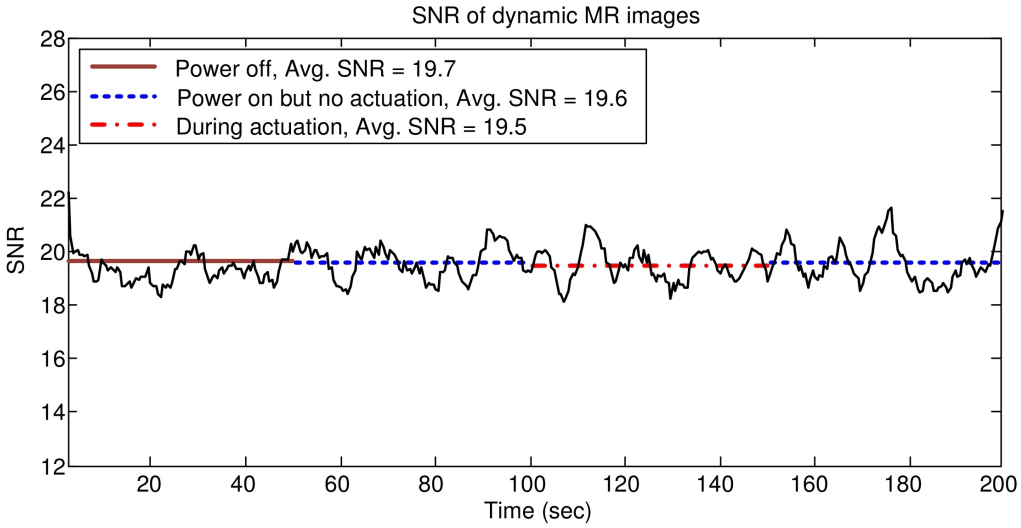

Figure 5.32: SNR of each MR images of the *Ex-Vivo* experiment.

be controlled using real-time MR images as feedback. In this section, we present the experimental results of using image feedback to control the joint motion of MINIR. Since we could not access real-time MR images at this point, we used a camera to get the images of MINIR. The experimental setup is shown in figure 5.33. In this experiment, we assumed that the image plane was parallel to the motion plane.

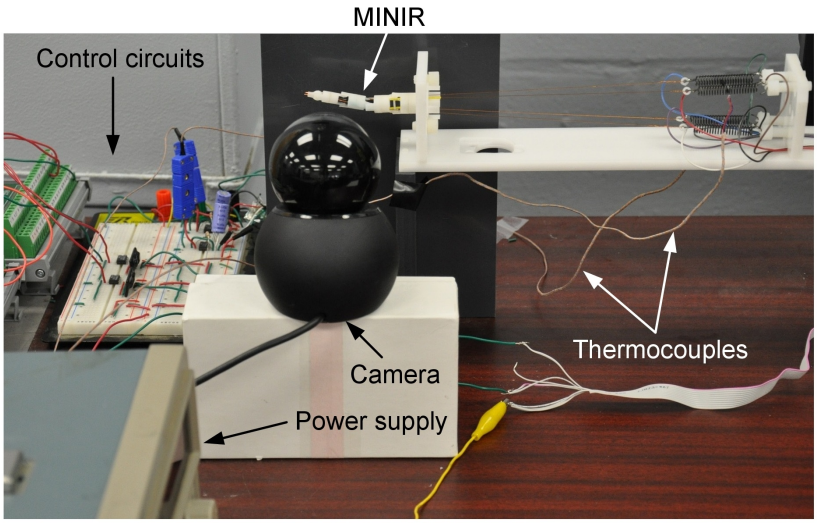

Figure 5.33: Experimental setup for image feedback and temperature feedback motion control of MINIR.

The color depth and frame rate of the camera were set to 8-bit gray scale and 4 fps, respectively, which were close to the image quality that a MRI scanner can get for a dynamic scanning. The 4 fps frame rate was fast enough to be considered as real-time imaging for MINIR because the response of SMA springs was slow. We used Lucas-Kanade Optical Flow Method [92] to track the position of each joint and electrocautery tips and the tracking images are shown in figure 5.34. The images simulated MINIR operating in a medium that contained water so that the background of the image was white which is the color of water in MR images and MINIR was black because of its plastic body. The track point can be selected manually by clicking on the image and the tracking algorithm will find the best feature to track in the nearby areas. The target point was also selected manually and a PWM-PI controller was used to heat the corresponding SMA spring until the track point reached the target point. The target point cannot be selected arbitrarily and can only be located on the path of the track point, therefore, a constraint must be added to the algorithm for the target point. Since we assumed the camera plane was parallel to the motion plane, the path of the track point should be a circle. The center of the circle can be computed using the positions of the track point in different images. After obtaining the rotation center of the track point, the target point can be adjusted to the closest point on the path of the track point if the selected target point was originally not on the path.

The experimental results of image feedback control are shown in figure 5.35. The controller worked well and the maximum steady state error was 0.2°. Stick-slip was observed during the experiments and the maximum jump was observed to be 3.2°. This issue must be solved in the future for more precise control. It is important to note that

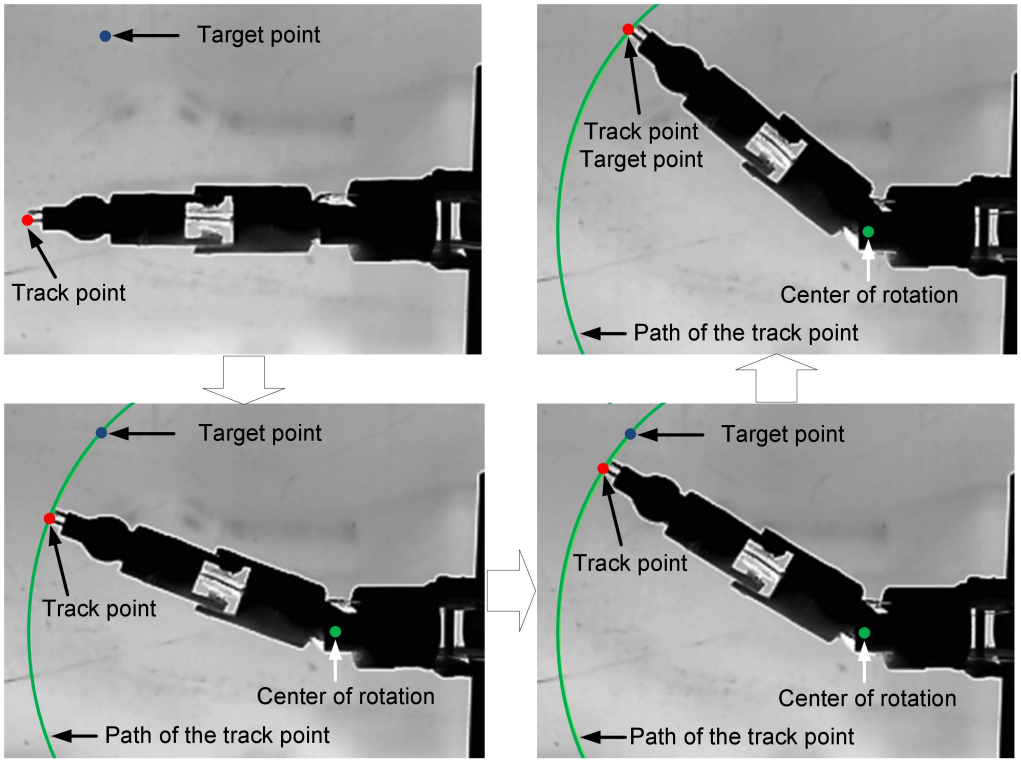

Figure 5.34: Image feedback control of MINIR.

when the motion direction changes, the heated SMA spring must be cooled down below A_s before the other SMA spring is actuated. If the other SMA spring is heated right away, both SMA springs will be at higher temperatures. In this case, the heated SMA spring might not be able to reach the target location and that could result in overheating. Therefore, monitoring the temperature in each SMA spring is required in the antagonistic setup. This is why temperature feedback is necessary even if image feedback control is used.

5.4.7 Temperature Feedback Control

The image feedback control may fail due to the noise in the MR images or the missing of track points. Since safety is the most important factor in a surgical robot, a backup

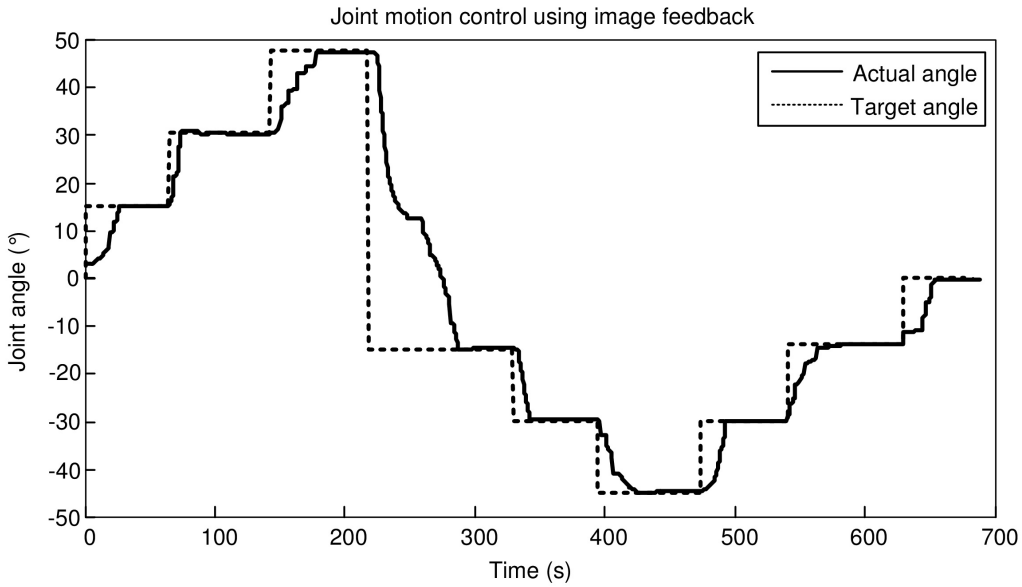

Figure 5.35: Experimental results of image feedback motion control.

controller has to be implemented for MINIR. In the previous section 5.4.6, we discussed the reason why it is necessary to monitor the temperature in each SMA spring. Since the temperature information is available, it is natural to use temperature feedback as the backup control strategy. The experimental setup of temperature feedback motion control is the same as figure 5.33, but we only relied on temperature to control the joint motion of MINIR. The experimental results are shown in figure 5.36. In the figure, we can see that the difference between theoretical model and experimental data was significant. The reason for this difference was that theoretical model, *i.e.* equation 5.29, only considered the stiffness of the bias (non-heated) SMA spring and did not include friction force and resistant force of the sheaths. Therefore, we did experiments to find the equivalent stiffness of the joint and the results are shown in figure 5.37. It is clear in the figure that the friction force and resistant force increased the stiffness of the robot joint significantly. The joint angle increased linearly with the spring force, which implied that the stiffness of the joint

was constant within the motion range, $\pm 60^{\circ}$. By fitting the experimental results linearly, we found the equivalent spring constant was 941.9 N/m. We then used the equivalent spring constant to replace the spring constant, k, in equation 5.29 and re-computed the theoretical joint angle. The results are shown in figure 5.38.

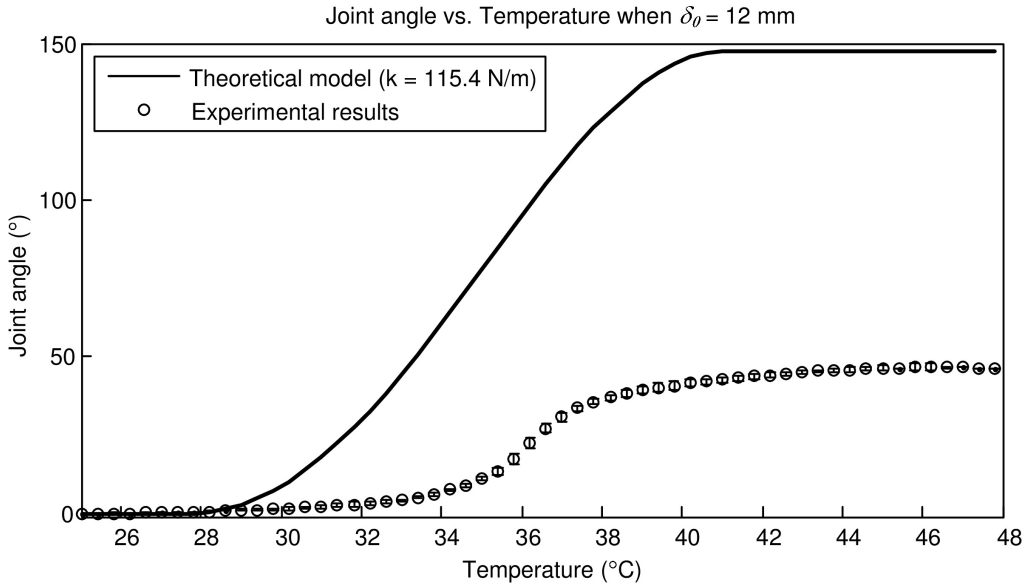

Figure 5.36: Experimental results of the joint angle at different temperatures when only the stiffness of the bias spring was considered.

Although the theoretical model fitted the experimental data better than in figure 5.36, the model was still not precise enough to be used to control the robot. The difference between the experimental results and theoretical model might come from the nonlinear properties such as backlash, hysteresis and friction in the tendon-sheath mechanism. The nonlinear characteristics of tendon-sheath mechanisms have been discussed and modeled, such as in [100], and they can be compensated using feedforward terms in the controller [101]. We have not modeled the nonlinear characteristics of the tendon-sheath mechanism used in MINIR, but we believe that the antagonistic SMA spring model will be valid to control the joint motion of MINIR if the nonlinear characteristics of the tendon-

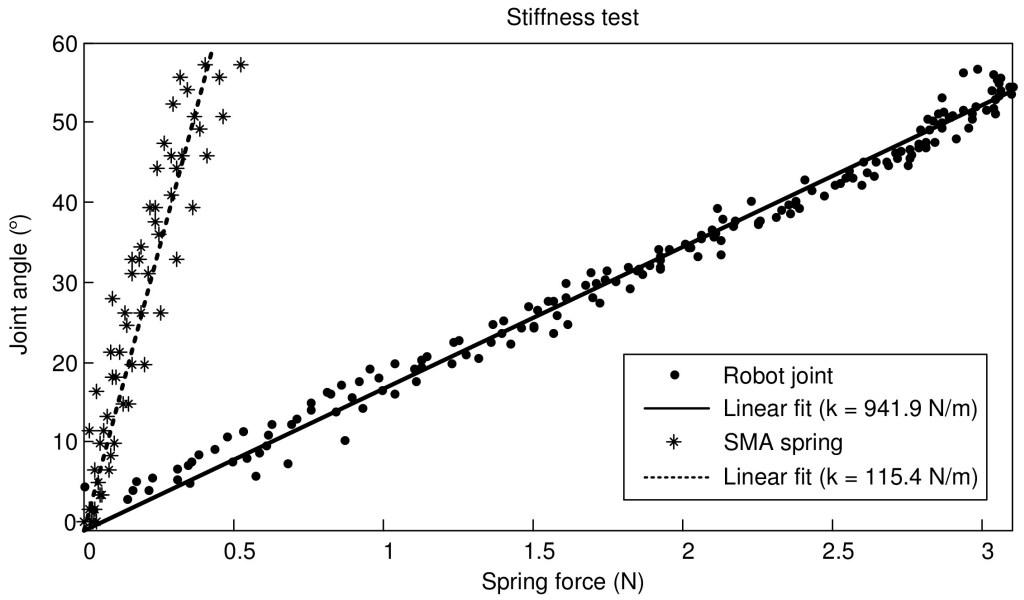

Figure 5.37: Stiffness tests of the bias spring and robot joint.

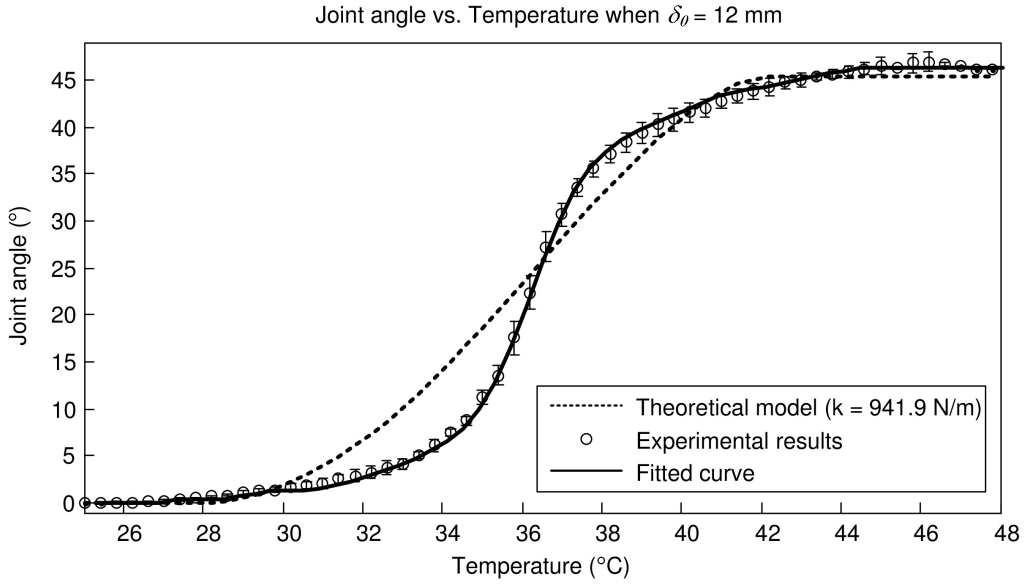

Figure 5.38: Experimental results of the joint angle at different temperatures using emperical stiffness of the joint.

sheath mechanism are incorporated into the model.

At this point, we decided to use experimental data to control the robot since it was repeatable. The fitted curve was computed using Eureqa [102] and is shown as the solid line in figure 5.38. Eureqa is a software for detecting equations and mathematical

relationships in the data. The empirical model is:

$$T = 26.8 + 0.444\theta - \frac{3.73}{0.718 + \theta} + cos(0.228\theta) - 4.63cos(2.25 + 0.118\theta) \qquad (5.33)$$

where θ is the joint angle, *i.e.* control command, obtained from the control interface shown in figure 5.34.

The experimental results of using equation 5.33 to control the joint motion of the robot are shown in figure 5.39. The joint angle was converted to temperature command, T, through equation 5.33 and then sent to the PWM-PI temperature controller. In this experiment, the SMA spring #1 was used to move the joint to positive joint angle while the SMA spring #2 was used to move the joint to negative joint angle. The experimental results show that the temperature feedback motion control worked well with the maximum steady state error of 3°. It is important to note that when the robot was commanded to change the motion direction, the heated SMA spring should be cooled down below A_s before the other SMA spring was actuated. figure 5.39 clearly shows that when the control command changed from 45° to -15°, the SMA #1 was cooled to 26°C before the SMA #2 was heated.

5.5 Summary

In this chapter, we presented a new design of MINIR using SMA spring actuators along with tendon-driven mechanisms to actuate the various joints of MINIR. The MINIR prototype overcomes several limitations of our previous prototypes discussed in chapter 4 while having a lager range of motion, larger output force and better MRI compatibility.

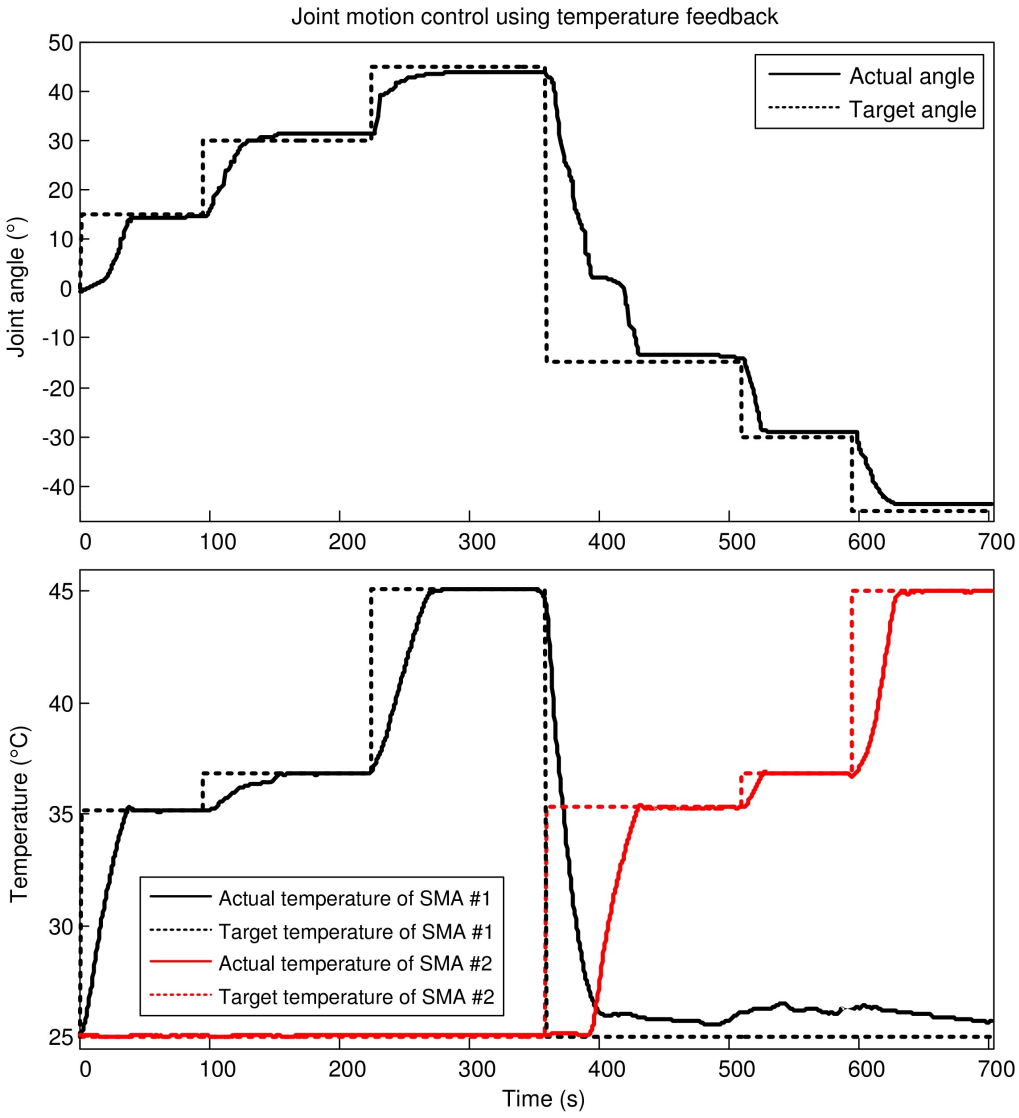

Figure 5.39: Experimental results of temperature feedback motion control.

We used two pairs of antagonistic SMA springs to actuate two joints of MINIR. The joints were actuated to move back and forth successfully and each joint could be controlled independently.

We modeled and characterized the behavior of a single SMA spring as well as antagonistic SMA springs. We also designed and developed our own experimental setup to determine material parameters that are required for the theoretical models. The models

derived from the constitutive equation of SMAs can be used to describe the relations of the recovery length and the temperature of SMA springs. We further used these models to develop a temperature feedback control algorithm to control the recovery length of the antagonistic SMA springs and hence control the joint motion of MINIR. However, the theoretical model did not fit the experimental data well due to the hysteresis in the cabling as well as the stick-slip phenomenon. Therefore, we used an empirical model to control the robot instead of using the theoretical model and the maximum positioning error of MINIR when using temperature feedback control was 3°. Moreover, the models developed in this chapter enable us to use temperature feedback to control the output force of the robot if the displacement of the SMA spring or the joint motion of the robot is measured.

We then demonstrated that MINIR is fully MRI compatible by taking static and dynamic MR images. The MR images show no significant image distortion and a very limited SNR drop was observed by introducing MINIR in MRI. Thus, the current design of MINIR enables the possibility of using MR images as visual feedback for physicians when performing a deep brain tumor resection. We then implemented an image feedback control algorithm to control the joint motion of MINIR. The maximum positioning error was 1° when the image feedback controller was used. Since both image feedback and temperature feedback can be used to control the joint motion of MINIR, temperature feedback can be used as a backup control scheme for MINIR in case the image feedback control fails.

Chapter 6

Conclusions and Future Work

6.1 Conclusions

The objective of this research was to develop a MRI-compatible meso-scale neurosurgical robot to overcome the limitations of current procedures of brain tumor resection. In this thesis, we presented the design, development and experimental results of two prototypes of MINIR with two different actuation mechanisms. Based on the results, we have the following conclusions.

- Brass is MRI-compatible but the sharp edge of a brass object may cause distortion in MR images. Therefore, only a small amount of brass should be used to develop MRI-compatible devices. Plastic, such as Delrin®, is MRI-compatible and is more favorable for building MRI-compatible devices.

- The antagonistic SMA actuation mechanisms were successfully used to actuate the joints of MINIR and each joint can be controlled independently.

- SMA wires and SMA springs were successfully used as actuators to develop MRI-compatible robotic systems and they could be actuated within or close to the imaging region of MRI scanners during continuous scan while causing no significant noise to MR images.

- MR image quality was better when the SMA actuators were placed away from the

imagining region than when placed within the imaging region.

- MINIR is MRI-compatible and can be operated under dynamic MRI without causing significant noise in MR images. Which enables it to be controlled under real-time MRI guidance.

- Temperature feedback can be used as a backup control scheme to control the joint motion of MINIR in case the image tracking algorithm for image feedback control fails. However, the theoretical model could not be used to control the third generation of MINIR due to the nonlinear properties of the tendon-sheath mechanism. An empirical model instead of the theoretical model was used to control the joint motion of the third generation of MINIR using temperature feedback. This is because the theoretical model that we developed in the thesis did not take into account the nonlinear properties of the tendon-sheath mechanism. However, the nonlinear characteristics of tendon-sheath mechanisms have been discussed and modeled in several researches, such as in [100], and they can be compensated using feedforward terms [101]. Therefore, we believe that the theoretical model will be valid to control the joint motion of MINIR if the nonlinear characteristics of the tendon-sheath mechanism are incorporated into the model.

- The responses of SMA actuators are slow which is not a problem for our application, however, it might be an issue when used for other applications. Therefore, an active cooling system will be beneficial for SMA actuators.

- A PWM-PI temperature controller with a multiplexed control circuit was imple-

mented to control the temperatures of multiple SMA actuators simultaneous and independently by using one power supply.

- A 0.5 mm diameter SMA wire could generate up to 1.4 N of force in the bent configuration and was able to move a link of MINIR in a gelatin medium. A 6.2 mm diameter SMA spring, with a spring wire diameter of 0.76 mm, could generate up to 3.9 N of force. SMA actuators are compact and have a large force to weight ratio so that they are good candidates to be used in meso-scale robotic systems.

6.2 Contributions

The contributions of this research are presented as follows:

- Designed and developed two prototypes of MINIR which can be operated under continuous MRI and created no significant distortion in the MR images of dynamic scanning. The motion range and output force of MINIR met the requirements for use in neurosurgical applications.

- Modeled the bending displacement vs. temperature relationship and the block force behavior of a SMA wire in bent configurations based on the constitutive models of SMAs.

- Modeled the spring displacement vs. temperature relationship and the block force behavior of a SMA spring based on the constitutive models of SMAs.

- Developed an image feedback control algorithm to control the joint motion of MINIR.

- Successfully used temperature feedback through the model developed in the thesis to control the joint motion of the second generation of MINIR.

- Successfully used temperature feedback through a empirical model to control the joint motion of the third generation of generation of MINIR.

- Observed that the generated force of a SMA wire in bent configurations is relatively independent to the strain in the SMA wire and is dependent on the temperature in the SMA wire. This observation provides a feasibility of using SMA wires as intrinsic force sensors to measure the generated force of the SMA wires through temperature.

- Observed that when the SMA actuators are placed away from the imaging region, the disturbance in the MR image caused by the SMA actuator was negligible.

6.3 Future Work

The future work which could potentially improve this research are listed below:

- Model and compensate the nonlinear properties, such as backlash, friction and hysteresis, of the tendon-sheath mechanism used in the third generation of MINIR so that the theoretical model of the SMA spring can be used to control the joint motion of MINIR using temperature feedback

- Investigate using SMA actuators as intrinsic force sensors through the theoretical models developed in this thesis.

- Investigate alternative MRI-compatible sensing techniques, such as magnetic sensors and optic-fiber techniques, to directly measure the joint motion of MINIR.

- Investigate using alternative actuation techniques combined with tendon-sheath mechanisms to actuate MINIR. Since the tendon-sheath mechanism enables us to place the actuators away from the imaging region, some MRI-compatible electric actuators, such as piezoelectric motors, could be used.

Appendix A

Engineering Drawings

The detailed engineering drawings of each part of the robots are presented in this chapter. The drawings of the SMA wire actuated MINIR are presented in appendix A.1 and the drawings of the SMA spring actuated MINIR are presented in appendix A.2.

A.1 Engineering drawings of the SMA Wire Actuated MINIR

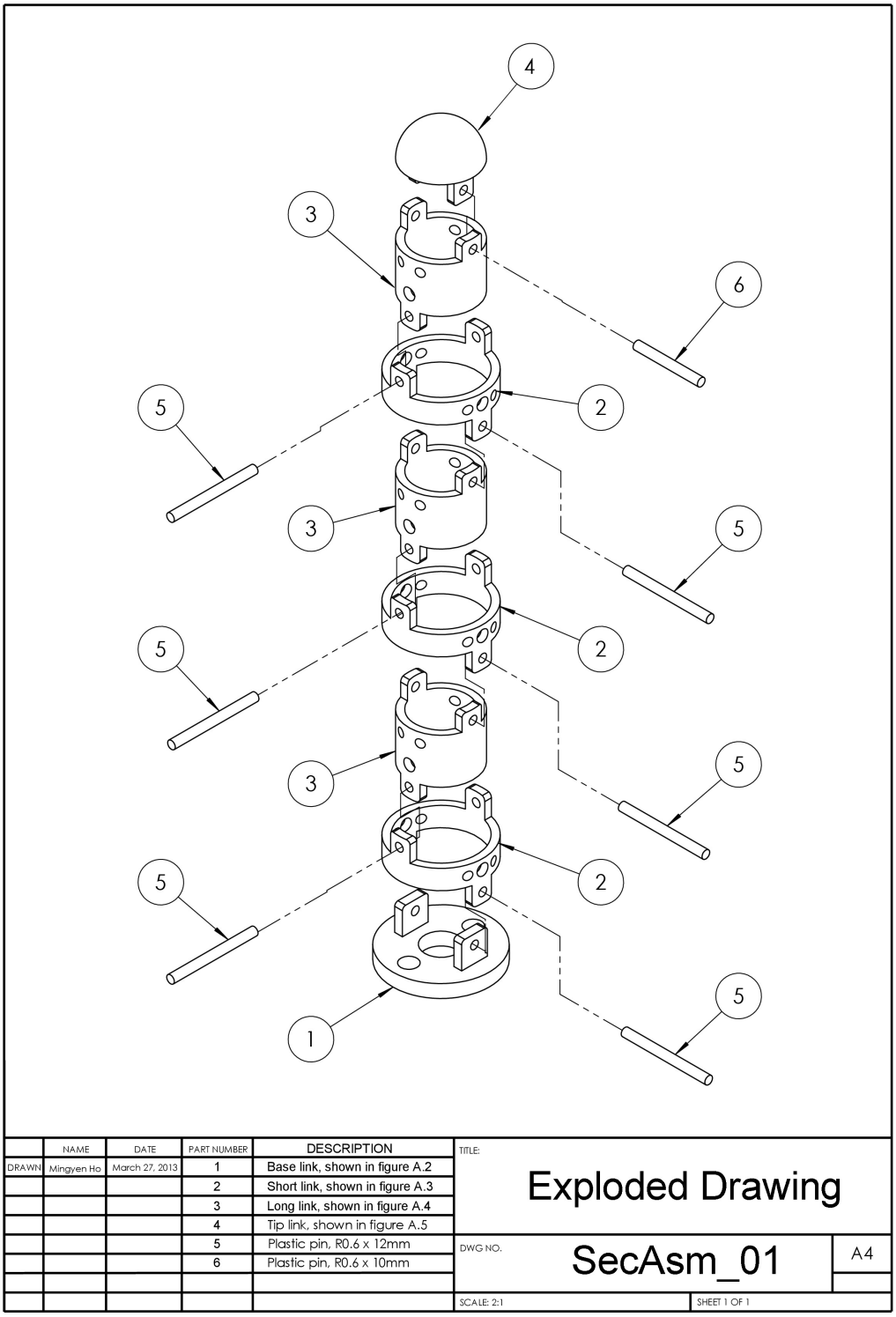

	NAME	DATE	PART NUMBER	DESCRIPTION
DRAWN	Mingyen Ho	March 27, 2013	1	Base link, shown in figure A.2
			2	Short link, shown in figure A.3
			3	Long link, shown in figure A.4
			4	Tip link, shown in figure A.5
			5	Plastic pin, R0.6 x 12mm
			6	Plastic pin, R0.6 x 10mm

TITLE: Exploded Drawing

DWG NO. SecAsm_01 A4

SCALE: 2:1 SHEET 1 OF 1

Figure A.1: Exploded drawing of the SMA wire actuated MINIR.

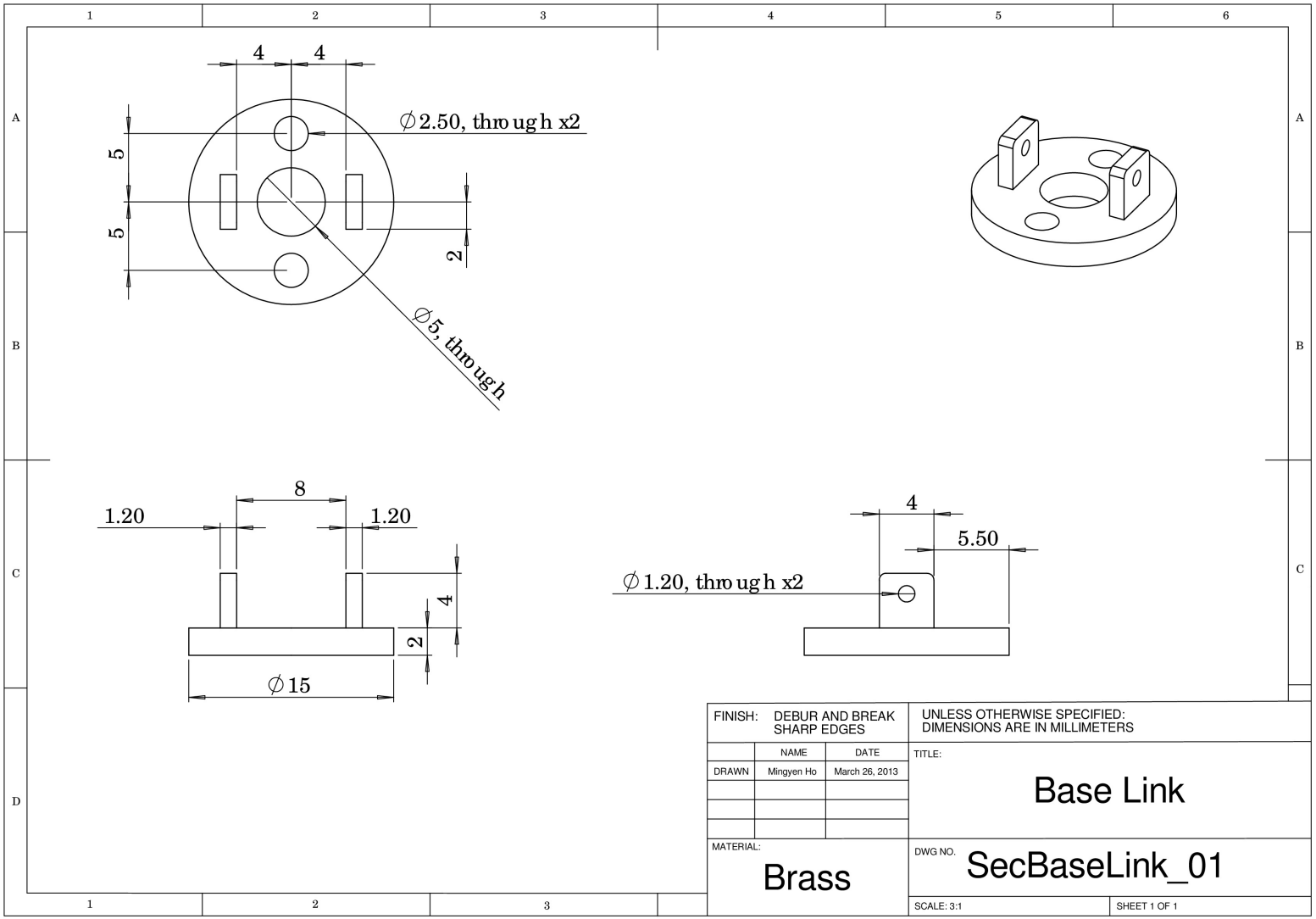

Figure A.2: Engineering drawing of the based link of the SMA wire actuated MINIR.

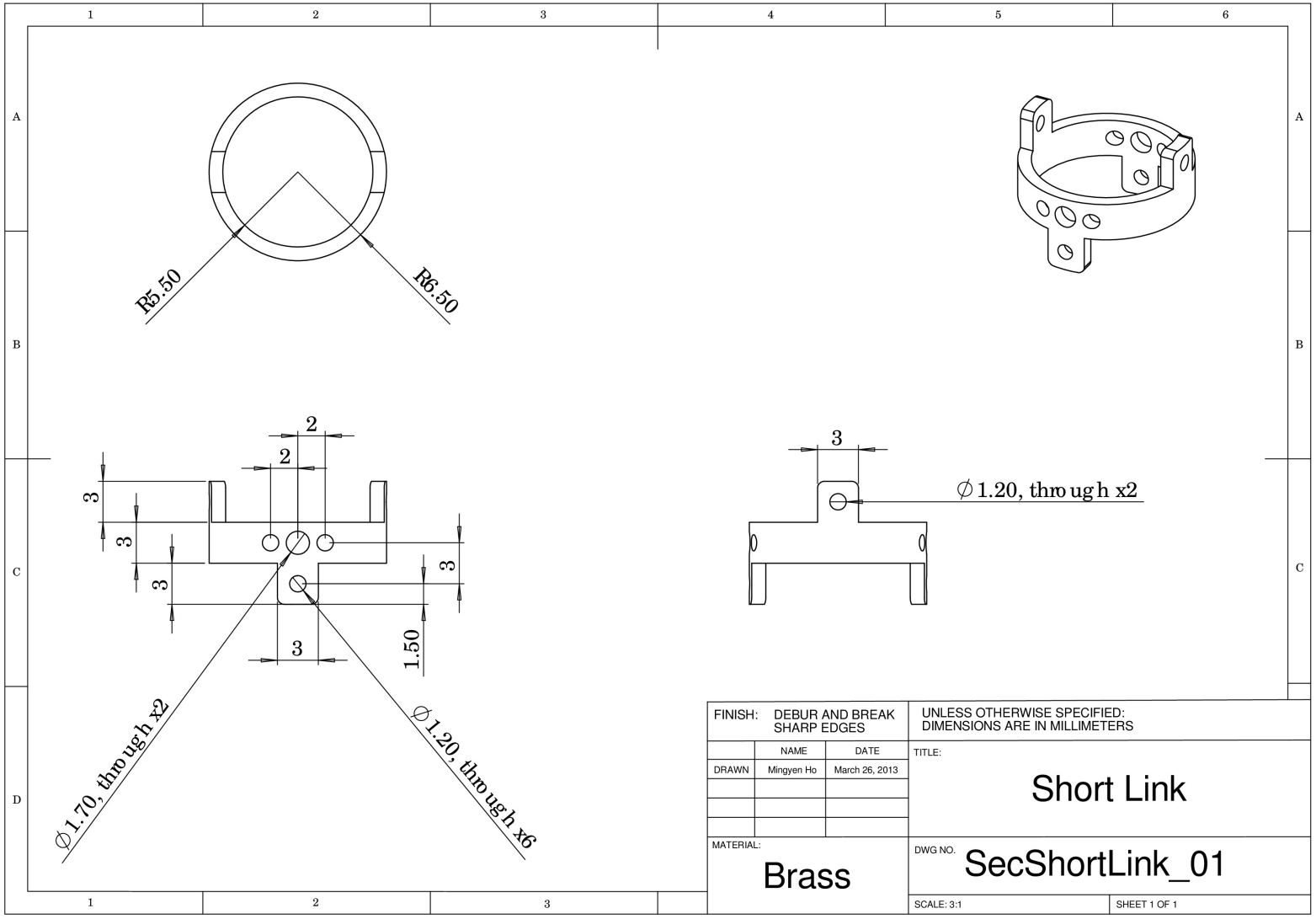

Figure A.3: Engineering drawing of the short link of the SMA wire actuated MINIR.

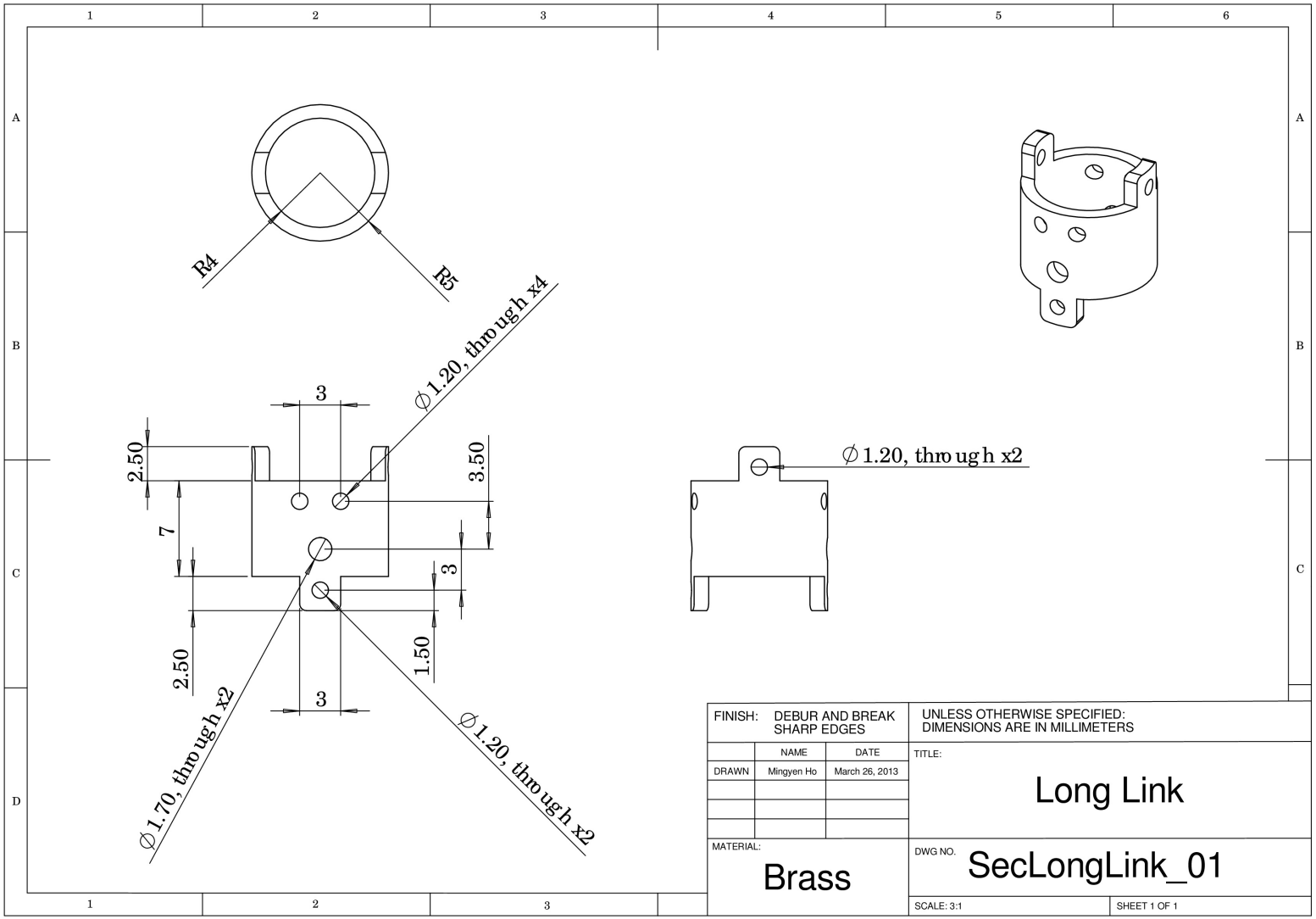

Figure A.4: Engineering drawing of the long link of the SMA wire actuated MINIR.

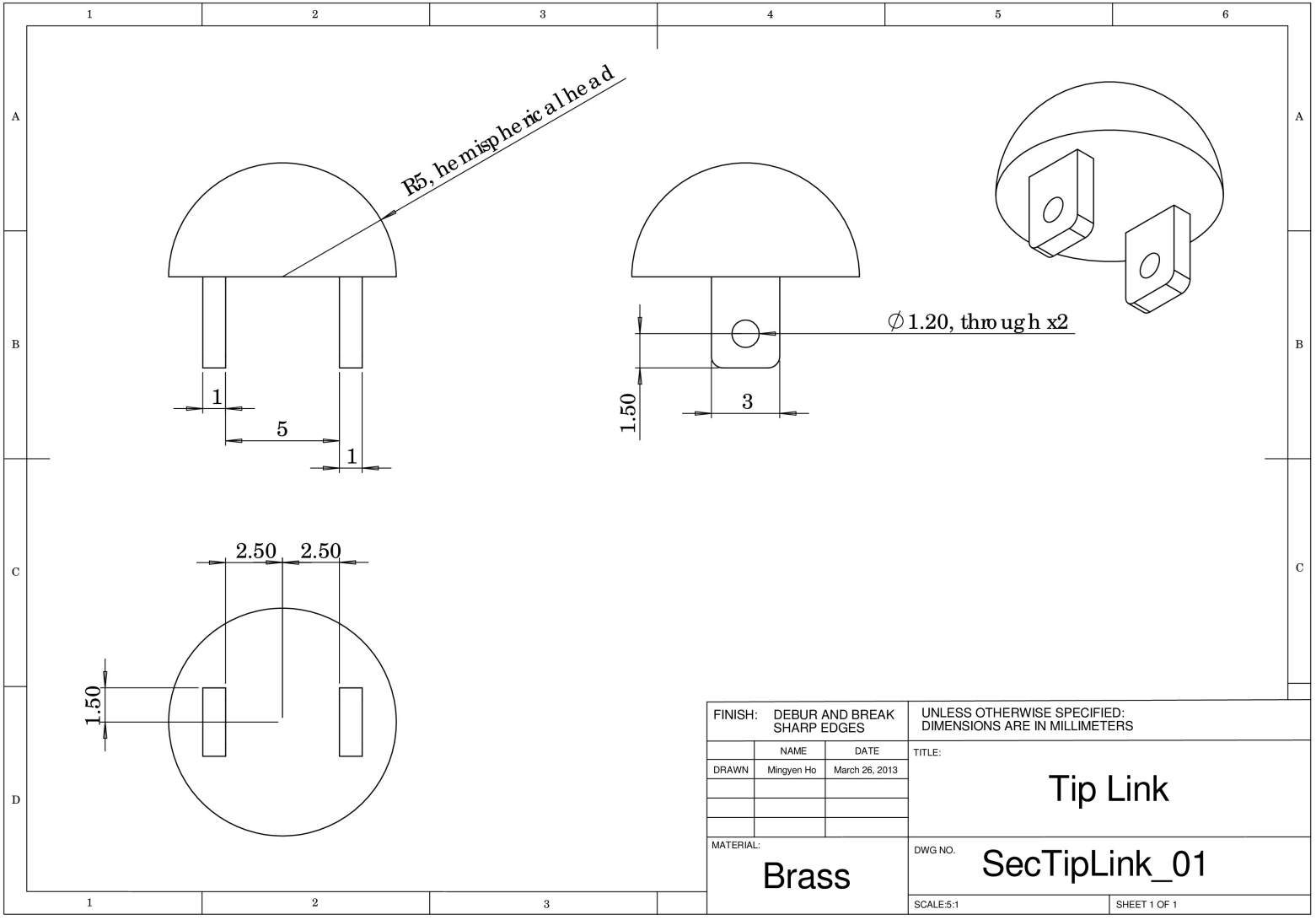

Figure A.5: Engineering drawing of the tip link of the SMA wire actuated MINIR.

A.2 Engineering drawings of the SMA Spring Actuated MINIR

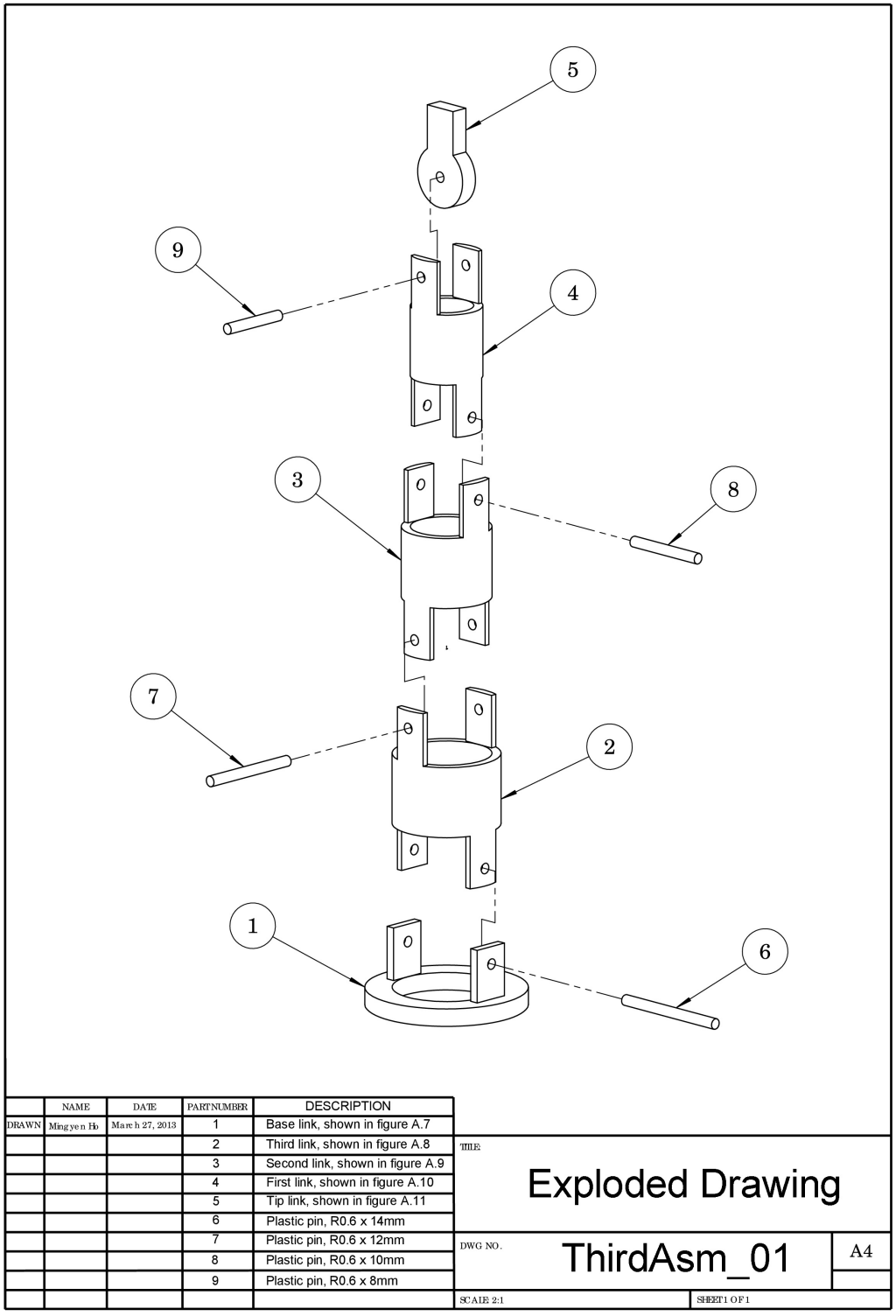

	NAME	DATE	PART NUMBER	DESCRIPTION
DRAWN	Mingyen Ho	March 27, 2013	1	Base link, shown in figure A.7
			2	Third link, shown in figure A.8
			3	Second link, shown in figure A.9
			4	First link, shown in figure A.10
			5	Tip link, shown in figure A.11
			6	Plastic pin, R0.6 x 14mm
			7	Plastic pin, R0.6 x 12mm
			8	Plastic pin, R0.6 x 10mm
			9	Plastic pin, R0.6 x 8mm

TITLE: Exploded Drawing

DWG NO. ThirdAsm_01 A4

SCALE 2:1 SHEET 1 OF 1

Figure A.6: Exploded drawing of the SMA spring actuated MINIR.

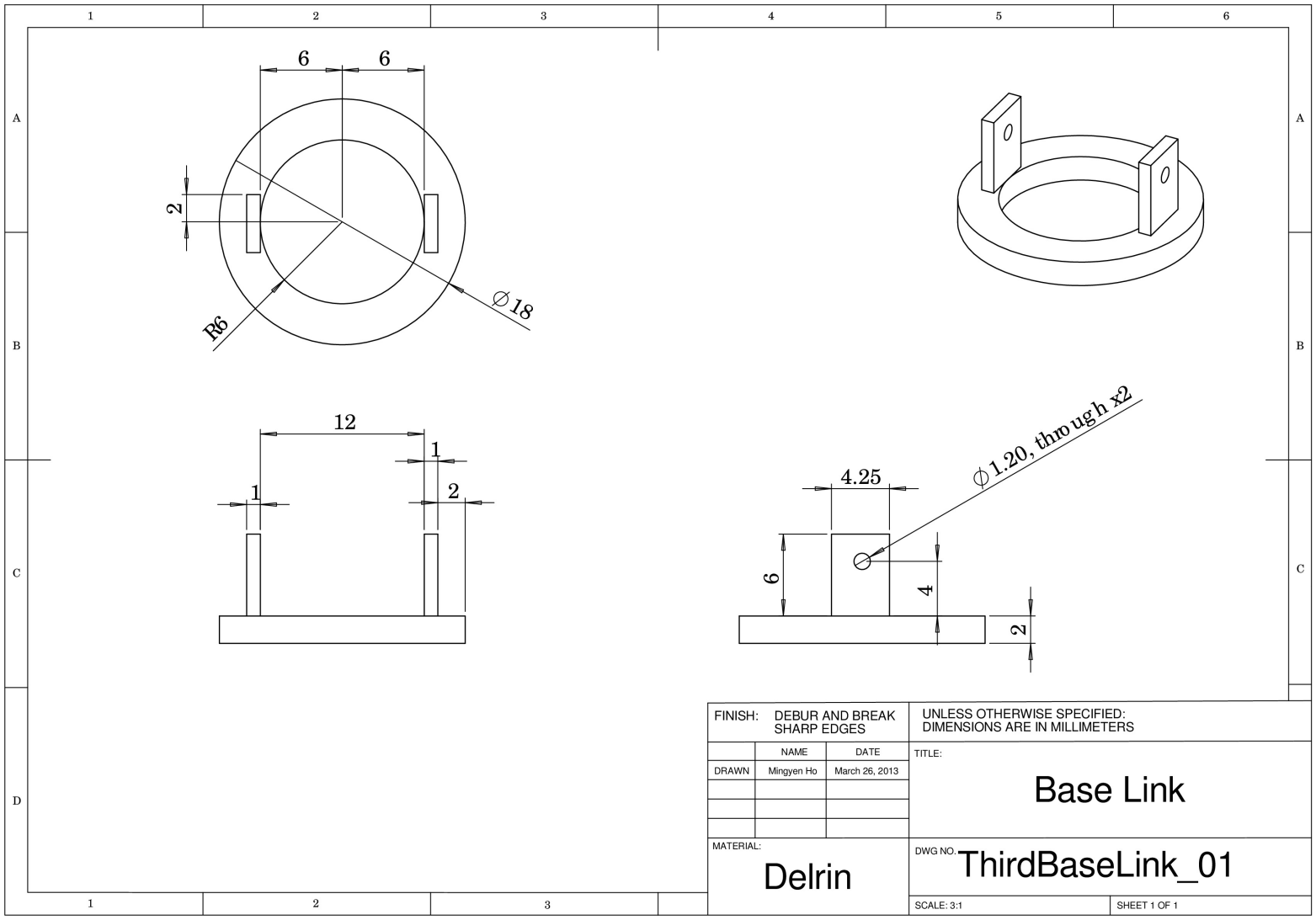

Figure A.7: Engineering drawing of the base link of the SMA spring actuated MINIR.

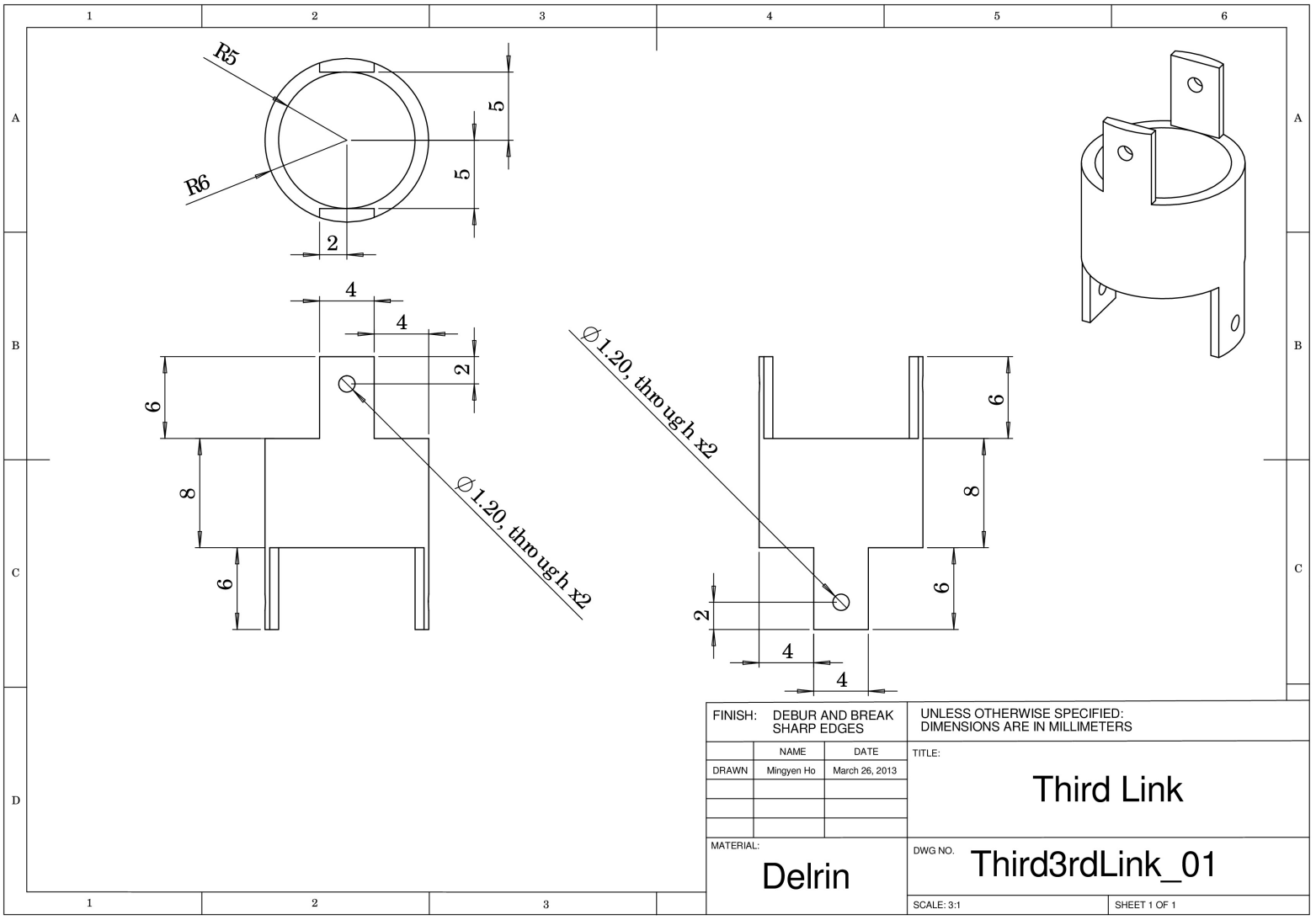

Figure A.8: Engineering drawing of the third link of the SMA spring actuated MINIR.

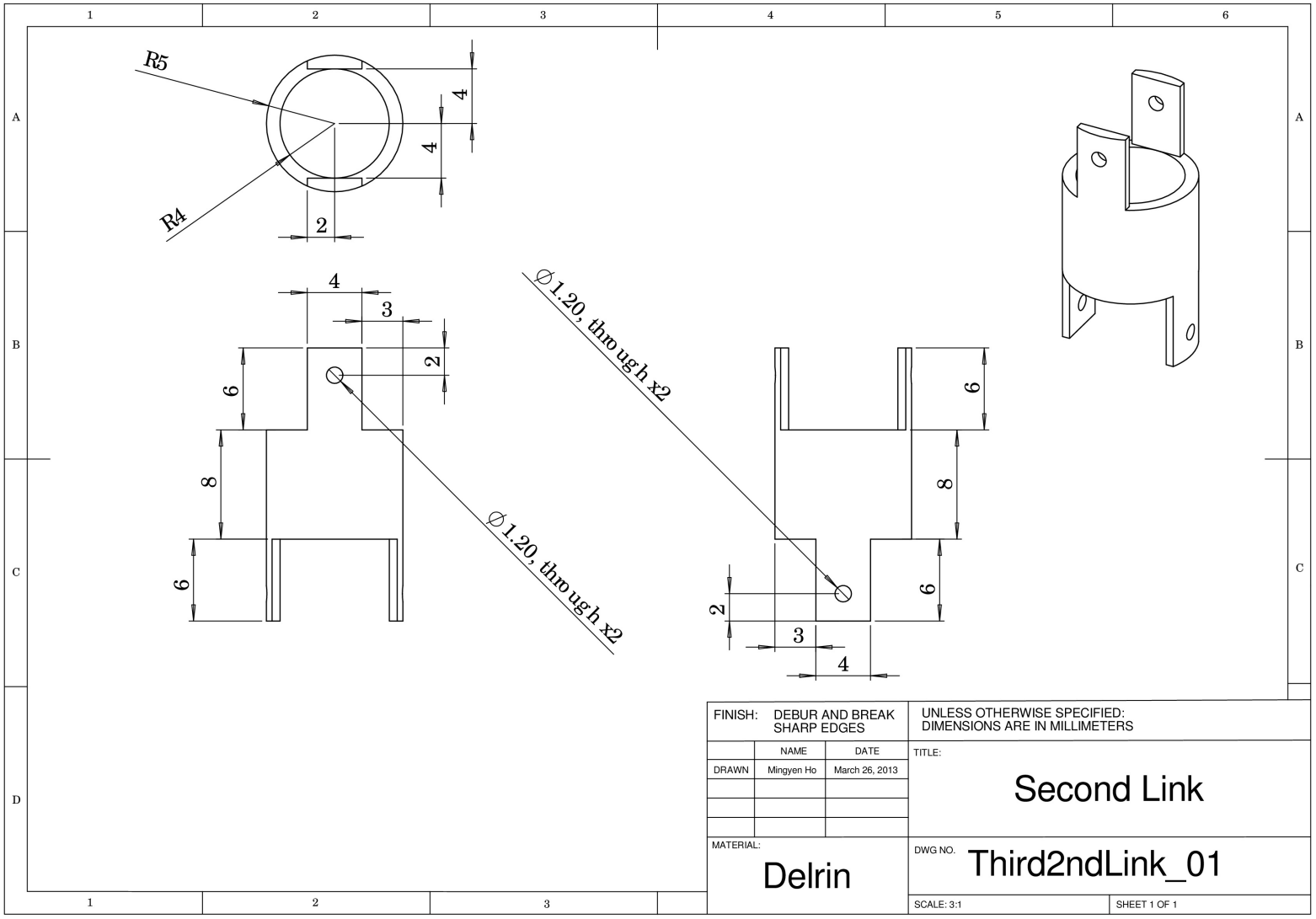

Figure A.9: Engineering drawing of the second link of the SMA spring actuated MINIR.

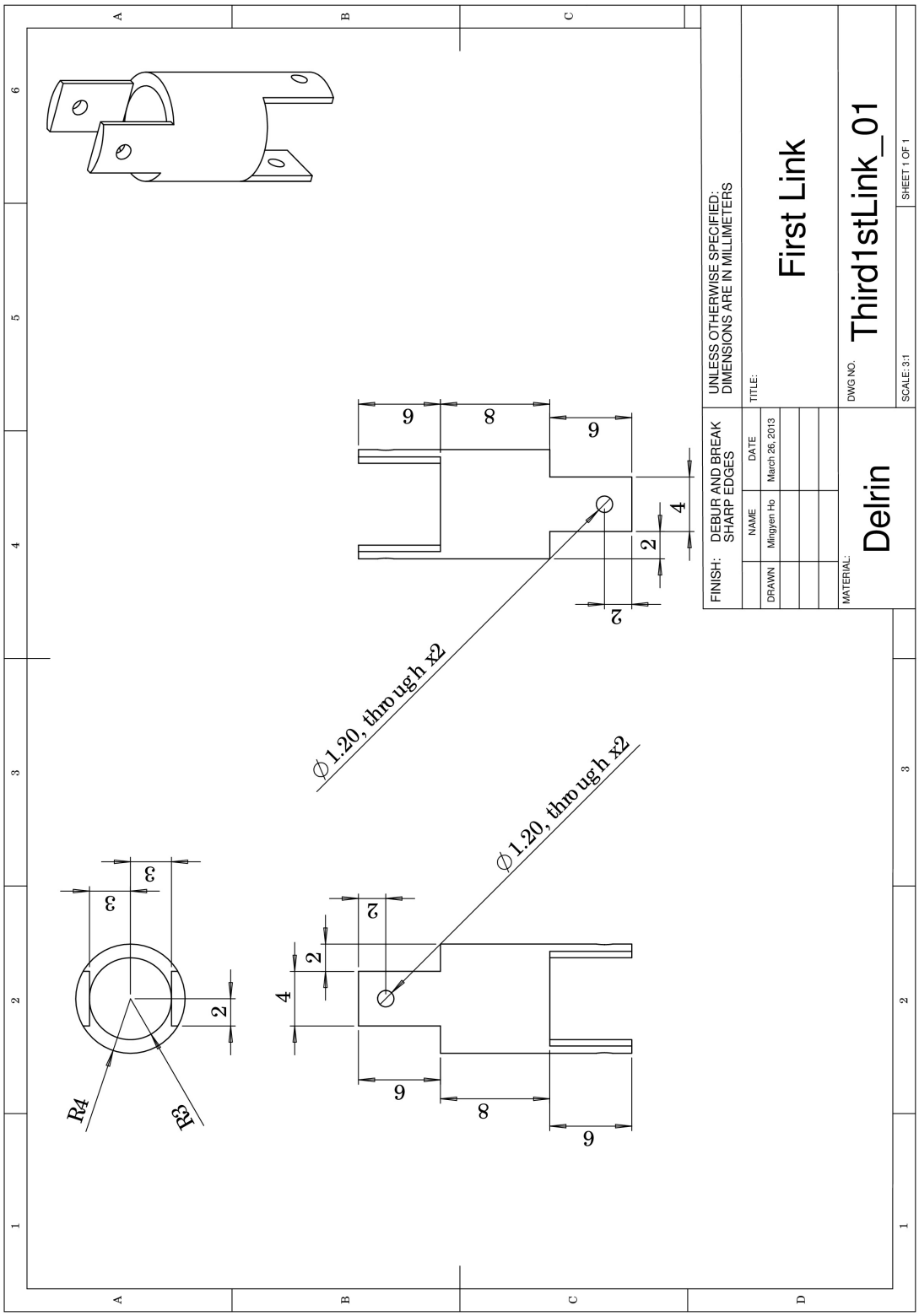

Figure A.10: Engineering drawing of the first link of the SMA spring actuated MINIR.

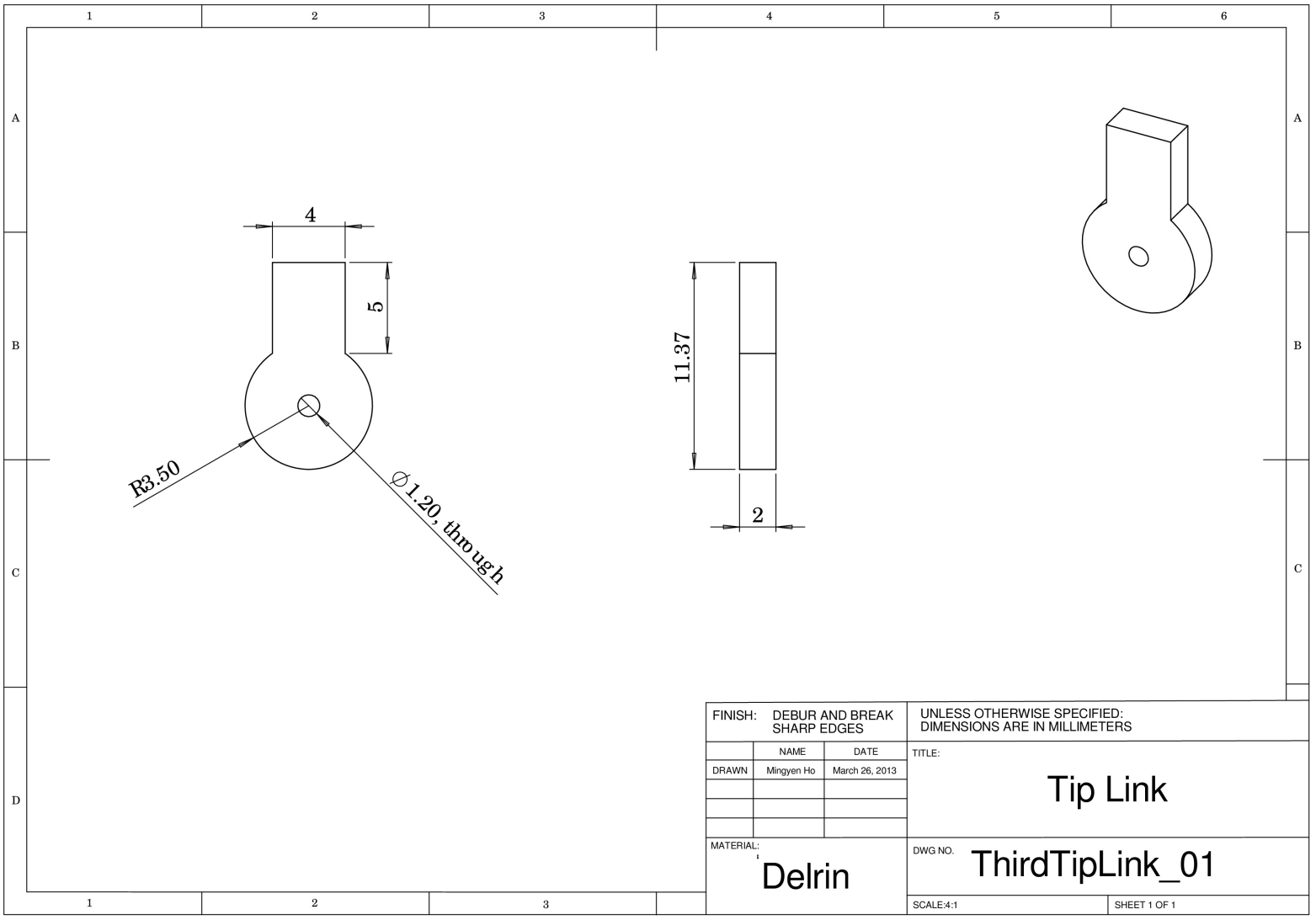

Figure A.11: Engineering drawing of the tip link of the SMA spring actuated MINIR.

Bibliography

[1] Malika L. Siker and Minesh P. Mehta. Resection versus radiosurgery for patients with brain metastases. *Future oncology*, 3(1):95–102, 2007.

[2] Pawel G. Ochalski and Johnathan A. Engh. Endoscopic port surgery for intraparenchymal brain tumors. In M.A. Hayat, editor, *Tumors of the Central Nervous system*, volume 3, pages 261–267. Springer Netherlands, 2011.

[3] Robert J. Webster III, Allison M. Okamura, , and Noah J. Cowan. Toward active cannulas: Miniature snake-like surgical robots. In *Proceedings of the IEEE/RSJ International Conference on Intelligent Robots and Systems*, pages 2857–2863, 2006.

[4] Amir Degani, Howie Choset, Alon Wolf, Takeyoshi Ota, and Marco A. Zenati. Percutaneous intrapericardial interventions using a highly articulated robotic probe. In *Proceedings of the IEEE International Conference on Biomedical Robotics and Biomechatronics*, pages 7–12, 2006.

[5] Kai Xu and Nabil Simaan. Analytic formulation for kinematics, statics, and shape restoration of multibackbone continuum robots via elliptic integrals. *ASME Journal of Mechanisms and Robotics*, 2:011006–1 – 011006–13, 2010.

[6] Gorkem Dogangil, Brian L. Davies, and Ferdinando Rodriguez y Baena. A review of medical robotics for minimally invasive soft tissue surgery. *Proceedings of the Institution of Mechanical Engineers, Part H: Journal of Engineering in Medicine*, 224(5):653–679, 2010.

[7] Yik San Kwoh, Joahin Hou, Edmond A. Jonckheere, and Samad Hayati. A robot with improved absolute positioning accuracy for CT guided stereotactic brain surgery. *IEEE Transactions on Biomedical Engineering*, 35(2):153–160, 1988.

[8] James M. Drake, Michael Joy, Andrew Goldenberg, and David Kreindler. Computer and robotic assisted resection of brain tumours. In *Proceedings of the International Conference on Advanced Robotics*, volume 1, pages 888–892, 1991.

[9] C.W. Burckhardt, P. Flury, and D. Glauser. Stereotactic brain surgery. *IEEE Engineering in Medicine and Biology Magazine*, 14(3):314–317, 1995.

[10] AL Benabid, P Cinquin, S Lavalle, JF Le Bas, J Demongeot, and J de Rougemont. Computer-driven robot for stereotactic surgery connected to CT scan and magnetic resonance imaging. *Appl Neurophysiol*, 50:153–154, 1987.

[11] Paul B. McBeth, Deon F. Louw, Peter R. Rizun, and Garnette R. Sutherland. Robotics in neurosurgery. *The American Journal of Surgery*, 18(4, Supplement 1):68–75, 2004.

[12] Kazuhiro Hongo, Tetsuya Goto, Yukinari Kakizawa, Jun ichi Koyama, Toshikazu Kawai, Kazutoshi Kan, Yuichiro Tanaka, and Shigeaki Kobayashi. Micromanipulator system (NeuRobot): clinical application in neurosurgery. In *Proceedings of the 17th International Congress and Exhibition on Computer Assisted Radiology and Surgery.*, volume 1256, pages 509–513, 2003.

[13] Arne Radetzky and Michael Rudolph. Simulating tumour removal in neurosurgery. *International Journal of Medical Informatics*, 64(2-3):461–472, 2001.

[14] H. Takasuna, T. Goto, Y. Kakizawa, T. Miyahara, J. Koyama, Y. Tanaka, T. Kawai, and K. Hongo. Use of a micromanipulator system (neurobot) in endoscopic neurosurgery. *Journal of Clinical Neuroscience*, 19:1553–1557, 2012.

[15] Junchuan Liu, Yuru Zhang, Tianmiao Wang, Hongguang Xing, and Zengmin Tian. Neuromaster: A robot system for neurosurgery. In *Proceedings of the IEEE International Conference on Robotics and Automation*, pages 824–828, 2004.

[16] PathFinder. Prosurgics ltd., 2012 (online). Available from http://prosurgics.com/prosurgics_pathfinder.htm.

[17] G Deacon, A Harwood, J Holdback, D Maiwand, M Pearce, I Reid, M Street, and J Taylor. The pathfinder image-guided surgical robot. *Proceedings of the Institution of Mechanical Engineers, Part H: Journal of Engineering in Medicine*, 224(5):691–713, 2010.

[18] M. S. Eljamel. Validation of the Pathfinder neurosurgical robot using a phantom. *The International Journal of Medical Robotics and Computer Assisted Surgery*, 3(4):372–377, 2007.

[19] N. B. Morgan and M. Broadley. Taking the art out of smart! - Forming processes and durability issues for the application of NiTi shape memory alloys in medical devices. In *Materials & Processes for Medical Devices Conference*, pages 247–252, 2003.

[20] R. Shamir, M. Freiman, L. Joskowicz, M. Shoham, E. Zehavi, and Y. Shoshan. Robot-assisted image-guided targeting for minimally invasive neurosurgery: planning, registration, and in-vitro experiment. In *Proceedings of the International Conference on Medical Image Computing and Computer-Assisted Intervention*, pages 131–138, 2005.

[21] Moshe Shoham, Michael Burman, Eli Zehavi, Leo Joskowicz, Eduard Batkilin, and Yigal Kunicher. Bone-mounted miniature robot for surgical procedures: Concept and clinical applications. *IEEE Transactions on Robotics and Automation*, 19(5):893–901, 2003.

[22] M. Sam Eljamel. *Medical Robotics*, chapter 5 Robotic Applications in Neurosurgery. InTech, 2008.

[23] D. Stoianovici. Multi-imager compatible actuation principles in surgical robotics. *The international journal of medical robotics computer assisted surgery*, 1:86–100, 2005.

[24] C. Nimsky, O. Ganslandt, M. Buchfelder, and R. Fahlbusch. Intraoperative visualization for resection of gliomas: the role of functional neuronavigation and intraoperative 1.5 T MRI. *Journal of Neurology Research*, 28(5):482–487, 2006.

[25] Elizabeth B. Claus, Andres Horlacher, Liangge Hsu, Richard B. Schwartz, Donna Dello-Iacono, Florian Talos, Ferenc A. Jolesz, and Peter M. Black. Survival rates in patients with low-grade glioma after intraoperative magnetic resonance image guidance. *Cancer*, 103(6):1227–1233, 2005.

[26] A. Krieger, R.C. Susil, C. Menard, J.A. Coleman, G. Fichtinger, E. Atalar, and L.L. Whitcomb. Design of a novel mri compatible manipulator for image guided prostate interventions. *IEEE Transactions on Biomedical Engineering*, 52(2):306–313, 2005.

[27] A. Krieger, I. Iordachita, Sang-Eun Song, N.B. Cho, P. Guion, G. Fichtinger, and L.L. Whitcomb. Development and preliminary evaluation of an actuated mri-compatible robotic device for mri-guided prostate intervention. In *Proceedings of the IEEE International Conference on Robotics and Automation*, pages 1066 –1073, 2010.

[28] Yi Wang, Gregory A. Cole, Hao Su, Julie G. Pilitsis, and Gregory S. Fischer. MRI compatibility evaluation of a piezoelectric actuator system for a neural interventional robot. In *Proceedings of the IEEE Engineering in Medicine and Biology Society Annual International Conference*, pages 6072–6075, 2009.

[29] Rebecca Kokes, Kevin Lister, Rao Gullapalli, Bao Zhang, Alan MacMillan, Howard Richard, and Jaydev P. Desai. Towards a teleoperated needle driver robot with haptic feedback for RFA of breast tumors under continuous mri. *Medical Image Analysis*, 13(3):445–455, 2009.

[30] Bo Yang, U-Xuan Tan, Alan B. McMillan, Rao Gullapalli, and Jaydev P. Desai. Design and control of a 1-DOF MRI-compatible pneumatically actuated robot with long transmission lines. *IEEE/ASME Transactions on Mechatronics*, 16:1040–1048, 2011.

[31] Nikolaos V. Tsekos, Azadeh Khanicheh, Eftychios Christoforou, and Constantinos Mavroidis. Magnetic resonance compatible robotic and mechatronics systems for image-guided interventions and rehabilitation: A review study. *Annual Review of Biomedical Engineering*, 9:351–387, 2007.

[32] R. Gassert, E. Burdet, and K. Chinzei. Opportunities and challenges in MR-compatible robotics. *IEEE Engineering in Medicine and Biology Magazine*, 27(3):15–22, 2008.

[33] John F. Schenck. The role of magnetic susceptibility in magnetic resonance imaging: MRI magnetic compatibility of the first and second kinds. *Medical Physics*, 23(6):815–580, 1996.

[34] Kiyoyuki Chinzei, Ron Kikinis, and Ferenc A. Jolesz. MR compatibility of mechatronic devices: Design criteria. In *Proceedings of the International Conference on Medical Image Computing and Computer-Assisted Intervention*, pages 1020–1030, 1999.

[35] H. Elhawary, A. Zivanovic, B. Davies, and M. Lamperth. A review of magnetic resonance imaging compatible manipulators in surgery. In *Proceedings of the Institution of Mechanical Engineers Part H Journal of engineering in medicine*, volume 220, pages 413–424.

[36] Roger Gassert, Akio Yamamoto, Dominique Chapuis, Ludovic Dovat, Hannes Bleuler, and Etienne Burdet. Actuation methods for applications in mr environments. *Concepts in Magnetic Resonance Part B: Magnetic Resonance Engineering*, 29B:191–209, 2006.

[37] K. Masamune, E. Kobayashi, Y. Masutani, M. Suzuki, T. Dohi, H. Iseki, and K. Takakura. Development of an MRI-compatible needle insertion manipulator for stereotactic neurosurgery. *Journal of Image Guided Surgery*, 1(4):242–248, 1995.

[38] Garnette R. Sutherland, Paul B. McBeth, and Deon F. Louw. Neuroarm: an mr compatible robot for microsurgery. In *Proceedings of the 17th International Congress and Exhibition on Computer Assisted Radiology and Surgery.*, volume 1256, pages 504–508, 2003.

[39] NEUROARM. University of calgary, 2012 (online). Available from http://www.neuroarm.org/.

[40] Gregory Cole, Julie Pilitsis, and Gregory S. Fischer. Design of a robotic system for MRI-guided deep brain stimulation electrode placement. In *Proceedings of the IEEE International Conference on Robotics and Automation*, pages 4450–4456, 2009.

[41] Nobuhiko Hata, Steve Piper, Ferenc A Jolesz, Clare MC Tempany, Peter McL Black, Shigehiro Morikawa, Horoshi Iseki, Makoto Hashizume, , and Ron Kikinis. Application of open source image guided therapy software in MR-guided therapies. In *Proceedings of the International Conference on Medical Image Computing and Computer-Assisted Intervention*, volume 4791, pages 491–498, 2007.

[42] Cyrus Raoufi, Andrew A. Goldenberg, and Walter Kucharczyk. Design and control of a novel hydraulically/pneumatically actuated robotic system for MRI-guided neurosurgery. *Journal of Biomedical Science and Engineering*, 1:68–74, 2008.

[43] M.C. Cavusoglu, F. Tendick, M. Cohn, and S.S. Sastry. A laparoscopic telesurgical workstation. *IEEE Transactions on Robotics and Automation*, 15(4):728–739, 1999.

[44] Nabil Simaan, Russell Taylor, and Paul Flint. High dexterity snake-like robotic slaves for minimally invasive telesurgery of the upper airway. In *Proceedings of the International Conference on Medical Image Computing and Computer-Assisted Intervention*, pages 17–24, 2004.

[45] Takeyoshi Ota, Amir Degani, David Schwartzman, Brett Zubiate, Jeremy McGarvey, Howie Choset, and Marco A. Zenati. A highly articulated robotic surgical system for minimally invasive surgery. *The Annals of Thoracic Surgery*, 87:1253–1256, 2009.

[46] D. Chapuis, R. Gassert, G. Ganesh, E. Burdet, and H. Bleuler. Investigation of a cable transmission for the actuation of mr compatible haptic interfaces. pages 426–431, 2006.

[47] G.M. Bone and Shu Ning. Experimental comparison of position tracking control algorithms for pneumatic cylinder actuators. *IEEE/ASME Transactions on Mechatronics*, 12(5):557–561, 2007.

[48] G.S. Fischer, I. Iordachita, C. Csoma, J. Tokuda, S.P. DiMaio, C.M. Tempany, N. Hata, and G. Fichtinger. MRI-compatible pneumatic robot for transperineal prostate needle placement. *IEEE/ASME Transactions on Mechatronics*, 13(3):295–305, 2008.

[49] Dan Stoianovici, Alexandru Patriciu, Doru Petrisor, Dumitru Mazilu, and Louis Kavoussi. A new type of motor: Pneumatic step motor. *IEEE/ASME Transactions on Mechatronics*, 12(1):98–106, 2007.

[50] A. Patriciu, D. Petrisor, M. Muntener, D. Mazilu, M. Schar, and D. Stoianovici. Automatic brachytherapy seed placement under mri guidance. *IEEE Transactions on Biomedical Engineering*, 54(8):1499–1506, 2007.

[51] H. Sajima, I. Sato, H. Yamashita, T. Dohi, and K. Masamune. Two-DOF nonmetal manipulator with pneumatic stepping actuators for needle puncturing inside open-type MRI. In *World Automation Congress (WAC)*, pages 1–6, 2010.

[52] Daeyoung Kim, Etsuko Kobayashi, Takeyoshi Dohi, and Ichiro Sakuma. A new, compact MR-compatible surgical manipulator for minimally invasive liver surgery. In *Proceedings of the International Conference on Medical Image Computing and Computer-Assisted Intervention*, pages 99–106, 2002.

[53] K. Ikuta, M. Matsuda, D. Yajima, and Y. Ota. Pressure pulse drive: A control method for the precise bending of hydraulic active catheters. *IEEE/ASME Transactions on Mechatronics*, PP(99):1–8, 2011.

[54] Ningbo Yu, C. Hollnagel, A. Blickenstorfer, S.S. Kollias, and R. Riener. Comparison of MRI-compatible mechatronic systems with hydrodynamic and pneumatic actuation. *IEEE/ASME Transactions on Mechatronics*, 13(3):268–277, 2008.

[55] Bo Yang, U-Xuan Tan, Alan McMillan, Rao Gullapalli, and Jaydev P. Desai. Design and implementation of a pneumatically-actuated robot for breast biopsy under continuous MRI. In *Proceedings of the IEEE International Conference on Robotics and Automation*, pages 674–679, 2011.

[56] M. Oura, Y. Kobayashi, J. Okamoto, and M.G. Fujie. Development of mri compatible versatile manipulator for minimally invasive surgery. In *Proceedings of the IEEE International Conference on Biomedical Robotics and Biomechatronics*, pages 176–181, 2006.

[57] J. Izawa, T. Shimizu, T. Aodai, T. Kondo, H. Gomi, S. Toyama, and K. Ito. Mr compatible manipulandum with ultrasonic motor for fmri studies. In *Proceedings of the IEEE International Conference on Robotics and Automation*, pages 3850–3854, 2006.

[58] K. Harada, K. Tsubouchi, M.G. Fujie, and T. Chiba. Micro manipulators for intrauterine fetal surgery in an open mri. In *Proceedings of the IEEE International Conference on Robotics and Automation*, pages 502–507, 2005.

[59] Federico Carpi, Azadeh Khanicheh, Constantinos Mavroidis, and Danilo De Rossi. MRI compatibility of silicone-made contractile dielectric elastomer actuators. *IEEE/ASME Transactions on Mechatronics*, 13(3):370–374, 2008.

[60] Koji Ikuta, Masahiro Tsukumoto, and Shigeo Hirose. Shape memory alloy servo actuator system with electric resistance feedback and application for active endoscope. In *Proceedings of the IEEE International Conference on Robotics and Automation*, pages 427–430, 1988.

[61] Y. Nakamura, A. Matsui, T. Saito, and K. Yoshimoto. Shape-memory-alloy active forceps for laparoscopic surgery. In *Proceedings of the IEEE International Conference on Robotics and Automation*, pages 2320–2327, 1995.

[62] Elif Ayvali, Chia-Pin Liang, Mingyen Ho, Yu Chen, and Jaydev P Desai. Towards a discretely actuated steerable cannula for diagnostic and therapeutic procedures. *International Journal of Robotics Research*, 31(5):588–603, 2012.

[63] Andrea Holton, Edward Walsh, Andreas Anayiotos, Gerald Pohost, and Ramakrishna Venugopalan. Comparative MRI compatibility of 316L stainless steel alloy and nickel-titanium alloy stents. *Journal of Cardiovascular Magnetic Resonance*, 4(4):423–430, 2002.

[64] K. Ikuta. Micro/miniature shape memory alloy actuator. In *Proceedings of the IEEE International Conference on Robotics and Automation*, pages 2156–2161, 1990.

[65] Mohammed Es-Souni, Martha Es-Souni, and Helge Fischer-Brandies. Assessing the biocompatibility of NiTi shape memory alloys used for medical applications. *Analytical and Bioanalytical Chemistry*, 381(3):557–567, 2005.

[66] Daniel J. Hoh, Brian L. Hoh, Arun P. Amar, and Michael Y. Wang. Shape memory alloys: metallurgy, biocompatibility, and biomechanics for neurosurgical applications. *Neurosurgery*, 64(5):199–214, 2009.

[67] Mingyen Ho and Jaydev P. Desai. Characterization of SMA actuator for applications in robotic neurosurgery. In *Proceedings of the IEEE Engineering in Medicine and Biology Society Annual International Conference*, pages 6856–6859, 2009.

[68] Mingyen Ho and Jaydev P. Desai. Towards a MRI-compatible meso-scale SMA-actuated robot using PWM control. In *Proceedings of the IEEE International Conference on Biomedical Robotics and Biomechatronics*, pages 361–366, 2010.

[69] W. J. Buehler, J. V. Gilfrich, and R. C. Wiley. Effect of low-temperature phase changes on the mechanical properties of alloys near composition NiTi. *Journal of Applied Physics*, 34(5):1475–1477, 1963.

[70] E. Pieczyska, S. Gadaj, W.K. Nowacki, K. Hoshio, Y. Makino, and H. Tobushi. Characteristics of energy storage and dissipation in tini shape memory alloy. *Science and Technology of Advanced Materials*, 6(8):889–894, 2005.

[71] C. Liang and C. A. Rogers. Design of shape memory alloy springs with applications in vibration control. *Journal of Intelligent Material Systems and Structures*, 8(4):314–322, 1997.

[72] Kikuaki Tanaka. A thermomechanical sketch of shape memory effect: One-dimensional tensile behavior. *Res Mechanica*, 18(3):251–263, 1986.

[73] C. Liang and C. A. Rogers. One-dimensional thermomechanical constitutive relations for shape memory materials. *Journal of Intelligent Material Systems and Structures*, 1(2):207–230, 1990.

[74] L. Catherine Brinson. One-dimensional constitutive behavior of shape memory alloys: Thermomechanical derivation with non-constant material functions and redefined martensite internal variable. *Journal of Intelligent Material Systems and Structures*, 4(2):229–242, 1993.

[75] Yee Harn Teh and Roy Featherstone. An architecture for fast and accurate control of shape memory alloy actuators. *International Journal of Robotics Research*, 27(5):595–611, 2008.

[76] Gangbing Song, Brian Kelly, and Brij N Agrawal. Active position control of a shape memory alloy wire actuated composite beam. *Smart Materials and Structures*, 9(5):711–716, 2000.

[77] Troisfontaine Ph Bidaud, N. Troisfontaine, Ph. Bidaud, and P. Dario. Control experiments on two sma based micro-actuators. In *International Symposium on Experimental Robotics*, pages 490–499, 1997.

[78] N. Ma, G. Song, and H-J Lee. Position control of shape memory alloy actuators with internal electrical resistance feedback using neural networks. *Smart Materials and Structures*, 13(4):777–783, 2004.

[79] Vishalini Bundhoo, Edmund Haslam, Benjamin Birch, and Edward J. Park. A shape memory alloy-based tendon-driven actuation system for biomimetic artificial fingers, part I: Design and evaluation. *Robotica*, 27:131–146, 2009.

[80] N. Ma and G. Song. Control of shape memory alloy actuator using pulse width modulation. *Smart Materials and Structures*, 12(5):712–719, 2003.

[81] Yuuta Sugiyama and Shinichi Hirai. Crawling and jumping by a deformable robot. *International Journal of Robotics Research*, 25(5-6):603–620, 2006.

[82] A. D. Price, A. Jnifene, and H. E. Naguib. Design and control of a shape memory alloy based dexterous robot hand. *Smart Materials and Structures*, 16(4):1401–1414, 2007.

[83] Gabriele Gilardi, Edmund Haslam, Vishalini Bundhoo, and Edward J. Park. A shape memory alloy-based tendon-driven actuation system for biomimetic artificial fingers, part II: Modeling and control. *Robotica*, 28:675–687, 2010.

[84] K. Craig Goodrich, J. Rock Hadley, Sung M. Moon, Blaine A. Chronik, Timothy J. Scholl, Joshua T. Debever, and Dennis L. Parker. Design, fabrication and testing of an insertable double-imaging-region gradient coil. *Concepts in Magnetic Resonance Part B: Magnetic Resonance Engineering*, 35B:98–105, 2009.

[85] J. A. Shaw, C. B. Churchill, and M. A. Iadicola. Tips and tricks for characterizing shape memory alloy wire: Part 1 - Differential scanning calorimetry and basic phenomena. *Experimental Techniques*, 32:55–62, 2008.

[86] C. B. Churchill, J. A. Shaw, and M. A. Iadicola. Tips and tricks for characterizing shape memory alloy wire: Part 2 - Fundamental isothermal responses. *Experimental Techniques*, 33:51–62, 2009.

[87] D. C. Lagoudas, P. B. Entchev, and P. K. Kumar. Thermomechanical characterization of sma actuators under cyclic loading. In *Proceedings of the ASME International Mechanical Engineering Congress and Exposition*, pages 211–217, 2003.

[88] V. R. C. Kode and M. C. Cavusoglu. Design and characterization of a novel hybrid actuator using shape memory alloy and DC micromotor for minimally invasive surgery applications. *IEEE/ASME Transactions on Mechatronics*, 12:455–464, 2007.

[89] Mingyen Ho, Michael Koltz, J. Marc Simard, Rao Gullapalli, and Jaydev P. Desai. Towards a MR image-guided SMA-actuated neurosurgical robot. In *Proceedings of the IEEE International Conference on Robotics and Automation*, pages 1153–1158, 2011.

[90] Mingyen Ho, Alan B. McMillan, J. Marc Simard, Rao Gullapalli, and Jaydev P. Desai. Toward a meso-scale SMA-actuated MRI-compatible neurosurgical robot. *IEEE Transactions on Robotics*, 28(1):213–222, 2012.

[91] Nicholas Pappafotis, Wojciech Bejgerowski, Rao Gullapalli, J. Marc Simard, Satyandra K. Gupta, and Jaydev P. Desai. Towards design and fabrication of a miniature MRI-compatible robot for applications in neurosurgery. In *Proceedings of the ASME International Design Engineering Technical Conferences and Computers and Information in Engineering Conference*, pages 747–754, 2008.

[92] Bruce D. Lucas and Takeo Kanade. An iterative image registration technique with an application to stereo vision. In *Proceedings of the international joint conference on Artificial intelligence*, pages 674–679, 1981.

[93] NEMA Standards Publication MS 1-2008. *Determination of Signal-to-Noise Ratio (SNR) in Diagnostic Magnetic Resonance Imaging*. National Electrical Manufacturers Association, 2008.

[94] Mingyen Ho and Jaydev P. Desai. Design of a MRI-compatible tendon-driven neurosurgical robot. In *Proceedings of the ASME Dynamic Systems and Control Conference*, 2011.

[95] Mingyen Ho and Jaydev P. Desai. Towards the development of a sma-actuated mri-compatible tendon-driven neurosurgical robot. In *Proceedings of the IEEE International Conference on Robotics and Automation*, pages 683–688, 2012.

[96] Mingyen Ho and Jaydev P. Desai. Characterization of antagonistic SMA spring actuators for use in a MRI-compatible intracranial robot. In *Proceedings of the ASME Dynamic Systems and Control Conference*, 2012.

[97] Hisaaki Tobushi and Kikuaki Tanaka. Deformation of a shape memory alloy helical spring : Analysis based on stress-strain-temperature relation. *JSME international journal. Ser. 1, Solid mechanics, strength of materials*, 34-I(1):83–89, 1991.

[98] Sung-Min An, Junghyun Ryu, Maenghyo Cho, and Kyu-Jin Cho. Engineering design framework for a shape memory alloy coil spring actuator using a static two-state model. *Smart Materials and Structures*, 21(5):055009, 2012.

[99] Joseph Edward Shigley and Charles R. Mischke. *Mechanical Engineering Design*. McGraw Hill, 2001.

[100] Varun Agrawal, William J. Peine, and Bin Yao. Modeling of transmission characteristics across a cable-conduit system. *IEEE Transactions on Robotics*, 26(5):914–924, 2010.

[101] Gianluca Palli, Gianni Borghesan, and Claudio Melchiorri. Modeling, identification, and control of tendon-based actuation systems. *IEEE Transactions on Robotics*, 28(2):277–290, 2012.

[102] Michael D. Schmidt and Hod Lipson. Coevolution of fitness predictors. *IEEE Transactions on Evolutionary Computation*, 12(6):736–749, 2008.